AN ABSTRACT OF THE THESIS OF

Subin Sahu for the degree of Doctor of Philosophy in Physics presented on May 23, 2017.
Title: Nonlinear Behavior of Thermal and Ion Transport at the Nanoscale

Abstract approved: _____

Michael Zwolak

Functional control at the nanoscale forms the foundation of biological systems. These work at the cellular level by manipulating ions and molecules. Nanoscale devices that give functional control at this scale are also becoming an important component in diverse fields such as electronics, medicine, engineering, and manufacturing. Moreover, scientific advances are making it technologically viable to control and observe matter at the atomic level. Computational techniques are an integral part in designing and understanding these systems, as they reveal the processes that are experimentally unobservable and allow for inexpensive screening and predictions. Since the atomistic nature of matter plays a major role at the nanoscale, classical all-atom molecular dynamic simulations are widely employed.

We concentrate on thermal transport, ion transport, and nonlinear interactions at the nanoscale. For thermal transport, in particular, we develop a rigorous approach to computing thermal conductance by coupling a system of interest to two large "extended reservoirs" that act as heat source/sinks. Within this setup, we prove that the "intrinsic conductance" of the system can be obtained by having the extended reservoirs be large and weakly coupled to Langevin baths.

For ion transport, we show that subnanoscale pores in monolayer graphene membranes display selectivity (not unlike biological ion channels but weaker) even when the graphene pores do not have charge or functional groups. The selectivity appears because the ions translocating through these pores lose some water from their solvation shell and different ions have different energy dehydration penalties. We also demonstrate that such

selectivity can be tuned by adjusting the pore radius and number of graphene layers. This will enable the optimization of water flow and ion rejection for applications such as filtration and desalination. We also develop a finite-size scaling model to compute the effect of bulk electrolyte dimension on the ionic resistance. This separates the pore and the bulk electrolyte contribution to the total ionic resistance in molecular dynamics simulations. Additionally, in collaboration with an experimental group, we show that graphene is a good choice for a transparent cap for spectroscopy of water as it only has a minor influence on the structure of water.

Nonlinear Behavior of Thermal and Ion Transport at the Nanoscale

by

Subin Sahu

A THESIS

submitted to

Oregon State University

in partial fulfillment of
the requirements for the
degree of

Doctor of Philosophy

Presented May 23, 2017
Commencement June 2017

Doctor of Philosophy thesis of Subin Sahu presented on May 23, 2017

APPROVED:

Major Professor, representing Physics

Chair of the Department of Physics

Dean of the Graduate School

I understand that my thesis will become part of the permanent collection of Oregon State University libraries. My signature below authorizes release of my thesis to any reader upon request.

Subin Sahu, Author

ACKNOWLEDGEMENTS

My deepest thanks to my advisor Michael Zwolak for his guidance and support which were paramount for the completion of this thesis and will also guide me in my future endeavors. My sincere thanks also go to Massimiliano Di Ventra, Kirill Velizhanin, Chih-Chun Chien, Yonatan Dubi, Evgheni Strelcov, Hongxuan Guo, Alexander Yulaev, Jian Wang, Narayana Appathurai, Stephen Urquhart, John Vinson and Andrei Kolmakov for collaboration on great projects. Special thanks to my group members Daniel Gruss, Joshua Kincaid, Xiaoxuan Hung, Justin Elenewski for the helpful discussions and comments. I'm grateful to all the faculty in Department of Physics at Oregon State University and my committee members David Roundy, Guenter Schneider, Weihong Qiu and P. Alex Greaney for their instructions. I also want to thank the Institute for Research in Electronic and Applied Physics(IREAP) at the University of Maryland for granting the research opportunity at Center for Nanoscale Science and Technology (CNST), National Institute of Standards and Technology (NIST).

I want to express my gratitude toward my fellow grad students at OSU, especially Hiral Patel, Kati Bilty, Bo Chen, Andrew Stickel, Krishna Poudel, Dinesh Timilsina, Gehendra Bhattarai, Birat Sapkota, Deepak Rayamajhi, DS Niroula and Suman Pant for being great friends. I'm also thankful for all the encouragements from my parents, my brother, and my sister, which helped me throughout this journey. Most of all, I want to thank Erica, who was always there for me.

TABLE OF CONTENTS

TABLE OF CONTENTS (Continued)

TABLE OF CONTENTS (Continued)

TABLE OF CONTENTS (Continued)

LIST OF FIGURES

LIST OF FIGURES (Continued)

LIST OF TABLES

NONLINEAR BEHAVIOR OF THERMAL AND ION TRANSPORT AT THE NANOSCALE

1. INTRODUCTION

With the remarkable advancement in the ability to visualize, control, and simulate matter up to the atomic scale, past decade has seen significant progress in nanotechnology and has opened new avenues in diverse fields such as biotechnology, molecular biology, medicine, surface science, engineering, material science just to mention few. Although the basic physics – from classical to quantum – needed for understanding the dynamics of nanoscale systems were developed several decades ago, their application at such length scale, however, produces novel and surprising effects not seen at macro-scale. Thus, on the one hand, nanoscale science has galvanized the advancement of technology, and on the other hand, it has advanced our basic understanding of nature.

Nanoscale science and modern computers have mutually benefited from each other; with nanotechnology contributing to the continuous development of computational capabilities and in return computational technique becoming an integral part of the study of nanoscale systems. The advancement in the modern computer has made it possible to simulate complex systems at atomic level details, which helps to understand the physics that are elusive in experiments. The importance of computational technique for the future of science is highlighted by 2013 Nobel Prize in Chemistry being awarded to computational chemist Martin Karplus, Michael Levitt and Arieh Warshel for their development of multiscale methods for complex systems.

1.1. Transport at nanoscale

Transport properties at the nanoscale are interesting because the functions of nanoscale systems – whether they are biological such as DNA or artificial such as nanosensors – depend not only on the structure but also on the dynamics of the system. Transport properties at this length scale are fundamentally different than at macro level because the continuum approximations fail and it becomes necessary to consider the atomic details of the system [4]. All type of transport phenomena involving the exchange of mass, energy, charge, momentum, or angular momentum is of interest in the nanoscale science among which I will be focusing on the thermal and the ion transport.

1.1.1 Thermal transport and Fourier's law

Management of heat energy is essential for any power consuming or heat dissipating device, but this is especially the case for the nano- and micro- scale devices. On the one hand, thermal energy can be used to power these devices, for example, the nanoscale thermoelectric generator can drive current in the nanoscale electronic device. On the other hand, proper management of heat is critical for the basic operation of nano- and microscale devices. Besides the technological applications, it is also interesting to understand how Fouriers law behave in microscale. Fourier's law of thermal transport,

$$\vec{J}_H = -\kappa \nabla T, \tag{1.1}$$

is an empirical law that relates heat current $\vec{J}_H$ to the temperature gradient ∇T, where the proportionality constant κ is called thermal conductivity. However, proving the Fourier's law from the first principle remains a challenge in Theoretical Physics [5]. Thermal transport through a system can also reveal the structural properties of the system and thus can be used to analyze the properties of the nanoscale systems.

1.1.2 Ion transport through nanoscale pores

Ion transport through nanoscale pores is a common process in various biological phenomena. Ion channels, in particular, play a crucial role in physiological functions such as the generation of electrical activity in the nerves and muscle, volume regulation of cells, intracellular signaling and so on. In fact, ion channels are often an important target for new drug discovery since malfunctioning ion channels can cause several diseases [6]. However, these ion channels are very complex and various factors such as charge and dipole moments, structural changes of the protein and dehydration control their function. Solid state nanopores on the contrary are much simpler and can mimic aspects of biological pores. Ion transport through these pores have several interesting applications. Ion transport through nanopores is getting further attention due to the discovery of atomically thick membranes such as graphene, MoS_2 and hexagonal BN.

1.2. Graphene nanopores

Graphene is a two-dimensional material with atomic-scale thickness consisting of the hexagonal lattice with carbon atoms at each vertex. Theoretical description of graphene dated back to 1940's [7] and was observed under the electron microscope as early as 1960's [8]. It was isolated in a stable two-dimensional form in 2004 [9], for which Andre Geim and Konstantin Novoselov were awarded the Nobel Prize in Physics in 2010. Graphene has drawn the widespread attention of researchers due to its unique electronic and physical properties.

Recent studies have shown that pores can be drilled through graphene with atomic level precision [2, 10, 11]. Along with its flexible, exceptional mechanical strength, and biocompatibility, graphene is an ideal material for application such as bio-sensing, chemical-sensing, and filtration. The detailed understanding of ion transport process in graphene nanopore is crucial for its intended applications.

1.3. Surface interactions at nanoscale

Nanoscale systems have a much larger surface to volume ratio than macro-scale systems which enhance the contact between different materials and hence increases the reactivity. Thus the nanomaterials can be useful catalysts for chemical reactions as well as an excellent candidate for applications such as filtration and purification. At the same time, surface interactions play a much more important role in these systems and also give rise to unusual behavior not seen at the macro scale.

1.4. Applications

This section provides brief descriptions of some of the key applications of thermal transport and ion transport at the nanoscale.

1.4.1 Thermal management at nanoscale

Heat transport plays important roles in nanotechnology as often it hinders the miniaturization of electronics device [12]. Nanoscale devices such as heat diode [13] and heat transistors [14, 15] are being studied for controlling thermal current at the nanoscale and on-chip micro-refrigerator [16] are also possible solution maintaining the temperature of nano device. However, heat is not just a hindrance to the development of nanotechnology, and thermal transport has some interesting applications in this field. For example, temperature control can be used to fine-tune electronic current in nanoscale device [17], particularly at the superconducting regime. Material such as DNA, which have rapidly rising thermal conductance in a narrow temperature range may be used to engineer nanoscale thermal switch [12]. In the growing field of nanomedicine researchers are studying the use of heat energy for the targeted treatment of tumor and cancer cell [18]. All of these applications requires the detailed understanding of thermal transport at the nanoscale.

1.4.2 Ion Channel targeted drug discovery

Biological ion channels are essential components of cell operation. They pump ions and other species across biological membranes by opening and closing in response to stimuli. Malfunctioning of these pores causes numerous diseases; thus ion-channel targeted drug discovery is very compelling. However, the immense complexity of these pores makes it tough to delineate the role of different factors in their function. For example, the dehydration process is important for understanding the behavior of ions and the selectivity of biological channels, but it is hard to study its effect in such complex systems. Study of ion transport through solid state nanopore is much simpler and can reveal important details about the ion transport process, which can be utilized to understand the overall working mechanism of the ion channel. The dynamic mechanism of ion transport through confined geometry is necessary to understand the mechanism that leads to malfunctioning of these pores.

1.4.3 DNA and Protein sequencing

One of the interesting applications of ion transport through nanopores is for sequencing of DNA and protein. Biological pores such as alpha-hemolysin have been successfully used to identify all four DNA bases [19]. However, the natural pores are very sensitive to environmental conditions and are difficult to control outside the lab condition [20]. Studies are being carried out to use solid state nanopore including graphene nanopore for sequencing DNA by analyzing the blockade current as it is pulled through the pore using some external force. Such sequencing technique will be revolutionary in the medical field as such technique will not only be inexpensive but also ultra-fast as well. However, several challenges have to be overcome before such technology can be implemented at the commercial level. Understanding ion transport through nano- and subnano- scale pore is crucial for developing the capability to analyze the blockade ionic current and discriminate the individual base pair of DNA.

1.4.4 Bio and Chemical Sensing

Besides DNA and protein sequencing, nanopores can also be used for other biosensing application. These pores can be made selective, either be functionalizing them, or by proper control of their size. Such pore will be able to discriminate different species based on their size, charge, or functional group, thus making them suitable for sensing application [21]. Ion transport through nanoscale channels is also utilized to scan biological membrane and other surfaces using the technique known as Scanning Ion Conductance Microscopy [22]. The method has been demonstrated to able to examine biological membrane in vivo without artificial label [23].

1.4.5 Molecular sieving and desalination

Another application of ion transport through graphene and graphene-based nanopores is in molecular sieving and desalination. Since graphene is only one atom thick, porous graphene membrane allows very fast flow of water through them. The pore sizes in graphene can be controlled up to atomic level thus these pores can be engineered for letting one set of molecules/particles to flow and blocking others based on their ionic or solvated size. Porous graphene has also been shown to be able to separate gasses.

1.5. Outline

The remaining chapters in this thesis are organized as follows:

- Chapter 2 provides the details of the methods used in the remainder of this thesis.
- Chapter 3 contains work done in collaboration with Kirill A Velizhanin, Chih-Chun Chien, Yonatan Dubi, where we studied the crossover behavior of thermal conductance in harmonic and anharmonic lattices similar to Kramars' transition rate theory in chemical reactions.
- Chapter 4 contains work done in collaboration with Massimiliano Di Ventra. We explored the dehydration based selectivity in graphene nanopores.

- Chapter 5 explores the ion selectivity in multilayer graphene nanopores.
- Chapter 6 contains the study of access resistance in graphene nanopores.
- Chapter 7 includes the work done in collaboration with Evgheni Strelcov, Hongxuan Guo, Alexander Yulaev, Jian Wang, Narayana Appathurai, Stephen Urquhart, John Vinson and Andrei Kolmakov from experimental groups at National Institute of Standards and Technology (NIST), Canadian Light Source Inc. and University of Saskatchewan. The work demonstrated that bilayer graphene does not significantly distort the electronic structure of water in the first few water layers and thus graphene-capped channel ultra-high vacuum spectromicroscopy of water.
- Appendices cover some mathematical derivations used in the thesis.

2. THEORY AND METHODS

The general method used in this thesis is to solve the Newtonian equation of motion of the particles under the influence of external force as well as frictional force and noise. The equation on its own is simple, but the complexity comes due to the sheer number of particles involved and interaction between them. The number of interactions increases very fast with the number of particles as N^2; thus various approach is used to reduce the computational complexity. In this chapter, I will present in detail the computational techniques used in the thesis.

2.1. Langevin Dynamics

Langevin Dynamics [24] is an effective way of including stochastic forces – random noise and friction in the equation of motion and hence approximate the effect of degrees of freedom that has been neglected. The equation of motion of a particle under the influence of noise and friction is given as

$$F(\vec{x}_n) + \vec{f}_n(t) = m\ddot{x}_n, \tag{2.1}$$

where, $F(\vec{x}_n)$ is the sum of external forces and $f_n(t) = \eta_n(t) - \gamma_n \dot{x}_n(t)$ is the random force. The noise $\eta_n(t)$ and friction coefficient γ_n are related by the fluctuation-dissipation relation

$$\langle \eta_n(t)\eta_m(t')\rangle = 2\gamma_n k_B T_n \delta_{nm}\delta(t-t'). \tag{2.2}$$

One can approximate the effect of solvent and environment using the proper choice of γ.

2.2. All-atom Molecular Dynamics Simulation

Atomic scale details are often required for understanding the behavior of nanoscale systems whether they are biological systems such as ion channels, proteins, nucleic acids or they are artificial nanoscale devices. To this end, all-atom MD simulation [25] allows one to explore the system with atomic level details. These simulations are computationally expensive since even a nanoscale system can have millions of atoms. Typically in MD simulation one uses periodic boundary condition to minimize the finite size effects. Thus MD simulation is well suited for systems with periodic boundary condition such as crystal structures. However such boundary conditions are also well suited for fluidic systems. Another limiting factor in these calculations is the integration time-step required to capture the fastest atomic interactions. The vibrations of covalent bonds are the most rapid interactions encountered in MD simulations and the time step should be in few femtoseconds or less to accurately calculate these interactions. Thus typical MD simulations are in the order of nano- to micro- seconds. However, with increasing computational power even millisecond long simulations are becoming feasible. With the current rate of progress, it won't be distant future when it is possible to simulation an entire cell with atomistic detail.

Force Fields

Even the smallest nanoscale biological systems or artificial devices will have thousands of atoms and thus cannot be solved using the first principle. The approach used in classical Molecular Dynamics is to ignore the electronic degree of freedom and calculate the dynamics of the system considering each atom as a single particle. The effective potential, also known as the force field, in all-atom MD has two parts:bonded interaction and non-bonded interaction.

2.2.1 Bonded interaction

Bonded interactions are due to chemical bonding between atoms, which can be ionic or covalent. They include three terms: Bond Stretching, Angle Bending, and Torsional

interaction.

Bond Stretching

An accurate representation of the bond stretching interaction is the Morse potential

$$E_{\text{bond}} = D\left[1 - e^{-a(x-x_m)}\right]^2 \tag{2.3}$$

where, D is the depth of the potential well and x_m is the equilibrium bond length. Morse potential becomes flat at a large bond separation – representing the bond breaking. For small bond stretching, which is generally the case in MD simulations, Hooke's law is a good approximation

$$E_{\text{bond}} = k_B(x - x_m)^2. \tag{2.4}$$

Angle Bending

Similar to the bond stretching, angle bending is also represented as a simple Hooke's law,

$$E_{\text{angle}} = k_\theta(\theta - \theta_m)^2, \tag{2.5}$$

where, θ_m is the equilibrium bond angle.

Torsional term

The energy due to the bond torsion (also known as dihedral energy) is calculated as

$$E_{\text{dehydral}} = k_\chi[1 + \cos(n\chi - \delta)], \tag{2.6}$$

where χ is the torsion angle and δ is the phase factor.

2.2.2 Non-bonded interactions

Non-bonded interactions occur between every pair of atoms that aren't chemically bonded. Non-bonded interactions include electrostatics interaction and van der Waals interaction.

Electrostatic interaction

The computation of electrostatic interactions between charged particles is the most numerically intensive calculation because the electrostatic forces decay rather slowly with distance. The electrostatic potential energy due to N charged particles $q_1, q_2, ..., q_N$ with position vectors $\vec{r}_1, \vec{r}_2, ..., \vec{r}_N$ is given as

$$E = \sum_i \sum_{j>i} \frac{q_i q_j}{4\pi\epsilon_o |\vec{r}_{ij}|} = \frac{1}{2} \sum_i \sum_{j \neq i} \frac{q_i q_j}{4\pi\epsilon_o |\vec{r}_{ij}|}. \tag{2.7}$$

Such direct calculation using Coulomb law is not practical for large system such as the one that includes explicit solvent. In a system with N particles, where each particle interacts with other $N-1$ particles the numerical complexity of electrostatic interaction scale as N^2. One of the ways to deal with the problem is to use a cutoff distance beyond which the electrostatic energy is considered zero. However, for a periodic system, some numerical techniques can be used to do full electrostatic calculation without using cutoffs.

Particle Mesh Ewald (PME)

Particle Mesh Ewald (PME) method [26] allows the calculation of full electrostatics for system with periodic boundary condition (PBC). With PBC, the total energy is:

$$\begin{aligned} E &= \sum_i \sum_{j \neq i} \frac{q_i q_j}{8\pi\epsilon_o |\vec{r}_{ij}|} + \sum_{n_1,n_2,n_3}{}' \sum_i \sum_j \frac{q_i q_j}{8\pi\epsilon_o |\vec{r}_{ij} + n_1\vec{T}_1 + n_2\vec{T}_2 + n_3\vec{T}_3|} \\ &= \sum_{n_1,n_2,n_3} \sum_i \sum_j{}' \frac{q_i q_j}{8\pi\epsilon_o |\vec{r}_{ij} + n_1\vec{T}_1 + n_2\vec{T}_2 + n_3\vec{T}_3|} \end{aligned} \tag{2.8}$$

where, $\sum_{n_1,n_2,n_3}{}'$ is sum with not all $n_i s$ zero, $\sum_j{}'$ is sum with $j \neq i$ for $n_1 = n_2 = n_3 = 0$; $\vec{T}_1$,$\vec{T}_2$,$\vec{T}_3$ are translation vectors of the periodic system; and q_i are charge.

The basic idea in PME method is to break Eq. 2.8 into short and long range interactions. The short range interaction converges quickly in the real space, and the long-range interaction converges in the reciprocal space.

For this purpose the point charge is replaced with charge distribution function. $\rho_i(r)$

which satisfies the Poisson's equation.

$$\nabla^2 \phi_i(r) = -\frac{\rho_i(r)}{\epsilon_o}$$

Giving

$$E = \sum_{n_1,n_2,n_3} \sum_i \sum_j{}' \int_r \int_{r'} \frac{\rho_i(\vec{r})\rho_j(\vec{r}')d^3\vec{r}d^3\,\vec{r}'}{8\pi\epsilon_o|\vec{r} - \vec{r}' + n_1\vec{T_1} + n_2\vec{T_2} + n_3\vec{T_3}|} \tag{2.9}$$

Van der Waals interaction

Van der Waals interactions occur between nearby atoms which are not chemically bonded. These interactions are strongly repulsive below a threshold and weekly attractive beyond it. The repulsive interactions are mainly due to Pauli Exclusion force and the attractive interactions are due to induced dipole. The attractive van der Waals, however, decay rapidly with distance. Lennard-Jones potential is usually used to represent van der Waals interactions.

$$V_{LJ} = \epsilon \left[\left(\frac{r_m}{r} \right)^{12} - 2 \left(\frac{r_m}{r} \right)^{6} \right] \tag{2.10}$$

where, ϵ is the depth of the potential well and r_m is the equilibrium distance.

2.2.3 Hydrogen Bonding

A hydrogen bond is an electrostatic attraction between a hydrogen atom of one polar group (called donor) and an electronegative atom of another polar group (called acceptor). Such interaction occurs between polar groups which have hydrogen atom covalently bonded to a highly electronegative atom such as nitrogen, oxygen or fluorine. Since a hydrogen bond is a phenomenological description of the electrostatic interaction between polar groups, it is usually not necessary to have an explicit H-bond term in all-atom MD simulation. Nonetheless, H-bond plays an important role in the behavior of water and organic molecules.

2.2.4 Water Models

One of the most important distinctions between all-atom MD simulation and other forms of numerical simulations (such as Brownian Dynamics) is the use of explicit water. At nanoscale water plays an important role in the dynamics of the system and cannot be taken as just the background noise. However, the inclusion of explicit water is also the major computational cost of all-atom MD simulation.

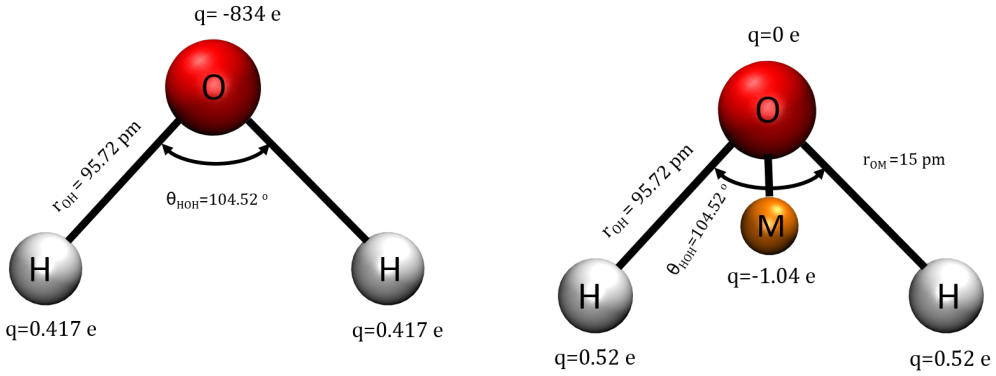

FIGURE 2.1: Tip3p and Tip4p water models with their respective parameters illustrated in the diagram. 'O' and 'H' represent Oxygen and Hydrogen respectively where as 'M' represent the "lone pair" which have zero mass but carry all negative charge.

The two water models I used are Tip3p and Tip4p [27] illustrated in the Fig. 2.1 which are the most commonly used water models. Tip3p have three sites representing the two hydrogens and one oxygen atoms. Tip4p has an additional massless site called lone pair that carries the negative charge of the oxygen atom. The extra degree of freedom in Tip4p helps better represent the electrostatic properties of water.

Water model can also be either rigid or flexible, and for rigid water model, there are algorithms to keep it rigid such as SHAKE [28] or RATTLE [29]. There are several models with a higher number of sites, but the computational cost increases proportionally to the number of sites.

2.2.5 Solvation shell of ions in water

An ion dissolved in water form a solvation shells (also called hydration layers) around it as shown in Fig. 2.2 which is due to the strong electrostatic interaction between the ion and the water dipole. Such shells increase the effective size of the ion in the solution. Ions translocating through pores and channel smaller than it's hydrated size has to shed some of the water molecules from their solvation shell. There is energy penalty associated with the removal of water molecules from the solvation shell of an ion which is called dehydration energy. The dehydration barrier results in nonlinear behavior in ion transport through nanoscale pores and can also lead to ion selectivity. We will be discussing these phenomena in detail in Chapters 4 and 5.

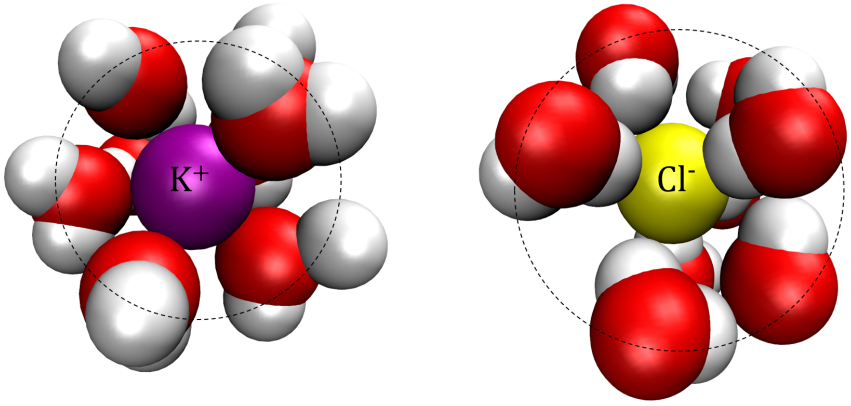

FIGURE 2.2: A snapshot of MD simulation showing the first solvation shell around a K^+ and a Cl^- ion in water. The red and the white spheres represent oxygen atom and hydrogen atom respectively.

2.2.6 Free energy calculation

The free energy of a system along a reaction coordinate is important information in understanding the dynamics of the system along the path. However, often enough, potential along the reaction coordinate is not smooth, and system may spend so much time in a particular state that it become practically impossible to get the good statistically average for the rest of the path. One way to overcome such problem is the Adaptive Biasing Force (ABF) method [30, 31]. In ABF method, a biasing force just enough for the system

to overcome potential barrier is applied so that system moves under random forces along the reaction coordinate. The biasing force needed in turn can be use to calculate the potential landscape of the system.

2.3. Coarse-Grain Models

All-atom MD simulation being computationally expensive may not be practical for the study of phenomena that occur at larger time scale. Also, the atomic level details are not necessary for all cases or can be approximated by some phenomenological model. I will use coarse-grain model to study the thermal transport through DNA.

2.3.1 1D models for DNA denaturation

Bases in a DNA are bonded to their neighboring bases in the same chain by covalent bonds and bonded to the complementary bases in the second chain by hydrogen bonds. Because the covalent bonds are much stronger than hydrogen bonds one can ignore the extension of covalent bonds (say x_n) compare to the extension of hydrogen bonds (say y_n). With this approximation, the fluctuation of DNA reduces to one-dimensional form:

$$H = \frac{1}{2}\sum_n \dot{y}_n^2 + \sum_n V(y_n) + \sum_n W(y_n, y_{n+1}) \tag{2.11}$$

where, V is the onsite potential, and W is the nearest neighbor coupling.

PB model

Morse potential can be used to represent the onsite potential. However it is not clear what should be the form of the nearest neighbor interaction. The simplest choice is to use a harmonic coupling and thus the hamiltonian becomes

$$H = \frac{1}{2}\sum_n \dot{y}_n^2 + \sum_n D_n(1 - e^{ay_n})^2 + \sum_n \frac{k_n}{2}(y_n - y_{n-1})^2, \tag{2.12}$$

where, D_n, k_n, and a are coefficients that depends on the interaction pair. This model is called Peyrard-Bishop (PB) model [32].

PBD model

PB model was later modified to account for the sharp melting curve of DNA by introducing an anharmonic coefficient depended on the extension of bond nearest for the neighbor coupling,

$$H = \frac{1}{2}\sum_n \dot{y}_n^2 + \sum_n D_n(1-e^{ay_n})^2 + \sum_n \frac{k_n}{2}[1+\rho e^{-\alpha(y_n+y_{n-1})}](y_n-y_{n-1})^2, \qquad (2.13)$$

where, ρ and α are constants. This model is called Peyrard-Bishop-Dauxois (PBD) model [33, 34].

JB model

Marc Joyeux and Sahin Buyukdagli [35] presented an alternative to PBD model for DNA denaturation. They argue that PBD model do not take into account that stacking interactions are necessarily finite. So they argue that this potential should be of the form

$$W(y_n, y_{n+1}) = \min[\frac{1}{2}\Delta H, \frac{1}{2}K(y_n - y_{n+1})^2].$$

They choose following form of potential.

$$W(y_n, y_{n+1}) = \frac{\Delta H}{2}(1-e^{-b(y_n-yn+1)^2}) + k_B(y_n-y_{n+1})^2$$

Here the first term is the switch function which switch the potential from harmonic to a constant as $(y_n - y_{n+1})^2$ increases and second term is added to account for the stiffness of sugar/phosphate bond, without which each strand would break into smaller strands at large $(y_n - y_{n+1})^2$. Nevertheless, k_B is much smaller than K used in PBD model.
The results from transfer integral method Fig. 2.3.1 shows that this model gives similar melting curve as PBD model.

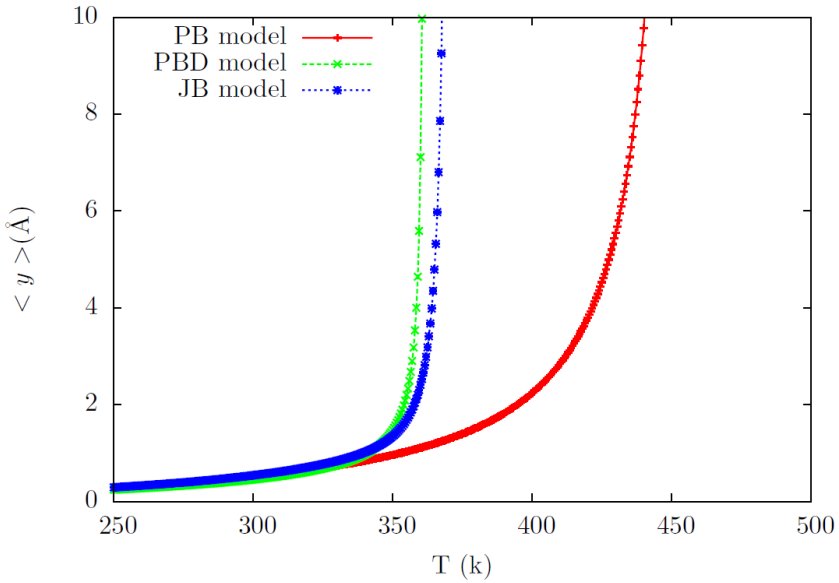

FIGURE 2.3: Melting curve of DNA according to the various 1D model.

The melting curves for homogeneous DNA strands using all those three models are shown in Fig. 2.3.1. The melting temperature is different for different models. It is sharper for the anharmonic models (PBD and JB) and less sharp for the harmonic model (PB).

2.4. Summary

Thus in this chapter, I laid out the general methodology used for my research and presented the technique to deal with the computational complexities that arise due to a large number of particles involved in our problems. The other chapters in this thesis will deal with case-specific problems.

3. CROSSOVER BEHAVIOR OF THE THERMAL CONDUCTANCE AND KRAMERS' TRANSITION RATE THEORY

Kramers' theory frames chemical reaction rates in solution as reactants overcoming a barrier in the presence of friction and noise. For weak coupling to the solution, the reaction rate is limited by the rate at which the solution can restore equilibrium after a subset of reactants have surmounted the barrier to become products. For strong coupling, there are always sufficiently energetic reactants. However, the solution returns many of the intermediate states back to the reactants before the product fully forms. Here, we demonstrate that the thermal conductance displays an analogous physical response to the friction and noise that drive the heat current through a material or structure. A crossover behavior emerges where the thermal reservoirs dominate the conductance at the extremes and only in the intermediate region are the intrinsic properties of the lattice manifest. Not only does this shed new light on Kramers' classic turnover problem, this result is significant for the design of devices for thermal management and other applications, as well as the proper simulation of transport at the nanoscale. The work in this chapter is performed in collaboration with Kirill Velizhanin, Chih-Chun Chien and Yonatan Dubi and has been previously published in Ref. [36] and have been presented in 2015 APS March Meeting [37].

3.1. Introduction

Thermal transport is an important process in micro- and nano-scale technologies. It is often in a precarious position: On the one hand, thermal management strategies, including the engineering of low-resistance interfaces, become increasingly important as elements in electronic devices approach the atomic level. On the other hand, *phononics* – phonon analogues of electronics – seek tunability and inherently nonlinear behavior to make functional devices [38]. Thermal transport is thus at the forefront of nanotechnology

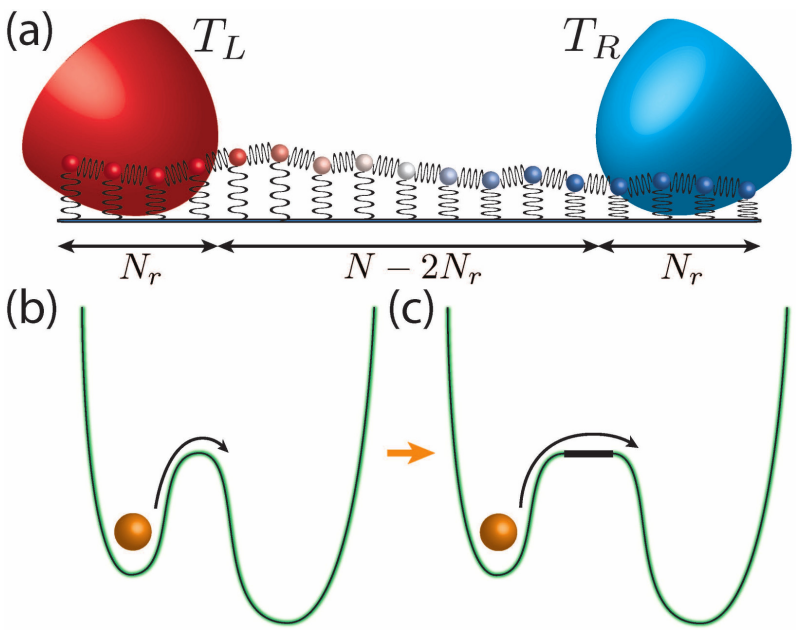

FIGURE 3.1: Thermal conductance and Kramers' transition rate problem. (a) Schematic representation of a one-dimensional lattice of length N, with N_r sites on each side connected to independent Langevin reservoirs at temperatures T_L and T_R. (b) Kramers' problem where noise assists the escape of a classical particle from a metastable state. The green contour of the double-well potential outlines the region where the classical particle is subject to Langevin dynamics. (c) A modified double-well potential where the barrier is deformed horizontally into a region (thick black line) where only ballistic dynamics occurs, i.e., no friction or noise.

research. Its impact in a broad array of applications has sparked advanced methods of the fabrication, control, and measurement of transport in, e.g., carbon nanotubes and single-molecule junctions [39, 40, 38].

Moreover, thermal transport is at the center of one of the major unresolved puzzles in theoretical physics, the absence of a derivation of Fourier's law of heat conduction from a microscopic Hamiltonian [5, 41, 42, 43, 44, 45]. This is related to the seminal work of Fermi, Pasta and Ulam (FPU) [46, 47, 48], which demonstrated that nonlinearity does not always lead to thermalization. The considerations of FPU also apply to the emergence of a well-defined thermal conductivity. The role of nonlinearity – in addition to the description of the thermal reservoirs and interfacial regions – is thus the central topic of many studies examining thermal transport (see Refs. [49, 41, 50] for recent reviews).

In this work, we demonstrate that thermal transport goes through three physically

distinct regimes as the coupling to the surrounding environment – the reservoir that supplies the heat – changes. For weak coupling, energy input from the reservoir limits the heat current through the entire system. For strong coupling, the lattice dynamics are distorted by the presence of the reservoir and this dominates the conductance. Thermal transport is determined by the intrinsic parameters of the lattice only in the intermediate regime. These three distinct regimes exist regardless of whether the system has a well-defined conductivity or not, as we will show by theoretically studying paradigmatic examples of thermal transport [51, 41, 49, 52, 53]. The dependence of thermal conductance on the strength of coupling to reservoirs is physically analogous to the friction-induced turnover in Kramers' reaction rate problem for chemical reactions in solution.

3.2. Methods

Harmonic Lattices. The harmonic lattices we consider are described by the Hamiltonian

$$H = \frac{1}{2}\sum_{n=1}^{N} m\dot{x}_n^2 + \frac{D}{2}\sum_{n=1}^{N} x_n^2 + \frac{K}{2}\sum_{n=0}^{N}(x_n - x_{n+1})^2, \tag{3.1}$$

where x_n is the coordinate of the n^{th} oscillator, m is the mass, D is the strength of the on-site potential, and K is the nearest-neighbor coupling constant. The entire lattice is split into three regions: $N_r \geq 1$ sites on the left end (L) and on the right end (R) serve as *extended reservoirs* as each site (i.e., oscillator) in these regions is coupled to its own "external" Langevin reservoir of temperature T_L and T_R , see Fig. 3.1(a). The friction coefficient γ gives the strength of the coupling to the external reservoirs and is taken to be the same on the both ends for simplicity. The remaining $N - 2N_r$ sites in the middle comprise the *free lattice* (F). This is a generalization of a widely used model that sets $N_r \equiv 1$ [51, 54, 49]. In addition to being a prototypical model of thermal transport, it is also relevant to realistic systems, such as the high- and low-temperature limits of coarse-grained models of DNA [55, 12], where the on-site potential term represents the binding of interstrand base pairs. We also connect two additional sites x_0 and x_{N+1} to the ends

of the lattice, which are fixed at zero. The Langevin equations of motion are

$$m\ddot{x}_n + Dx_n + K[2x_n - x_{n-1} - x_{n+1}] = f_n(t), \tag{3.2}$$

where the l.h.s. describes the Hamiltonian dynamics and the r.h.s. is the reservoir-induced noise and friction forces, $f_n(t) = \eta_n(t) - \gamma_n \dot{x}_n(t)$. The noise $\eta_n(t)$ and friction coefficient γ_n are related by the fluctuation-dissipation relation

$$\langle \eta_n(t)\eta_m(t')\rangle = 2\gamma_n k_B T_n \delta_{nm}\delta(t-t'). \tag{3.3}$$

The three regions of the lattice (L, F and R) are encoded in equations of motion by setting

$$\gamma_n = \begin{cases} \gamma, & n \in L \text{ or } R \\ 0, & n \in F \end{cases} \tag{3.4}$$

and $T_n = T_L$ or T_R for $n \in L$ or R, respectively. Here, a collection of independent (uncorrelated) single site Langevin reservoirs approximates the contact to the thermal reservoir [56]. When $T_L = T_R = T$, the lattice will relax into an equilibrium state at temperature T, as guaranteed by the fluctuation-dissipation theorem. When $T_L \neq T_R$, a heat current will flow (we assume $T_L > T_R$ without loss of generality).

The current flowing from site n to $n+1$ is given by [51, 56]

$$J_n = K\langle \dot{x}_{n+1} x_n \rangle, \tag{3.5}$$

where the average is over the statistical ensemble. For $n \in F$, J_n will be independent of n, i.e., $J_n \equiv J$, in the steady state.

We note that thermal transport occurs ballistically in a frictionless harmonic lattice. This results in a diverging *conductivity*, which can be defined as $\lim_{N\to\infty}(N-2N_r)\sigma$ at fixed N_r. However, the conductance, σ, is well defined and is rapidly converging to its value corresponding to an infinite lattice, as shown in the inset of Fig. 3.2. Henceforth, we always assume $N \to \infty$ at fixed N_r for homogeneous harmonic lattices. Dimensional

analysis shows that the conductance of a uniform harmonic lattice in the limit $N \to \infty$ takes the form (see Appendix for the derivation)

$$\sigma = \frac{J}{\Delta T} = k_B \sqrt{\frac{K}{m}} C\left(\frac{D}{K}, \frac{\gamma}{\sqrt{mK}}, N_r\right), \tag{3.6}$$

where $\Delta T = T_L - T_R$ and C is a as of yet unknown dimensionless function of three dimensionless arguments. This expression implies that harmonic lattices with distinct values of parameters are nevertheless physically similar if $\sqrt{K/m}$, D/K, $\gamma/\sqrt{mK}$, and N_r are identical. Such models can be said to form a "similarity class". In what follows, all the figures pertaining to the harmonic case are plotted in natural units, i.e., γ is plotted in units of $\sqrt{mK}$, σ is plotted in units of $k_B\sqrt{K/m}$, etc. Note that we use ΔT defined with the external reservoir temperatures T_L and T_R, as these are the ones typically set/measured experimentally.

For the anharmonic lattice, the setup is the same as for harmonic lattices, but with the equation of motion given by its respective Hamiltonian.

Numerical Methods. For anharmonic lattice the evolution of the coordinates is computed using the Brünger-Brooks-Karplus integrator with a time step of 10 fs. The total length of the simulation varies from 0.1 ms to 2 ms depending on the convergence of current. The temperature difference between the hot and cold reservoirs was maintained at 9.3K for all calculations. The parameters used are same as in Ref. [34], i.e., $\tilde{D} = 0.04$ eV, $a = 44.5$ nm^{-1}, $\tilde{K} = 4$ eV/nm^2, $\rho = 0.5$, $b = 3.5$ nm^{-1}, and $m = 300$ u.

3.3. Results

The first model we examine is a classical one-dimensional (1D) uniform lattice of N harmonic oscillators as described in Eq. (3.1). Figure 3.2 shows the thermal conductance, defined as the heat current divided by $\Delta T = T_L - T_R$, for an infinite harmonic lattice with $N_r = 100$. A detailed description of the calculation is given in Appendix. Three qualitatively distinct regimes, which are labeled (1), (2) and (3), are apparent in the

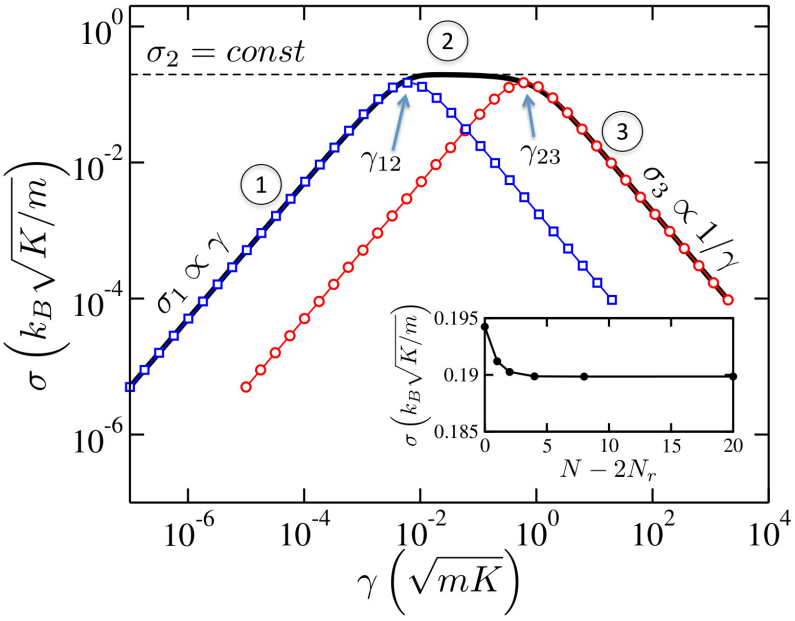

FIGURE 3.2: The thermal conductance of a harmonic lattice with $D/K = 1$, $N_r = 100$, and $N \to \infty$. The numerical results are shown as the thick black line. The analytical results for $N_r \equiv 1$, Eq. (3.10), are plotted as $\sigma_{CL}(\gamma)$ (red circles) and $\sigma_{CL}(N_r\gamma)$, i.e., the horizontal axis is scaled with N_r (blue squares). The inset shows the dependence of σ on $N - 2N_r$ at $\gamma = 0.1\sqrt{mK}$.

figure. We start by examining regime (2), where the conductance depends on γ only very weakly. The magnitude of the conductance on this plateau coincides with the *intrinsic conductance* of the lattice. For the anharmonic lattice we consider later on, the intrinsic conductance behaves as $\sim 1/N$ at large N, so there is a well-defined intrinsic *conductivity* in this plateau region, defined as the conductance multiplied by N in the limit $N \to \infty$.

3.3.1 Intrinsic conductance

We find the *intrinsic conductance* of the harmonic lattice by solving an auxiliary problem of heat current between two semi-infinite ballistic (i.e., no friction) lattices. These lattices are initially disconnected and equilibrated at respective temperatures T_L and T_R. When connected, the heat current flowing from left to right is $J_{L\to R} = k_B T_L l_L^{-1} \sum_{q>0} v_q$, where v_q is the group velocity of a phonon with momentum q (restricted to phonons moving to the right, i.e., $q > 0$) and l_L is the length of the left lattice. Essentially, this expression is just the amount of classical energy stored in a specific phonon mode in

equilibrium ($k_B T_L$), multiplied by its group velocity (v_q) and the local phononic density of states ($1/l_L$). Similarly introducing $J_{R\to L}$, taking the limit $l_L, l_R \to \infty$, and defining the total current as $J = J_{L\to R} - J_{R\to L}$, we obtain the intrinsic conductance as

$$\sigma_2 \equiv \frac{J}{\Delta T} = \frac{k_B}{2\pi}\int_\Omega dq\, v_q = \frac{k_B}{2\pi}\int_\Omega dq\, \frac{d\omega(q)}{dq} = \frac{k_B \Omega}{2\pi}, \tag{3.7}$$

where $\Omega = \omega_{\max} - \omega_{\min}$ is the phonon bandwidth. This conductance is also expressible as $\sigma_2 = \bar{v}_q/2$, where $\bar{v}_q$ is the group velocity averaged over the entire band, which gives additional insight into its form. The eigenmodes of the Hamiltonian, Eq. (3.1), obey $\omega^2 = \left[D + 4K\sin^2(q/2)\right]/m$, so that $\omega_{\min} = \sqrt{D/m}$, $\omega_{\max} = \sqrt{(D+4K)/m}$, and, therefore, the phonon bandwidth is

$$\Omega = \sqrt{\frac{K}{m}}\left[\sqrt{D/K + 4} - \sqrt{D/K}\right]. \tag{3.8}$$

Accordingly, the intrinsic conductance becomes

$$\sigma_2 = \frac{k_B}{2\pi}\sqrt{\frac{K}{m}}\left[\sqrt{D/K + 4} - \sqrt{D/K}\right]. \tag{3.9}$$

The intrinsic conductance is the maximum possible conductance of a harmonic system between two equilibrium reservoirs at different temperatures: No matter how much energy the reservoirs can pump into the system, the free lattice itself can not usher the energy from source (L) to sink (R) faster than the rate allowed by its intrinsic conductance. The magnitude of σ_2 is plotted in Fig. 3.2 (thin dashed line), showing an excellent agreement with the numerically calculated conductance in regime (2) (hence the subscript of σ_2). We also note that decreasing D – the onsite confining potential – and holding all other factors fixed increases the conductance, an effect that is observed in models of DNA denaturation [55, 12]. This is purely due to the increasing bandwidth.

Casher-Lebowitz formula. The other two regimes, (1) and (3), become physically transparent when using the Casher-Lebowitz formula [51] for a *single-site reservoir* at each

end (i.e., $N_r \equiv 1$)

$$\sigma_{CL}(\gamma) = \frac{k_B\gamma}{2\pi m}\int_0^{2\pi} dq\, \frac{\sin^2 q}{1+\frac{2\gamma^2}{mK}\left[1+\frac{D}{2K}-\cos q\right]}. \tag{3.10}$$

It is readily seen that the small and large γ expansion of the expression yields $\sigma_{CL} \propto \gamma$ and $\sigma_{CL} \propto 1/\gamma$, respectively. In fact, very general perturbative arguments suggest that these $\sigma \propto \gamma$ and $\sigma \propto 1/\gamma$ regimes are generic for arbitrary harmonic lattices, as we show in Appendix.

Eq. (3.10) is plotted in Fig. 3.2 as a function of two different arguments: the bare friction coefficient, $\sigma_{CL}(\gamma)$ (red circles), and the scaled friction coefficient, $\sigma_{CL}(N_r\gamma)$ (blue squares). As is seen in the figure, they coincide with numerical results at large and small γ, respectively, which we will now explain.

Small γ regime. The small γ expansion of Eq. (3.10) is $\sigma_{CL} = \frac{k_B\gamma}{2\pi m}\int_0^{2\pi} dq\, \sin^2 q = \frac{k_B\gamma}{2m}$. This expression reflects the fact that energy is pumped in/out of the system via the end sites at a rate proportional to γ, and this rate is much smaller (at low γ) than the one the free lattice can carry *intrinsically*, σ_2. At these conditions (i.e., $k_B\gamma/m \ll \sigma_2$), the heat input by the noise term in Eq. (3.2) is so inefficient that the system has enough time to equilibrate at some global temperature T'. In this quasi-equilibrium state the noise-induced heat current entering the left reservoir is $J_L = \frac{\gamma}{m}k_B(T_L - T')$, and similarly for the right reservoir $J_R = \frac{\gamma}{m}k_B(T_R - T')$. At the steady state $J = J_L = -J_R$, which yields $T' = \frac{T_L+T_R}{2}$, so that the conductance of the entire system becomes $\sigma = \frac{k_B\gamma}{2m}$, in full agreement with the low-γ expansion of Eq. (3.10) above.

These quasi-equilibrium-based considerations can be straightforwardly generalized to the case of extended reservoirs of arbitrary size N_r yielding

$$\sigma_1(\gamma) = \frac{k_B N_r\gamma}{2m} \equiv \frac{k_B\Gamma}{2m}, \tag{3.11}$$

i.e., the heat is pumped into the system at a rate proportional to cumulative friction constant $\Gamma = N_r\gamma$. This is the reason why Casher-Lebowitz formula (3.10), once plotted as a function of the *cumulative* friction constant, $\sigma_{CL}(N_r\gamma)$, coincides with the numerical

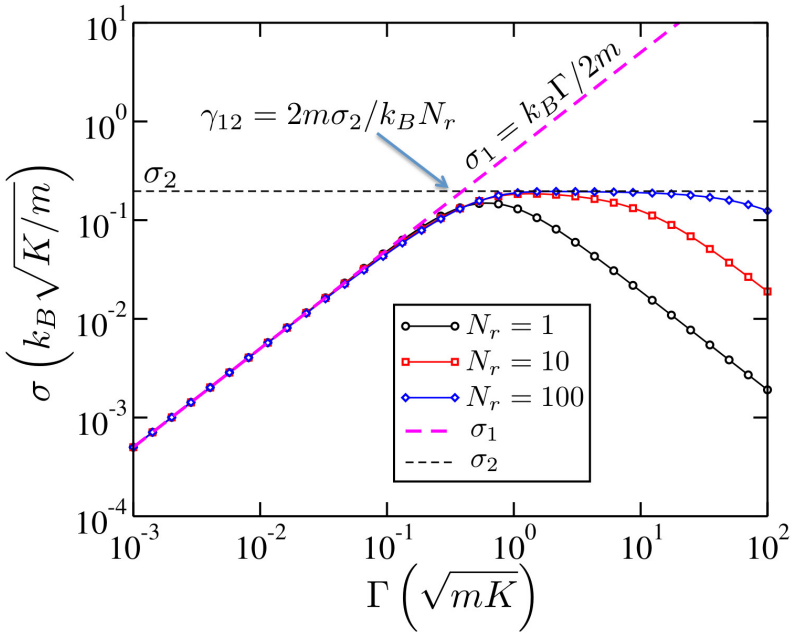

FIGURE 3.3: Comparison of numerical (circles, square, diamonds) and analytical results (dashed lines) in the small Γ regime at $D/K = 1$ for different sizes of extended reservoirs, N_r.

results in Fig. 3.2 at low γ. The agreement between Eq. (3.11) and numerical results in the weak friction regime is emphasized in Fig. 3.3 where conductances for a range of N_r exactly overlap with $k_B\Gamma/2m$ at small friction.

Eq. (3.11) is only valid at sufficiently small Γ. When $\frac{k_B\Gamma}{2m}$ becomes higher than σ_2, the free lattice cannot transfer all the heat the Langevin reservoirs are able to supply. At that point, i.e., $\gamma \approx \gamma_{12} = 2m\sigma_2/k_B N_r$ (marked in Figs. 3.2 and 3.3), the conductance of the overall system levels off and regime (2) is established.

Large γ regime. The large γ expansion of Eq. (3.10) is

$$\sigma_3 = \frac{k_B K}{2\gamma}\left(1 - \frac{\sqrt{mD}}{2K}\Omega\right). \tag{3.12}$$

At large γ, the noise term in Eq. (3.2) can efficiently supply heat to a lattice site. However, this site is effectively decoupled from the adjacent sites since the very large friction *overdamps* its motion resulting in the reservoir site becoming "off-resonant" from the rest

of the lattice. We will discuss this in detail in the next section. Heuristically, however, the efficiency of heat transfer from the reservoir site to the free lattice has to be proportional to a phonon group velocity and to a time the reservoir site can stay coherent with the rest of the lattice. The latter is given by the decoherence time of an overdamped oscillator, $1/\gamma$, so the conductance becomes (averaging over all phonon modes) $\sigma_3 \approx \frac{1}{\gamma}\int_\Omega d\omega\, v_q(\omega)$. This coincides with Eq. (3.12) up to a constant prefactor.

This heuristic argument is directly applicable to the case of extended reservoirs ($N_r > 1$). Indeed, the reservoir site directly connected to the free lattice is the one that excites phonons in the free lattice and the remaining $N_r - 1$ reservoir sites (on the left or on the right) are decoupled from the lattice by at least another order of $1/\gamma$. This entails that the heat conductance is independent of N_r in the large-γ regime, which agrees with the numerical results in Fig. 3.2. When $\sigma_3(\gamma)$ reaches σ_2 as γ decreases to $\gamma \approx \gamma_{23} = \frac{k_B K}{2\sigma_2}\left(1 - \frac{\sqrt{mD}}{2K}\Omega\right)$ (marked in Fig. 3.2), there is a crossover from regime (3) to (2). That is, as γ decreases the reservoir site becomes coherent enough to efficiently transfer heat to the free lattice, so the finite intrinsic conductance of the free lattice, σ_2, becomes the limiting factor.

The plateau and tilt. Regime (2) is just a crossover point at $N_r = 1$ [Eq. (3.10)], but it becomes a pronounced plateau at $N_r \gg 1$ as shown in Fig. 3.3. This is because the position of the crossover between regimes (2) and (3), γ_{23}, does not depend on N_r, but the one between regimes (1) and (2), does as $\gamma_{12} \propto 1/N_r$. At sufficiently large N_r the two crossovers are thus well separated, establishing a plateau in between.

Closer inspection of the numerical results reveals that the "plateau" is in fact tilted, see Fig. 3.4. The linear fit of this tilted plateau yields an intercept with the $\gamma = 0$ axis numerically close to σ_2 and the slope independent (within the fitting accuracy) of any parameters of the lattice.

We demonstrate below that once $N_r \to \infty$, the conductance becomes σ_2 as $\gamma \to 0$ (the order of taking the two limits is important: the limit of $N_r \to \infty$ is assumed to be taken first, i.e., $\Gamma = N_r\gamma \to \infty$). When γ is finite, though, the conductance falls off linearly with γ with a *universal* slope. This tilt can be understood via the inhomogeneity of the

lattice. For example, connecting lattices that have only partially overlapping phonon bands results in a poor conductance due to scattering at the interfaces [57]. In our situation, the phonons in the extended reservoirs and the free lattice are *different* because of a finite phonon lifetime in the former (due to friction) and an infinite lifetime in the latter. Within the extended reservoir, each phonon has a spread in frequency $\delta\omega \approx \gamma$. This smearing results in imperfectly overlapping bands at the band edges, which in turn leads to a decreasing conductance as γ increases.

The more rigorous understanding of the tilt can be achieved by considering phonon scattering at the interface between a free lattice and a lattice with uniform friction γ (K and D are the same for both). For a phonon of frequency ω incoming from the free lattice, the solution within the free lattice is $x_n(t) = e^{iqn-i\omega t} + Ae^{-iqn-i\omega t}$, where A is the reflection amplitude. The solution in the lattice with friction is $x_n(t) = Be^{iq'n-i\omega t}$, where q' has a non-zero imaginary component due to the finite phonon lifetime. Imposing the boundary conditions, the reflection amplitude is

$$A(q) = -\frac{1 - e^{-i(q'-q)}}{1 - e^{-i(q'+q)}}, \tag{3.13}$$

where $\cos q' = \cos q - i\gamma\omega/2K$ and $\omega = \omega(q)$ is the phonon dispersion relation for a free lattice. The two limiting cases are $A = 0$ at $\gamma \to 0$ and $|A| = 1$ at $\gamma \to \infty$ with $0 < |A| < 1$ at any finite γ. This justifies the heuristic argument above that phonons with and without friction are indeed different resulting in a finite reflection amplitude at the friction/frictionless interface. At finite γ, the reflection is most significant near the band edges (i.e., within $\delta\omega \approx \gamma$ of $\omega_{\min}$ or $\omega_{\max}$).

In equilibrium at temperature T, the momentum-resolved current from the free lattice to the extended reservoir is $J(q) = k_B T v_q [1 - R(q)]$ for $q > 0$, where $R(q) = |A(q)|^2$ is the reflection coefficient. It is difficult to directly evaluate the current from the extended reservoir to the free lattice, but at equilibrium this current has to fully compensate the one entering the reservoir from the free lattice. Using this correspondence, we can now write down the current from a reservoir to the free lattice even at non-equilibrium conditions. This results in the following set of balance equations for a heat current in a system of a

free lattice between two extended reservoirs,

$$\begin{aligned} J_L(q) - R(q)J(-q) &= J(q), \\ J_R(-q) - R(q)J(q) &= J(-q), \end{aligned} \tag{3.14}$$

where $J(q)$ is the current within the free lattice and $J_{L(R)}$ is the current from the left (right) reservoirs. For example, the first equation states that the current from left to right within the free lattice equals the current from the left reservoir plus the portion of "left" current, $J(-q)$, reflected by the interface with the right reservoir. Solving these equations and integrating over all phonon modes, $\int_0^\pi dq\ [J(q) + J(-q)]$, we obtain

$$\sigma(\gamma) = \frac{k_B}{2\pi} \int_0^\pi dq\, v_q \frac{1 - R(q)}{1 + R(q)}, \tag{3.15}$$

which is similar to Eq. (3.7), except for the quotient within the integrand. This quotient is strictly positive and always less than 1 – it represents the non-vanishing thermal resistance of the interfaces due to phonon scattering and is known as the Kapitza resistance [58]. The low-γ expansion of Eq. (3.15) produces a very simple result

$$\sigma(\gamma) \approx \sigma_2 - \frac{\pi}{48} \frac{k_B \gamma}{m}, \tag{3.16}$$

shown in Fig. 3.4 by blue crosses. As is seen, the universal tilt of $-\pi k_B/48m$ is independent of lattice parameters (except for mass) and in excellent agreement with numerical results in the plateau region. Furthermore, it turns out that Eq. (3.15) evaluated at arbitrary γ (red circles) does not only exactly reproduce the tilted plateau but also the high-γ regime (3). In particular, the large-γ expansion of Eq. (3.15) results in Eq. (3.12). Therefore, Eq. (3.15) is *exact* in the limit of $N_r \to \infty$ and is valid for the "moderate to strong friction" regime. The only regime it cannot reproduce is regime (1) since the limit $N_r \to \infty$ has been taken in the scattering calculation, which stretches the plateau all the way to $\gamma = 0$.

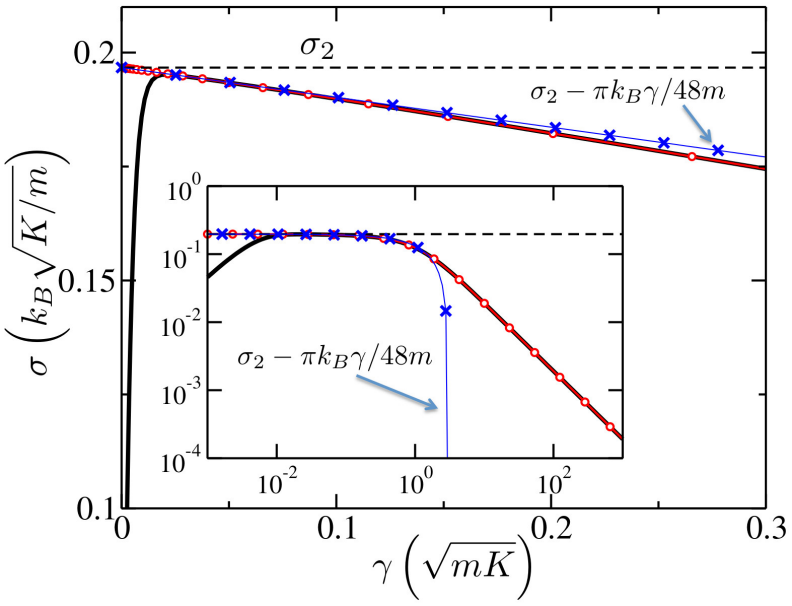

FIGURE 3.4: Comparison of the exact numerical results (thick black line) for the conductance with the semi-analytical result, Eq. (3.15), shown by red circles. The model parameters are $D/K = 1$ and $N_r = 100$. Thin dashed line shows σ_2. The inset shows that the semi-analytic result also works in the large γ regime. For weak friction, Eq. (3.15) reduces to Eq. (3.16), shown by blue crosses.

3.3.2 Kramers' theory

The crossover behavior discussed above is the thermal transport analog of the Kramers' theory for the classical transition rate of a particle out of a metastable well in the presence of friction and noise [59, 60], as depicted in Fig. 3.1(b) for a double-well potential. The rate constant for the transition is $k(E_b, \gamma) = k_0(\gamma)e^{-E_b/k_BT}$, where E_b is the height of the energy barrier and the prefactor $k_0(\gamma)$ depends on γ. Kramers demonstrated that $k_0(\gamma) \sim \gamma$ when γ is small. In general, the energy supplied by the noise to a particle in a certain well is lost either to friction or to the particle leaving this well by overcoming the barrier. The latter energy loss channel dominates when γ is very small so the friction can be essentially neglected. At these conditions, the transition rate is limited by the low rate at which noise can supply energy needed for a particle to overcome the barrier. This rate is linear with respect to γ, resulting in $k_0(\gamma) \sim \gamma$. This behavior is indeed analogous to regime (1) in the thermal transport problem, where the free lattice is very efficient in carrying heat, so the heat current is limited by the rate at which the

Langevin reservoir can input energy into the system, Eq. (3.11).

On the other extreme, as γ becomes very large, Kramers showed that $k_0(\gamma) \sim 1/\gamma$. In this regime, the dynamics of the particle in the Kramers' problem becomes increasingly non-ballistic due to the strong friction and noise. This results in the high probability of *re-crossings*, i.e., even if the particle overcomes the barrier and crosses the surface separating the wells, the very strong noise can still push it back thus preventing its thermalization in the new potential well [60]. The probability of re-crossings grows with γ resulting in $k_0(\gamma) \sim 1/\gamma$.

In order to illustrate the re-crossing phenomenon in the Kramers' problem and emphasize its similarity to the large-γ regime (3) of the thermal transport problem, we deform the barrier in the Kramers' problem as shown in Fig. 3.1(c). Specifically, we "stretch" the very top of the barrier into a horizontal *ballistic* region (i.e., no friction/noise) of a finite length (this is in contrast with the example of Section VII.E of Ref. [59], where dissipation is present everywhere). This modification does not affect the transition rate since if a particle enters this region with a certain velocity, it will leave this region with the same velocity (remember that, within our model, there is no friction in the horizontal region). The only thing that changes by adding this "stretching" is the time required for a particle to cross the barrier – irrelevant in the steady state.

Once a particle reaches the top of the barrier going from the left, it propagates freely along the ballistic region until it reaches the onset of the right well. Upon hitting this onset, the particle immediately becomes subject to noise which, if strong enough, can kick it back to the ballistic region, so the particle might end up in the the well it originally came from. Thus, the particle can be thought of as being *reflected* off the boundary between ballistic and non-ballistic regions. This is the phenomenon of re-crossing – the top of the barrier can be crossed multiple times without thermalization in either of the potential wells.

This perspective demonstrates the analogy to thermal transport at "moderate to strong" γ. Indeed, we were able to describe the thermal transport in regime (2) and regime (3), see inset in Fig. 3.4, by considering *reflections* of phonons off the boundary

between the free lattice (no friction) and one of the reservoirs (friction is present). The ballistic region and the two potential wells in the deformed double-well potential are then respective analogs of the free lattice and the extended reservoirs in the thermal transport problem.

This deep physical similarity between the two problems, when looked upon from the perspective of particle (or phonon) reflection, calls for qualitatively similar behavior as the magnitude of friction varies. Indeed, Eq. (3.15) gives $\sigma \sim 1/\gamma$ at large γ, which matches $k_0(\gamma) \sim 1/\gamma$ in Kramers' problem. Furthermore, at intermediate values of γ, the general Kramers' solution reduces to the transition state theory (TST) rate k_{TST} which does not depend on γ [59, 60]. More accurately, the Kramers' rate equals to k_{TST} with negative corrections linear with respect to γ, so that k_{TST} is always an exact upper limit of the Kramers' rate. This happens as well in the thermal transport problem where the conductance in regime (2) is given by Eq. (3.16). In this equation, σ_2 – an exact upper limit – is an *intrinsic* conductance of the free lattice, which does not depend on friction.

We note that similar arguments can be applied to a version of the Kramers' problem where a classical particle escapes a single metastable potential well [59]. In this formulation, Kramers' problem becomes analogous to a problem of thermal transport through the interface between a free lattice and a lattice with uniform friction studied by us when discussing the tilt of the plateau. In particular, the low probability of phonon transmission through the interface between these two lattices at large γ is analogous to the particle escape rate scaling as $1/\gamma$ in the Kramers' problem of a metastable potential well.

The appealing picture developed above is based on very general and intuitive physical arguments and is, therefore, expected to be valid beyond the specific case of a uniform harmonic lattice. Indeed, below we discuss the two important cases of (i) a harmonic lattice with disorder and (ii) an anharmonic lattice. We demonstrate the existence of three distinct regimes of thermal transport and, therefore, the similarity to Kramers' problem.

3.3.3 Disordered Harmonic Lattice

The Hamiltonian for a harmonic lattice with mass disorder reads as

$$H = \frac{1}{2}\sum_{n=1}^{N} m_n \dot{x}_n^2 + \frac{D}{2}\sum_{n=1}^{N} x_n^2 + \frac{K}{2}\sum_{n=1}^{N-1}(x_n - x_{n+1})^2. \tag{3.17}$$

The mass disorder is realized by sampling mass uniformly and independently for each lattice site within the interval $m_n = m \pm \delta m = m(1.0 \pm 0.3)$, so that the mean mass, m, is the same as in the non-disordered case, Eq (3.1). The central "free" part of the lattice is kept to be $N - 2N_r = 60$ sites long. The sizes of the extended reservoirs are N_r =1, 10 and 100 (the same on the left and on the right in each calculation).

Figure 3.5(a) shows the heat conductance versus γ for a harmonic lattice with mass disorder. The presented numerical results are statistically averaged over the disorder. The crossover behavior is indeed present. Furthermore, when N_r increases the plateau starts to form as it was the case for the homogeneous lattice. However, the magnitude of the conductance at the plateau, $\sigma_2(\text{dis})$, is approximately an order of magnitude lower than $\sigma_2(\text{hom})$ (dashed black line), the latter being the intrinsic conductance of the homogeneous lattice. This is due to disorder-induced finite phonon mean free path being shorter than $N - 2N_r = 60$, which lowers the conductance.

3.3.4 Anharmonic Lattice

To investigate the crossover behavior in an anharmonic lattice we examine the thermal conductance in a paradigmatic nonlinear lattice – the Peyrard-Bishop-Dauxois (PBD) model [32, 34, 33]. The PBD model is a one dimensional lattice that represents nonlinear fluctuations of DNA as it denatures. Here, we are primarily interested in the crossover behavior for a highly nonlinear lattice, rather than the physics of the denaturation transition where the double helix separates into two single strands (the transport physics described by this model has been discussed elsewhere, see Refs. [55, 12]). The Hamiltonian takes on the form

$$H = \frac{1}{2}\sum_{n=1}^{N} m\dot{x}_n^2 + \sum_{n=1}^{N} V(x_n) + \sum_{n=1}^{N} W(x_n, x_{n+1}), \tag{3.18}$$

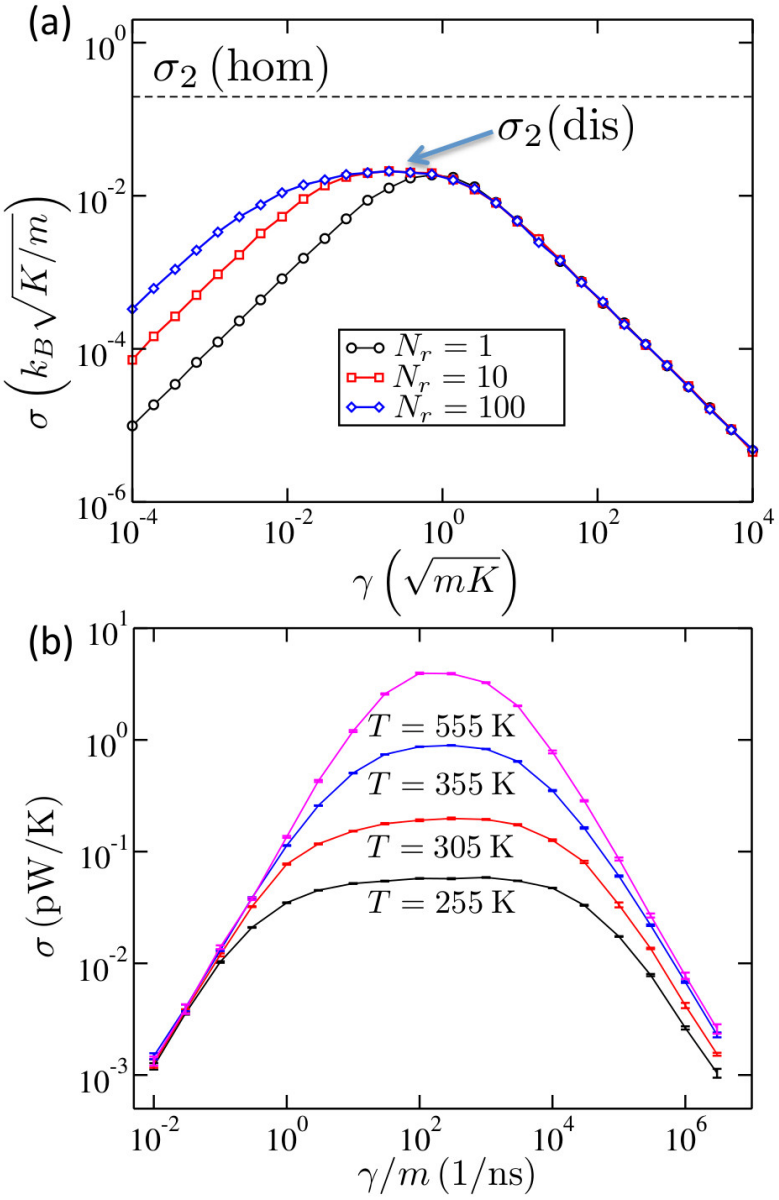

FIGURE 3.5: (a) The thermal conductance of a disordered harmonic lattice with N_r =1, 10 and 100 (black circles, red squares and blue diamonds) and $N - 2N_r = 60$. The system is the same as that in Fig. 3.2, i.e., $D/K = 1$, except for the mass which is now sampled uniformly and independently for each site within the interval $m_n = m(1\pm0.3)$. The dashed line gives the intrinsic conductance for a homogeneous lattice, σ_2(hom), demonstrating that the disorder significantly decreases the heat conductance of the lattice, σ_2(dis) at the plateau. The curve is averaged over 100 to 1000 realizations of the disorder so that magnitude of the error due to the incomplete averaging over disorder is comparable to the thickness of the lines. (b) The thermal conductance of anharmonic PBD lattice with $N_r = 20$ and $N = 100$ for various average temperatures T. The error bars are computed using the range of fluctuations of the cumulative current for the final 10 % of the simulation time.

where x_n represents the base-to-base distance within the n^{th} base pair. The on-site Morse potential $V(x_n) = \tilde{D}(e^{-ax_n} - 1)^2$ represents the hydrogen bonding between the bases and the coupling term $W(x_n, x_{n+1}) = \frac{\tilde{K}}{2}(1 + \rho e^{-b(x_n + x_{n+1})})(x_n - x_{n+1})^2$ gives the stacking interaction. We note that with small amplitude fluctuations (at low temperature) this model is harmonic with parameters $D = 2\tilde{D}a^2$ and $K = \tilde{K}(1 + \rho)$. Similarly, at high temperature, the model is harmonic with parameters $D = 0$ and $K = \tilde{K}$. In between, the model displays highly nonlinear behavior.

The results of simulations, shown in Fig. 3.5(b), clearly demonstrate three regimes of thermal transport. Specifically, $\sigma(\gamma) \sim \gamma$ and $\sigma(\gamma) \sim 1/\gamma$ at small and large γ, respectively. Regime (2), where $\sigma(\gamma) \approx$ constant, is most pronounced at lower temperatures because the extended reservoir size is kept fixed and the conductance is lowest at this point, see the discussion below. We have shown elsewhere that this regime has a well-defined conductivity [12].

Unlike the harmonic model, the intrinsic conductance of nonlinear lattices does in general depend on temperature. In case of the PBD model, the intrinsic conductance of the lattice increases as the average temperature increases across the denaturation transition, which is apparent in the increase of the conductance plateau. This increase is due to the decrease in nonlinearity of the model as the transition is crossed from below. Moreover, the length of the plateau region shortens due to the increasing conductance. At higher temperatures, the crossover from Regime (1) to Regime (2) happens at a larger γ, as the rate of heat input from the reservoir ($\sim \gamma$) has to compete with the intrinsic conductance of the complete reservoir/lattice system. A similar shift in the crossover happens for Regime (2) to Regime (3). In addition to this model, the crossover behavior has been observed in other anharmonic lattices, such as the FPU lattice [41]. We note that for anharmonic lattices the heat conductance can scale nontrivially with the length and temperature, which will result in an intricate interplay between these variables, the extended reservoir size, and the width of the plateau region, as seen in Fig. 3.5(b).

3.4. Discussion

We elucidated the mechanisms behind the crossover behavior of thermal transport as the strength of coupling to the reservoirs is varied. The evidence suggests that this behavior is universal, applying to harmonic, anharmonic, and disordered systems. It is also guaranteed to exist in higher dimensional harmonic systems as well, due to the closed form expression of transport in arbitrary lattices. This phenomenon parallels the physical behavior observed in Kramers' transition state problem. Our results illuminate the regime where the intrinsic conductance is manifest. It is in this regime where nonlinear fluctuations, disorder, etc., dominate the conductance and where thermal transport can be used to probe physical processes, such as DNA denaturation [12, 55]. We also note that in many physical systems, the friction coefficient γ depends on frequency, giving rise to memory in the equations of motion [61, 49, 54]. We expect a crossover to still occur when the overall coupling to the external reservoirs is tuned. The intermediate regime, however, may display more complex behavior due to how the reservoirs affect modes at different frequency scales. We leave this study for a future investigation.

Moreover, non-equilibrium molecular dynamic simulations is the standard tool in the study of thermal transport in nanoscale systems (see, e.g., [62, 63, 64, 65, 40, 66, 67, 68, 69]). In these simulations the strength of coupling to the environment (in the form of, e.g., Langevin or Nose-Hoover thermostats) is a free parameter. It is relatively innocuous when a well-defined conductivity exists. However, when both ballistic and diffusive effects are present – as is the case at the nanoscale – the choice of this coupling affects the calculation of the thermal conductance. It thus must be chosen to appropriately simulate the property of interest, whether it is the thermal conductance of the device or the intrinsic conductance of the functional system. This is especially important when extracting scaling exponents of the conductance versus temperature or lattice length in nonlinear and disordered systems, as both quantities nontrivially affect the conductance and the crossover behavior can spuriously influence the predicted scaling.

4. DEHYDRATION AS A UNIVERSAL MECHANISM FOR ION SELECTIVITY IN GRAPHENE AND OTHER ATOMICALLY THIN PORES

Ion channels play a critical role in regulating cell behavior and in electrical signaling. In these settings, polar and charged functional groups – as well as protein response – compensate for dehydration in an ion-dependent way, giving rise to the ion selective transport critical to the operation of cells. Dehydration, though, yields ion-dependent free energy barriers and thus is predicted to give rise to selectivity by itself. However, these barriers are typically so large that they will suppress the ion currents to undetectable levels. Here, we establish that graphene displays a measurable dehydration-only mechanism for selectivity. This fundamental mechanism – one that depends only on the geometry and hydration – is the starting point for selectivity for all channels and pores. Its likely detection in graphene pores resolves conflicting experimental results, as well as presents a new paradigm for characterizing the operation of ion channels and engineering molecular/ionic selectivity in filtration and other applications. This work was done in collaboration with Massimiliano Di Ventra and was published in [70] and presented in Biophysical Society 61st Annual Meeting [71].

4.1. Introduction

Ionic transport through protein pores underlies many biological processes. Various factors, such as the presence of charges and dipole moments, structural transitions of the pore, dehydration of ions, make the dynamics of biological pores very complex [72, 73, 74, 75, 76, 77, 78]. Solid-state nanopores can delineate these contributions to transport. For instance, a competition of hydrated ion size and pore radius was predicted to result in a drastic drop in ionic conduction [79, 80] – in a way analogous to quantized conductance in electronics – and subsequently observed in graphene laminates [81]. These studies [79, 80], as well as others [82, 83, 84, 85], show that, as expected, ions have different free energy

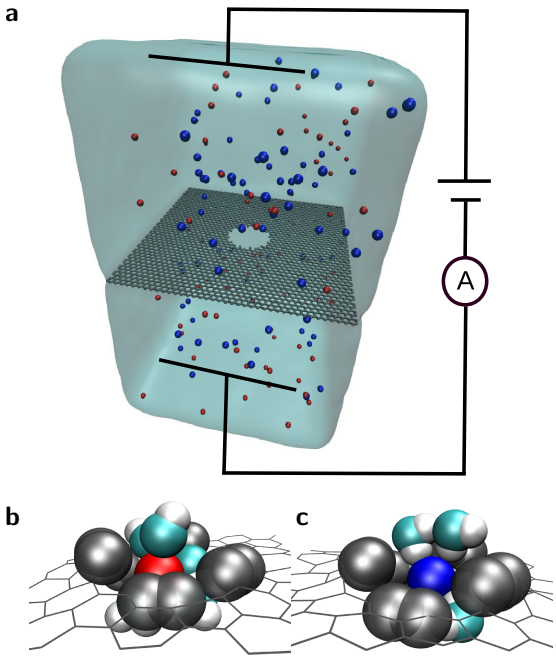

FIGURE 4.1: Schematic of ion transport through a graphene nanopore. (a) An applied bias across the membrane drives an ionic current so that, when the pore is sufficiently small, the ions have to partially shed their hydration layer in order to translocate through the pore. Red and blue spheres represent K^+ and Cl^- ions, respectively. Water is shown as a continuum even though we use an all-atom model for this work. (b) A potassium ion and (c) a chloride ion crossing the pore maintain significant hydration, unlike in long, narrow pores. Carbon at the edge of the pore, oxygen, and hydrogen are gray, cyan, and white spheres, respectively.

barriers due to dehydration, allowing dehydration to yield selectivity on its own. However, the large free energy barriers for ions to enter a long pore greatly suppress the current from all ions, making this selectivity difficult to resolve [86].

Due to its atomic thickness, one expects graphene may provide a suitable membrane to detect and exploit dehydration-only selectivity, as we will discuss here. Several recent experiments give tantalizing results in this direction. For instance, Ref. [2] finds that the graphene membrane they use has a small – but measurable – conductance when no pores are present, which they attribute to defect channels. Salts, XCl, with X=Cs^+, Rb^+, K^+, Na^+ and Li^+, give conductances that slightly deviate from what their bulk conductivities would predict. However, as their Table 1 and our Table 4.3 show, the discrepancy is small (less than 50 %). In fact, if the defect channels – the structure of which is not known – are

cation selective due to the presence of negative charges, the *bulk properties* almost perfectly predict the observations. Moreover, the difference in hydration energies is large and not expected *a priori* to give such a small deviation in conductance. The considerations here suggest that dehydration is likely *not* responsible for the small deviation in membrane-only conductance in Ref. [2].

In a similar vein, Ref. [3] finds weak monovalent cation selectivity over divalent cations for sub-2 nm pores. However, the pores had a large variability in conductance over time (see their Fig. 3). Within these uncertainties, the data may be explained by the different mobilities alone, as we show in Table 4.4. Moreover, Ref. [87] recently found highly selective (K^+ over Cl^-) graphene pores, where a charged graphene membrane is the likely cause since the selectivity persists for large pore sizes. These membranes also showed a weak monovalent cation selectivity over divalent cations for pores that were 2 nm to 15 nm in diameter. Indeed, for pores in the 2 nm to 6 nm range, the selectivity was the same magnitude as that observed by Ref. [3], who also indicate their pores are charged. These considerations suggest, as well, that dehydration is not the cause of selectivity in Ref. [3].

The strongest evidence for a hydration effect in transport comes not from nanopores but from nanochannels in graphene laminates. Ref. [81] show that channels with a height of ≈ 0.9 nm allow atomic and small molecular ions to permeate but exclude larger molecular ions, and this exclusion is correlated with hydrated radius (as those authors discuss, adsorption may be playing a role in addition to steric hindrance of the water shell). This height, though, is above the scale necessary to mimic and understand biological ion channels.

Another recent study, however, finds selectivity of K^+ over Cl^- in porous graphene [1]. This selectivity drops rapidly when the (mean) pore diameter increases by about 0.1 nm to 0.2 nm. Those authors attribute this selectivity to the presence of charges. However, this rapid drop in selectivity is a tell-tale signature of dehydration. Moreover, this is selectivity of a mono-atomic ion over another (ones with almost identical mobilities), just as in biological systems. We will show that the selectivity they find (≈ 1.8 to 2.5 for a

pore radius of ≈ 0.2 nm) is consistent with the partial dehydration ions experience when going into atomically "thin" pores with a radius in the sub-nanometer scale. This is the first direct evidence of dehydration-only in selectivity nanopore experiments.

4.2. Methods

4.2.1 Molecular Dynamics

Graphene has carbon atoms located at the points $\hat{r}_{nm} = m\hat{a}_1 + n\hat{r}_2$ for m, $n \in \mathbb{Z}$, where $\hat{a}_1 = a(3, \sqrt{3})/2$ and $\hat{a}_2 = a(3, -\sqrt{3})/2$ are the 2D lattice vectors and $a \approx 0.14$ nm is the C-C bond length. We open a pore of nominal radius r_n at the center of each membrane by removing carbon atoms satisfying the condition $x^2 + y^2 < r_n^2$, with x, y the coordinates of the atom in the $z = 0$ plane. We then immerse the membrane in an aqueous ionic solution, typically with 1 mol/L salt concentration, consistent with experiments. We use the CHARMM27 force field to model the atoms. The carbon atoms are type CA and water molecules are TIP3P from the CHARMM27 force field.

We perform all-atom molecular dynamics (MD) simulations using NAMD [88] with a time step of 1 fs and periodic boundary conditions in all directions. We use a cutoff of 1.2 nm for non-bonded interactions, i.e., van der Waals and electrostatics. However, we use a full electrostatic calculation every 4 fs via the particle-mesh Ewald (PME) method [26]. We first minimize the energy of the system for 4000 steps (4 ps) and then heat it to 295 K in another 4 ps. A 0.5 ns NPT (constant number of particles, pressure and temperature) equilibration using the Nose-Hoover Langevin piston method [89] – to raise the pressure to 101 325 Pa (i.e., 1 atm) – followed by 1.5 ns of NVT (constant number of particles, volume and temperature) equilibration generates the initial atomic configuration. An electric field perpendicular to the plane of the membrane drove the ionic current through the pore. We set the Langevin damping rate to 0.2/ps for carbon and water (via its oxygen atoms) during these runs. Test runs show that damping hydrogen atoms does not affect the results. Damping the ions, however, affects the current as it changes the ionic mobility.

We fix the outer edge of the graphene membrane but the bulk of the membrane has no confinement other than the C-C bonds of graphene. The production runs vary from 100 ns to 1.1 μs based on convergence of the current and other properties of interest. When calculating the water density around an ion fixed at the origin (e.g., in the center of the pore when it is not fluctuating), the parameters are the same except there was no external electric field present.

We use the Adaptive Biasing Method (ABF) [30, 31] in the colvar module of NAMD to perform the free energy calculation. In this method the reaction coordinate, ζ (z for the setup here), is divided into equally spaced bins and the free-energy difference along ζ, is calculated by integrating the equation

$$\langle f_\zeta \rangle_k = -\left\langle \frac{\partial U(X)}{\partial \zeta} - \frac{\partial ln|J|}{\partial \zeta} \right\rangle_k \equiv -\frac{dF(k)}{d\zeta}, \tag{4.1}$$

where $\langle f_\zeta \rangle_k$ and $F(k)$ are the mean force and free energy at bin k, X are the cartesian coordinates, and $|J|$ is the Jacobian of the transformation to cartesian coordinates. The ABF method applies an iterative biasing force, $\bar{f}_n(k)$, which is the average of all force samples after n MD steps in the bin k. This force enables the system to overcome free-energy barriers during an unconstrained MD run and allows for a more uniform sampling along the reaction coordinate. In our simulation, we calculate the one-dimensional free energy profile along the z-axis in bins of width 0.01 nm from $z = -1.5$ nm to $z = 1.5$ nm. We perform ABF calculation on three windows, (-1.5 nm $\leqslant z \leqslant -0.5$ nm), (-0.5 nm $\leqslant z \leqslant 0.5$ nm), and (0.5 nm $\leqslant z \leqslant 1.5$ nm), and also symmetrize the final result about $z = 0$ for better sampling. Also, we confine the ion within a cylinder of radius 0.2 nm centered at the origin, where a bounding potential with force constant ≈ 43 eV/nm^2 turns on outside of the 0.2 nm cylinder. In each bin, 800 samples of the instantaneous force are accrued prior to the full application of the ABF. This biasing force scales up linearly by a factor of 0 to 1 from 400 samples to 800 samples and no biasing force is applied below 400 samples. The total simulation consists of about 120 runs of 10 ns each for each window.

We use the Block Standard Error (BSE) method [90] to compute the error bars for

all plots. The BSE is given by

$$\text{BSE} = \frac{s_\tau \sqrt{\tau}}{\sqrt{T}}, \tag{4.2}$$

where T is the total simulation time (the time of the MD trajectory), τ is a length of time used to partition the simulation into many contiguous blocks, and $s_\tau = \sqrt{\frac{\sum_i (\langle I_\tau \rangle_i - \langle I_T \rangle)^2}{(N_b - 1)}}$ is the standard deviation of the mean current, $\langle I_\tau \rangle$, within each of the N_b blocks. The BSE depends on τ when the latter is very small (i.e., when τ is smaller than the timescale required to get independent reads of the current) or very large ($\tau \approx T$). In the first case, the dependence is due to the fluctuations in the mean being correlated and, in the later case, the estimate of the standard deviation having too few data points. However, the BSE is fairly constant over a broad range of τ in between, which is the value we used to estimate errors. The error bars in the plots are ± 1 BSE unless otherwise indicated.

4.2.2 Pore radius and area

As noted above, we open pores by removing carbon atoms with coordinates satisfying $x^2 + y^2 < r_n^2$. There is a range of r_n that give the same pore size due to the discrete nature of the membrane. We choose r_n to be the maximum of this range. This r_n also gives the distance of the carbon atoms at the pore edge to the center of the pore, see Fig. 4.2 (in other words, the radius of the largest circle that will fit into the pore).

When comparing to experimental results, however, these nominal radii may or may not correspond to the values reported. For instance, Ref. [1] defines the pore area by where electron density is not observed in Transmission Electron Microscopy (TEM) images. This will roughly correspond to $r_n - \sigma_C$ where $\sigma_C \approx 0.17$ nm is the van der Waals (vdW) radius of carbon. This is approximately where the electron density vanishes. Moreover, the actual area available for transport is smaller than nominal area due to the finite size of ions and carbon atoms (note, however, that the flexibility of the pore edge will tend to slightly increase the area available). These factors have negligible effect in larger pores but are significant for sub-nanoscale pores. We found that in general the maximum radial spread of the ion inside the pore is given by: $\rho_{max} \approx r_n - \sigma_C$ (see Fig. 4.3). Thus, we define the effective pore radius as $r_p = r_n - \sigma_C$ and effective area of the pore as $A_p = \pi r_p^2$. This

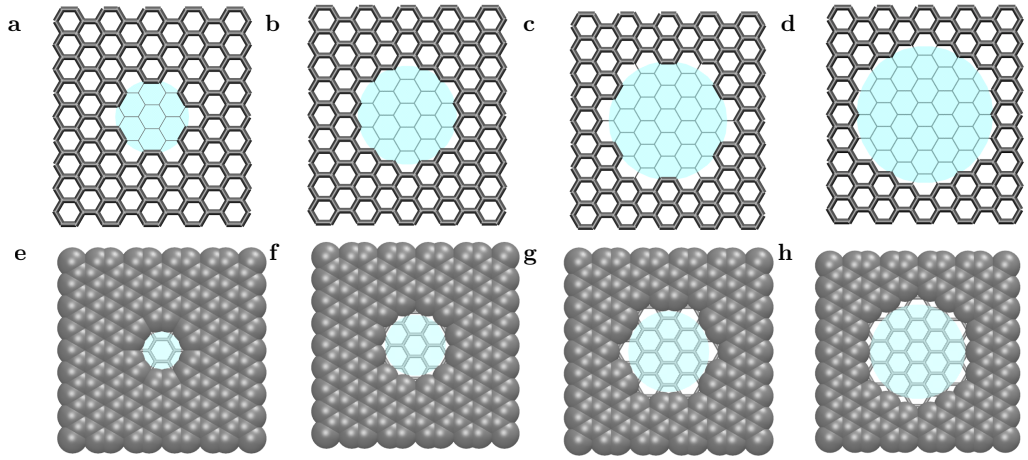

FIGURE 4.2: **Membrane & pore structure.** The images show a small section of the graphene membrane (2.1 nm by 2.1 nm) containing the pore. (a-d) The top panels show the nominal radii, $r_n = 0.38$ nm, 0.51 nm, 0.62 nm, and 0.71 nm. (e-h) The bottom panels show the corresponding effective radii, $r_p = 0.21$ nm, 0.34 nm, 0.45 nm, and 0.54 nm.

definition is both supported by the simulation and should correspond to experimentally observed values. Table 4.1 reports the nominal and effective radii.

r_n (nm)	0.38	0.51	0.62	0.71	0.86	0.93	1.11	1.24	1.36	1.48
r_p (nm)	0.21	0.34	0.45	0.54	0.69	0.76	0.94	1.07	1.19	1.31

TABLE 4.1: **Radii for various pores.** Here, r_n is the nominal radius of the pore (it defines the construction of the pore for the simulations) and $r_p = r_n - \sigma_C$ is the effective radius, where σ_c is the vdW radius of carbon. The quantity $r_p = r_n - \sigma_C$ also gives the radius that would be observed in experiments due to electron density around the carbon atoms and bonds.

4.2.3 Current definition and electric field

The ionic current was calculated using two definitions:

$$I_z(t) = \frac{1}{\Delta t L_z} \sum_{i=1}^{N} q_i [z_i(t + \Delta t) - z_i(t)], \tag{4.3}$$

and

$$I_p(t) = \frac{1}{\Delta t} \sum_{i=1}^{N} q_i (\Theta[Z_i(t + \Delta t)] - \Theta[Z_i(t)]), \tag{4.4}$$

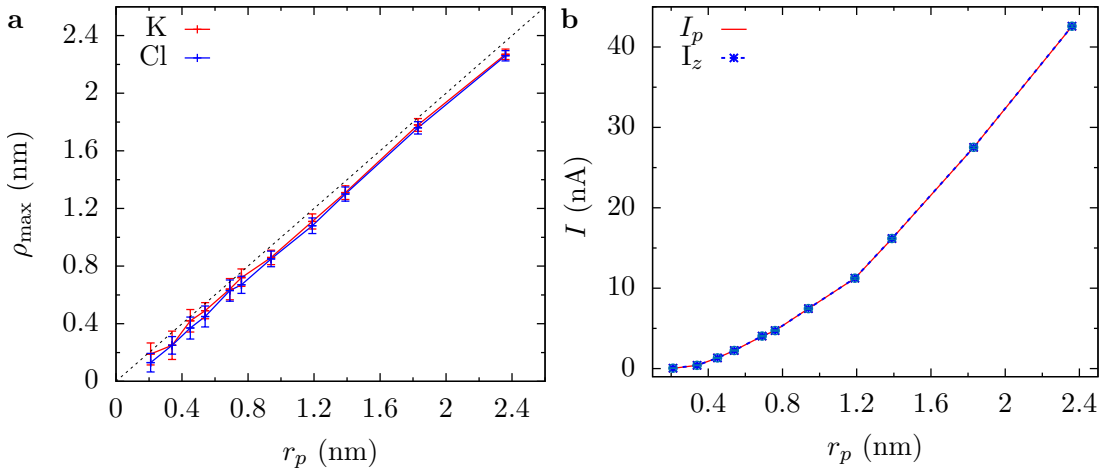

FIGURE 4.3: **Transport area and current definition.** (a) The maximum (cutoff of 99 %) radial spread ($\rho^2 = x^2 + y^2$) of ions inside the pore is roughly equal to r_p nm. That is, when looking at the integrated density of translocation events from 0 to ρ, 99 % of the events fall between 0 and ρ_{max}. (b) Current calculated from the two different definitions I_p (solid line) and I_z (dashed line). Connecting lines are shown as a guide to the eye.

where Θ is the Heaviside step function and $\Delta t = 1$ ps is the measurement time (we record the atomic configuration every Δt increment). The first definition takes into account the motion of all ions in the z-direction and the second definition counts ions crossing the pore. These definitions give the same value for the current so long as the simulation is converged with respect to the total simulation time (see Fig. 4.3(b)).

We found that about 80 % of the potential drops within a sphere of radius r_p from the center of the pore for larger pores (see Fig. 4.4). Thus, the electric field inside the pore can be estimated as $E \approx 0.8\,V/2r_p$. For the smallest pore, however, the electric field is more accurately estimated by $E \approx V/L$ with $L = 1$ nm. This is because vdW repulsion of the ions by the carbon prevents the charge layers from getting closer than about 1 nm.

We tested the effect of box size on the current by comparing different box sizes, a large box (with fixed cross-sectional area 7.4 nm $\times$ 7.4 nm and relaxed height 6.9 nm), a small box (with fixed cross-sectional area 3.7 nm $\times$ 3.7 nm and relaxed height 3.4 nm), and a extended small box (with fixed cross-sectional area 3.7 nm $\times$ 3.7 nm and relaxed height 6.9 nm). The current and selectivity is in agreement (to within the errors reported) for all box sizes when the pore is small and at low voltages, as the current is dominated by the

high pore resistance. The latter allows well-defined charge layers to develop and persist. However, for larger pores, the current was smaller by about 20 % for the larger box size. Since both box sizes have the same voltage and same concentration of ions, the difference in current is likely due to a smaller access resistance and lack of well-defined charge layers in the boxes with smaller cross-sectional area, as the pore diameter approaches the edge of the box. For the smallest pore size calculations, we use the extended small box, as it considerably reduces errors due to convergence in time, i.e., we can run microsecond long simulations, which are necessary when the currents are so small.

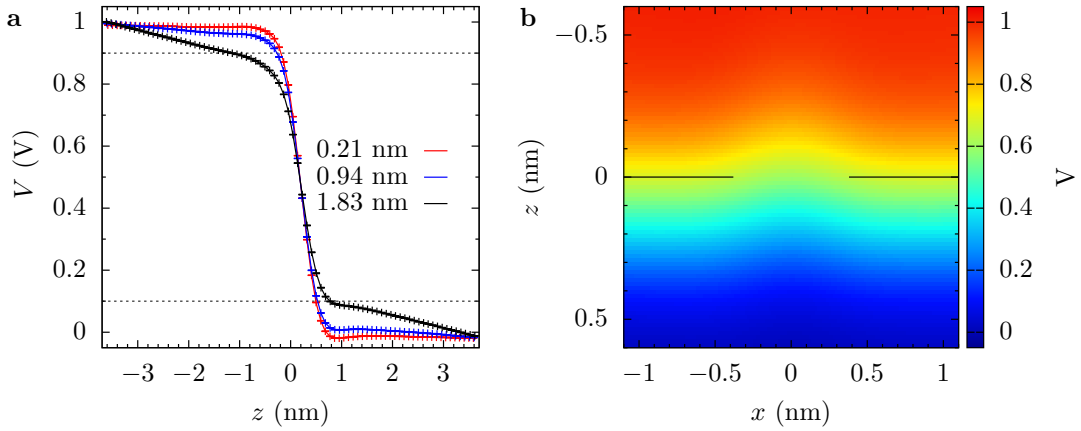

FIGURE 4.4: **Electric field** (a) Potential drop along the z-axis for various pore sizes and (b) a map of the potential for a pore of radius 0.21 nm. For larger pores, most of the potential drop (about 80% shown by the two dotted horizontal lines) occurs within a distance r_p from the center of pore. The electric field can thus be approximated by $E \approx 0.8\,V/2r_p$. However, for small pores the entire potential drop occurs over 1 nm due to vdW repulsion of the ions by the graphene membrane. In Fig. 4.5, we use the approximate electric field for larger pores in the expression $ez_\nu n_\nu \mu_\nu A_p E$ for the whole range of values reported. This overestimates the field for smaller pores, but will approach the right value as the pore size increases. Note, as well, that K^+ tends to come closer to the graphene membrane due to its smaller vdW repulsion. This results in the potential drop occurring mostly on the anion side and, when the voltage is increased enough to substantially polarize water, in the effective barrier for K^+ decreasing before that for Cl^-. Connecting lines are shown as a guide to the eye. The potential map were produced using the method described in [91].

4.3. Results

Atomically thin pores, such as graphene or MoS_2, display more intricate behavior – compared to long pores and channels – when reaching the scale of the hydration layers. Molecular dynamics (MD) simulations show that the ionic current through graphene pores (see the schematic in Fig. 4.1) exhibits nonlinear behavior as the pore radius, r_p, is reduced to the sub-nanometer scale. This nonlinear behavior is seen as a rapid drop in the ionic current, Fig. 4.5(a,b), and an excess noise in the current. At these length scales the pore edge begins to deform the hydration layers, increasing the energy barrier for ions to cross the pore.

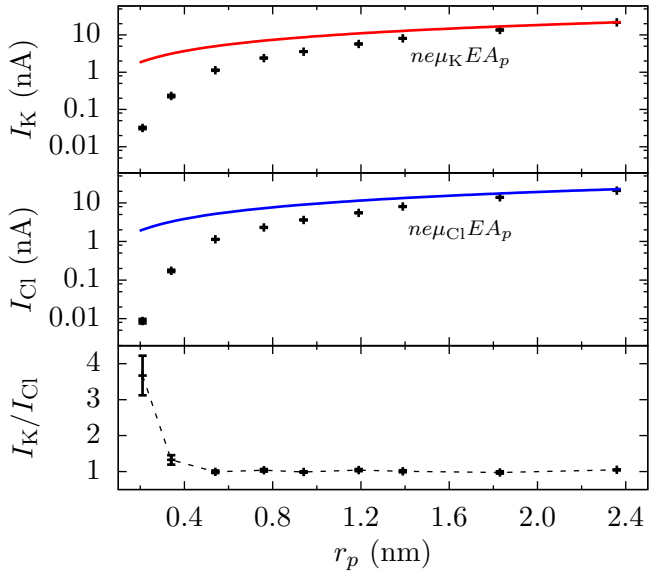

FIGURE 4.5: Selective behavior of graphene pores as a ratio of cation (I_K) to anion (I_{Cl}) currents versus the pore radius (as determined by MD simulations). For large pores ($r_p \gtrsim 2$ nm), the ionic current is due to bulk flow but limited by the pore's cross-sectional area, A_p, available for transport. In this situation, the contribution to the current from species ν is proportional to $ez_\nu n_\nu \mu_\nu$ (times A_p and the electric field, E, in the vicinity of the pore due to a 1 V applied bias, where z_ν is its valency, n_ν its number density, and μ_ν its mobility (shown as red and blue lines for K^+ and Cl^-, respectively). Thus, for potassium and chloride, the ratio is $I_K/I_{Cl} = \mu_K/\mu_{Cl} \approx 1$, as the relative mobility of K^+ to Cl^- is 1/1.04 . When the pore is very small, though, the relative cationic contribution to the total current increases. This is due to a higher dehydration energy of the anion compared to the cation. Connecting lines are shown as a guide to the eye. Error bars are ± 1 Block Standard Error (BSE) everywhere unless indicated otherwise.

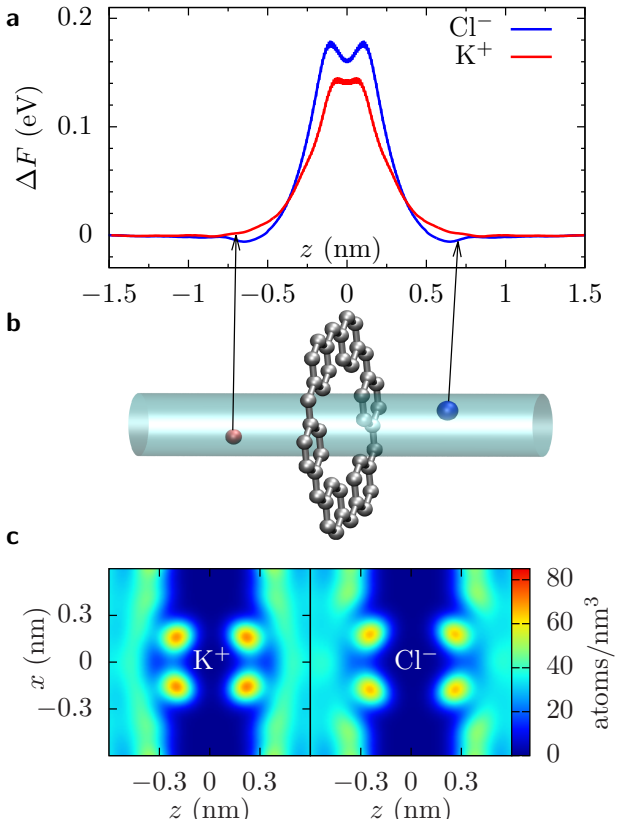

FIGURE 4.6: Free energy and hydration in graphene pores. (a) The free energy change of an ion to go from bulk into a pore with radius $r_p = 0.21$ nm versus the ions' z coordinate. (b) Schematic of the simulation showing the cylindrical region where a K^+ (red sphere) or a Cl^- (blue sphere) ion is confined for the ABF calculation. In the smallest pore and at 1 V, the relation $I_K/I_{Cl} = A_0 e^{(\Delta F_K - \Delta F_{Cl})/k_B T} \approx 3.5$, where $A_0 \approx 1$, k_B is Boltzmann's constant, and T is temperature, implies that the free energy change of Cl^- should be about 30 meV larger than that for K^+. This is consistent with the ABF calculation (between 20-40 meV depending on where we measure the difference). (c) Oxygen density from water around a potassium or a chloride ion fixed at the center of the $r_p = 0.21$ nm pore. Within the first hydration layer, there are $\langle n \rangle = 5.2$ and $\langle n \rangle = 5.8$ waters around K and Cl, respectively, which is approximately 1/4 less than in bulk in both cases. The loss of hydration is not as drastic as in long, thin solid-state pores. Also, the peaks in the oxygen density are further away for Cl^- compared to K^+, reflecting the electrostatic repulsion of the negative partial charge on oxygen by the anion. This larger distance affects the ability of anions to remain hydrated in the smallest pores – cations have a smaller effective size and thus have more opportunities to translocate without loosing hydration. Error bars in (a) are ±1 BSE.

In particular, graphene pores with $r_p = 0.21$ nm and in 1 mol/L KCl display selectivity of K^+ over Cl^- despite containing no charges or dipoles, as shown by the MD

simulations in Fig. 4.5(c). This observation is remarkable, since no electrostatic repulsion or specific interaction with the membrane is needed for its appearance. The selectivity and sharp rise in resistance was also seen for lower concentrations of KCl, i.e., this behavior is not due to ion-ion interactions or some other many-body effect.

To quantify the energetic differences of K^+ and Cl^-, we performed Adaptive Biasing Force (ABF) calculations for the smallest pore size. The ABF results, Fig. 4.6(a,b), demonstrate that – without an applied voltage – the K^+ is between 20-40 meV (depending on where we measure the difference) more favored to be in the pore compared to Cl^-, although both have to pay a substantial energy penalty. These equilibrium energy barriers are determined by the partial dehydration of the ions. When ions are in the atomically thick pore, water molecules can rearrange just outside of the pore to maintain significant hydration of the ion (see Fig. 4.6c). Ions only have to lose about 1/4 of their inner hydration water molecules in order to be at the pore center. In long, thin pores, a much larger dehydration occurs (about 3/4), as water molecules can only be at opposite ends of the ion (see Refs. [79, 80]). This will lead to related, but different, nonlinearities in the current.

The difference in energy barriers is due to a smaller dehydration energy of K^+ compare to Cl^-, which can be estimated from the relation,

$$\Delta E_\nu(r_p) = (1 - f_{1\nu}(r_p))E_{1\nu}, \tag{4.5}$$

where $f_{1\nu}$ is the fraction of water remaining in the 1st hydration layer and $E_{1\nu}$ is energy of the 1st hydration layer [79, 80]. This energy penalty is about 0.27 eV for K^+ and 0.37 eV for Cl^- when using $f_{1\nu} \approx 0.75$ (see Fig. 4.6(c)). Moreover, the fraction $f_{1\nu}$ can be approximated purely on geometric grounds: When an ion is in the center of the smallest pore, water molecules can not enter the pore due van der Waals (vdW) interactions with the carbon and the ion. The area available for water is composed of two spherical caps of radius $r_{1\nu}$ – the radius of the first hydration layer – on either side of the membrane. The fractional area left is $1 - d/2r_{1\nu}$ where d is the thickness of the membrane as seen by the water molecules near the pore edge. This thickness is $d \approx 0.2$ nm, slightly smaller than

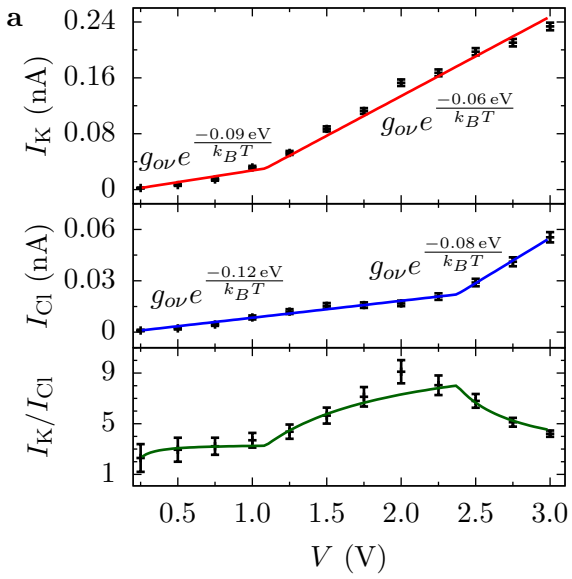

FIGURE 4.7: **Current & selectivity versus voltage.** Current-voltage characteristics for K^+ and Cl^- for the pore of radius 0.21 nm at 1 mol/L KCl (top panels). The selectivity of K^+ over Cl^- in the same pore (bottom panel). For small voltages, the ions display roughly linear behavior. Thus, we fit a piece-wise linear model for current taking each region to be linearly related to the differential conductance $g_\nu = ez_\nu n_\nu e^{(-\Delta F_\nu/k_BT)}\mu_\nu A_p/L = g_{0\nu}e^{(-\Delta F_\nu/k_BT)}$. Around 1.1 ± 0.1 V the energy barrier for potassium drops from (0.09 ± 0.004) eV to (0.06 ± 0.002) eV, whereas that of chloride drops from (0.12 ± 0.001) eV to (0.08 ± 0.008) eV around (2.38 ± 0.04) V. This change in conductance with voltage results in a rise and fall of selectivity. This piece-wise local conductance model (solid lines) can not capture all the features observable in the MD simulations (data points), but it captures the suppression of the current by the free energy barrier and how that barrier changes with voltage. Around 1.1 ± 0.1 V the energy barrier for potassium drops from $\approx 0.09 \pm 0.004$ eV to $\approx 0.06 \pm 0.002$ eV, whereas that of chloride remains approximately constant at $\approx 0.12 \pm 0.001$ eV. This results in sharper rise in the potassium current and, hence, selectivity. Error bars are ± 1 BSE.

the distance between water and the graphene membrane, as water molecules can move into the corrugated openings at the pore edge. This gives $f_{1\nu} \approx 0.7$ for both ions, when using $r_{1\nu} = 0.33$ and 0.31 nm for K^+ and Cl^-, respectively [80], in agreement with the full MD calculation.

The free-energy difference from the ABF calculation for each ion is about half of the value estimated using Eq. (4.5). To show why, we examine the net water dipole in the first layer when the ion is inside and outside the pore. The net dipole is reduced by about 5% to 10 %. Therefore, when about 25% of the water is lost, the remaining waters orient more strongly and the energy barrier is not 25% of the 1st hydration layer energy,

but less than half of that. The energy barrier is thus qualitatively in agreement with what Eq. (4.5) predicts but reduced due to stronger orientation of the remaining water dipoles (which is possible because interference from water-water interactions decreases). Finally, we note that other effects, such as polarization of graphene and different functional groups and/or pore shape (i.e., different atomic scale structure and graphene edge type), will change the observed barrier. However, when charges or static dipoles are absent, the main contribution to the free energy barrier is due to fractional dehydration – as qualitatively captured by Eq. (4.5). These barriers will differ from ion to ion, giving rise to weak selectivity (and, in some cases, giving rise to selectivity of anions over cations). This selectivity will thus appear in other atomically thin pores, such as MoS_2.

The selectivity also depends on the applied voltage, as seen in Fig. 4.7. The increasing selectivity from 0.25 V to 1 V is due to the lower barrier for K^+ vs. Cl^-. In this region, the current contribution from each ion species ν can be fit with the form,

$$I_\nu = g_\nu V + c_\nu, \tag{4.6}$$

where ,

$$g_\nu = e z_\nu n_\nu e^{(-\Delta F_\nu / k_B T)} \mu_\nu A_p / L, \tag{4.7}$$

and c_ν is a constant. This form of the current cannot capture all of the intricate behavior, but it does capture the main feature – the suppression of the current by the dehydration free energy barrier. The magnitude of c_ν reflects behavior below 0.25 V, which is a regime that is difficult to reach with all-atom simulations. Given c_ν, the differential conductance, Eq. (4.7), determines the selectivity as the voltage increases. This conductance depends on the valency, density, mobility, and free energy barrier of ion ν, as well as the electric field E and pore area A_p. Taking the electric field to be V/L with $L = 1$ nm (in agreement with the fields found from the MD simulations) and $A_p = \pi r_p^2$, the nonequilibrium free energy barriers are 0.09 ± 0.004 eV and 0.12 ± 0.001 eV for K^+ and Cl^-, respectively. These values are slightly less than the equilibrium free energy barriers from the ABF calculation in Fig. 4.6. As we discuss below, this is likely because of water polarization in the pore

that helps ions to move through. The value of other parameters, especially A_p and the voltage range, also affect the extracted free energy barriers both in equilibrium and out of equilibrium (computationally, for instance, sampling a smaller area in Fig. 4.6 (a,b) will lower the barrier, and fitting the IV curve at lower voltages will increase the barrier extracted). We note, though, that the difference in free energies between K^+ and Cl^- is the same in equilibrium and at low voltages.

Using the parameters for K^+ and Cl^- in Eq. (4.6), the selectivity will increase with voltage until it saturates at

$$\frac{I_{\mathrm{K}}}{I_{\mathrm{Cl}}} = \frac{g_{\mathrm{K}}}{g_{\mathrm{Cl}}}, \tag{4.8}$$

which fits very well with the selectivity data from MD, as shown in Fig. 4.7. However, we see that at ≈ 1 V, the selectivity starts to increase still further. Indeed, the differential conductance of K^+ increases at ≈ 1 V due to an effective lowering of the barrier to 0.06 ± 0.002 eV. This lower barrier is due to a polarization-induced chaperoning of the ion across the pore. As the local electric field increases with voltage, water becomes increasingly polarized in the vicinity of the pore and also increases its density there. When, for instance, K^+ sees a pore containing polarized water where the oxygen atoms are pointing towards the ion, it can more easily move to the pore edge and be taken through to the other side. The K^+ responds to this at lower voltages than Cl^- due to – surprisingly – its vdW interaction with carbon, which allows the charging layer of K^+ to be closer to the membrane than Cl^-.

4.3.1 Current behavior at the sub-nanoscale

The abnormal behavior of ionic current as the radius of the pore decreases to the sub-nanometer scale is seen in the sharp rise in the pore resistance and noise in the current, Fig. 4.8. As mentioned earlier, at these length scales, the pore edge begins to deform the hydration layers around the ions, which increases the energy barrier for ions to cross the pore.

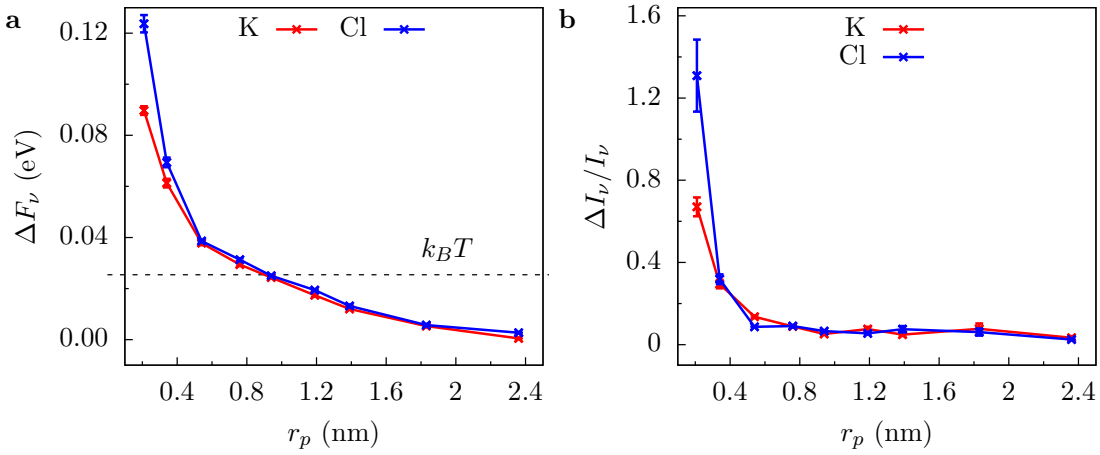

FIGURE 4.8: **Estimates of the free energy barrier and noise for various pores.** Sharp rise in (a) the free energy barrier and (b) the noise in the current at the sub-nanoscale. An "average" free energy barrier is estimated as $\Delta F_\nu = k_B T \log\left(\frac{q_\nu n A_p \mu_\nu E}{I_\nu}\right)$, where q_ν, μ_ν, n are the charge, average mobility (of K^+ and Cl^-), and particle concentration. The error in ΔF_ν is thus $k_B T \delta I_\nu / I_\nu$, where δI_ν is BSE in I_ν. The noise in current, $\Delta I_\nu(\tau)$ is measured by standard deviation of the mean current within blocks of length $\tau = 10$ ns. The relative noise in the current, $\Delta I_\nu(\tau)/I_\nu$ increases sharply due to the fluctuations in hydration layer configurations that allow or prohibit passage of ions through the pore [80]. The errors in ΔI_ν is estimated as $\frac{\Delta I_\nu}{\sqrt{2(N_b-1)}}$ [92]. Connecting lines are shown as a guide to the eye.

4.4. Selectivity

4.4.1 Experimental observation of selectivity

Ref. [1] found that graphene membranes with a distribution of pore sizes (in the sub-nanoscale) display selective behavior for K^+ over Cl^-. In that work, this is indicated by a nonzero membrane potential E_m. We use the relation

$$E_m = \frac{k_B T}{e} \ln\left(\frac{P_K [K]_o + P_{Cl} [Cl]_i}{P_K [K]_i + P_{Cl} [Cl]_o}\right) \tag{4.9}$$

or, rearranging,

$$e^{eE_m/k_B T} = \frac{\frac{P_K}{P_{Cl}} [K]_o + [Cl]_i}{\frac{P_K}{P_{Cl}} [K]_i + [Cl]_o} \tag{4.10}$$

to estimate the selectivity from the reported membrane potential ($E_m = 3.3 \pm 1$ mV, where we keep the second digit to not introduce rounding error, $[\mathrm{K}]_i = [\mathrm{Cl}]_i = 0.17$ mol/L, $[\mathrm{K}]_o = [\mathrm{Cl}]_o = 0.5$ mol/L , $T = 297$ K, and e is the magnitude of the electron charge). We obtain $\tilde{S} = P_{\mathrm{K}}/P_{\mathrm{Cl}} = 1.3 \pm 0.1$ as an "average" selectivity for their distribution of pore sizes. The ratio $P_{\mathrm{K}}/P_{\mathrm{Cl}}$ is the concentration-imbalance equivalent of $I_{\mathrm{K}}/I_{\mathrm{Cl}}$.

To compare with our numbers, we need to extract out the value for a particular pore size. For a membrane with a distribution of pore sizes, the observed selectivity $\tilde{S}$ can be estimated as

$$\tilde{S} = \frac{\sum_p I_{pK}}{\sum_p I_{pCl}} = \frac{\sum_p S_p I_{pCl}}{\sum_p I_{pCl}} \approx \frac{\sum_p S_p A_p}{\sum_p A_p}, \tag{4.11}$$

or,

$$\tilde{S} = \frac{\sum_p I_{pK}}{\sum_p I_{pCl}} = \frac{\sum_p I_{pK}}{\sum_p (1/S_p) I_{pK}} \approx \frac{\sum_p A_p}{\sum_p (1/S_p) A_p}, \tag{4.12}$$

where S_p (A_p) is the selectivity (area) for a pore of radius r_p. The approximate expressions in each equation assume that the current is proportional to area, but without a free energy barrier. This is a strong approximation and requires that the smallest pore sizes (i.e., with radii of about 0.15 nm and below) to be dropped from the sum (as their current contribution is negligible and not necessarily proportional to area). The sum is thus over the data in Table 4.2, which is from the selective membrane (5 min etch time) of Ref. [1]. This gives $S = 1.8 \pm 0.3$ from (4.11) and $S = 2.5 \pm 1$ from (4.12), where we again keep the second digit to not introduce rounding error. The difference in the selectivity estimated from the two equations is due to the fact that they did not take into account the free energy barrier at smaller radii. The error is calculated based on the error in $\tilde{S}$ only, as the error in area is not reported in Ref. [1]. However, the error due to area is expected to be much smaller than the approximations in the equations.

We note a few important limitations of this comparison between the experiments and our calculations. The lowest voltage in our simulations is still order of magnitude larger than the equivalent potential difference in the experiments. The regime below 0.25 V is very difficult to reach using all atom MD simulation for these pore sizes. Moreover, current experimental techniques cannot control the functionalization of graphene

A_p (nm^2)	0.2	0.123	0.108	0.321	0.368
r_p (nm)	0.25	0.20	0.19	0.32	0.34
S_p	S	S	S	1	1

TABLE 4.2: Current-carrying pores from the selectivity measurement of Ref. [1]. We assign a selectivity S for all pores with $r_p \approx 0.2$ nm and 1 for larger pores. There are also many pores with smaller radii, but we expect these pores to carry negligible current (and thus, even though they will be selective, they do not contribute to the observed selectivity). We do not include them in this table.

Salt (XCl)	CsCl	RbCl	KCl	NaCl	LiCl
σ (pS)	67	70	64	42	27
κ (10^{-3} S m^{-1})	1.42	1.42	1.3	1.19	0.95
E_{X} (eV)	3.1	3.4	3.7	4.6	5.7
μ_{bulk} (10^{-8} m^{2}V^{-1}s^{-1})	8.0	7.92	7.62	5.19	4.01
μ_{pore} (10^{-8} m^{2}V^{-1}s^{-1})	4.25	3.59	4.29	1.63	1.03
σ_{XCl} (pS)	67	66-63	65-67	55-52	50-48
σ_{X} (pS)	67	66-57	64-68	43-26	34-16

TABLE 4.3: Leakage conductance (σ), bulk conductivity of cations and anions together (κ), and hydration energy (E_{X}) of the cation X, as reported by Ref. [2]. Note that the reported bulk conductivity is four order of magnitude smaller than that used in their nanopore current measurements. We take the cation mobilities from bulk and effective mobilities in a biological pore from Ref. [93]. We make two estimates of the range of the conductance: One for σ_{XCl} (assuming both the cation and anion contribute) and the other for σ_{X} (assuming only the cation contributes). The first value in the range uses the bulk mobility and the second value uses the effective mobility. We note that even though graphene is atomically thick (and not the same pore used to calculate the effective mobility), it still can have, e.g., local water structure that reduces mobility. We use the effective mobilities of Ref. [93] only as an estimate. These ranges show that the deviation of the relative conductance from that predicted by bulk mobilities can easily be due to cation-only conductance (e.g., due to local charges) and/or effective mobilities through the defect channels responsible for the leakage conductance.

nanopores (and functionalization/surface species of graphene itself) which depends on the fabrication method and other random factors. Since it is not clear what groups will be present and where, we choose the simplest pore – the one with no functionalization. As well, some functionalization will introduce charges/dipoles to the pore region. However, if these are close (either on the pore rim or nearby), they will not give rise to the weak selectivity observed, but rather strong selectivity.

Garaj et al. [2] report that the leakage current (current through a graphene membrane when the pores have yet to be constructed) deviates from what the bulk conductivity would predict, which they attribute to the dehydration of the cations. Taking the conduc-

tance of CsCl to be the reference value, we can estimate the conductance of other salts XCl as

$$\sigma_{\mathrm{XCl}} = \frac{\sigma_{\mathrm{CsCl}}}{(\mu_{\mathrm{Cs}} + \mu_{\mathrm{Cl}})}(\mu_{\mathrm{X}} + \mu_{\mathrm{Cl}}). \tag{4.13}$$

As shown in Table 4.3, different *effective* mobilities of ions inside of pores explains some of the deviation. In fact, since the leakage conductance varies greatly from membrane to membrane (by a factor of two [2]), different effective mobilities alone may explain the deviation to within experimental uncertainties.

An alternative (or complementary) explanation is that the defect channels – the structure of which is unknown – are cation selective due to the presence of negative charges. In this case, the estimated conductance is

$$\sigma_{\mathrm{X}} = \frac{\sigma_{\mathrm{Cs}}}{\mu_{\mathrm{Cs}}}\mu_{\mathrm{X}}. \tag{4.14}$$

This estimate accurately explains the observations by itself. Relying on dehydration requires a convoluted explanation – or minuscule dehydration, e.g., a $1/100^{\mathrm{th}}$ fractional removal of water – to account for the differences between K^+, Na^+, and Li^+ when comparing to Cs^+. For instance, Na^+ and Li^+ have a much larger hydration energies than Cs^+, Rb^+, or K^+, and thus one expects that, if dehydration is a factor, the membrane conductance would go from cation and anion both contributing (for Cs^+, Rb^+, and K^+) to just anion contributing (for Na^+ and Li^+). In other words, NaCl and LiCl should have the same conductance, but they differ by 50 %.

We also note that ion transport for different cations was measured in Ref. [3], where the authors claim to have observed hydration-based selectivity. However, their selectivity can be explained based on difference in cation mobilities. Selectivity with respect to KCl can be captured via the normalized conductance

$$S_{\mathrm{XCl/KCl}} = \frac{\sigma_{\mathrm{XCl}}/(\mu_{\mathrm{X}} + \mu_{\mathrm{Cl}})}{\sigma_{\mathrm{KCl}}/(\mu_{\mathrm{K}} + \mu_{\mathrm{Cl}})}. \tag{4.15}$$

As shown in Table 4.4, the selectivity has a large range due to large variation of the

cation(X)	K^+	Li^+	Ba^{2+}	Ca^{2+}	Mg^{2+}
μ_X (10^{-8} $m^2V^{-1}s^{-1}$)	7.62	4.04	6.56	6.17	5.5
	device 3 ($r_p = 0.36 \pm 0.10$)				
σ (nS)	2.3 ± 1.2	1.1± 1.1	1.0±0.8	0.7± 0.5	0.4± 0.03
$S_{XCl/KCl}$	1	0.00 - 2.60	0.06 - 1.76	0.06 - 1.25	0.11 - 0.41
$S_{X/K}$	1	0.00 - 3.77	0.07 - 1.90	0.07 - 1.40	0.13 - 0.49
	device 4 ($r_p = 0.50 \pm 0.10$)				
σ (nS)	4.2 ± 0.3	2.2± 1.3	1.4 ±0	1.5±0.1	1.3± 0.1
$S_{XCl/KCl}$	1	0.25 - 1.17	0.34 - 0.40	0.34 - 0.45	0.31 - 0.39
$S_{X/K}$	1	0.37 - 1.69	0.37 - 0.43	0.38 - 0.51	0.37 - 0.46
	device 8 ($r_p = 0.39 \pm 0.06$)				
σ (nS)	2.6±1.5	1.3±0.1	2.3±1	2±1	1±1
$S_{XCl/KCl}$	1	0.39 - 1.65	0.32 - 3.22	0.28 - 3.01	0.00 - 2.00
$S_{X/K}$	1	0.57 - 2.40	0.35 - 3.48	0.31 - 3.37	0.00 - 2.39

TABLE 4.4: Chloride salt conductance (σ) of three different devices holding the chloride concentration constant at 100 mM [3]. The quantity $S_{XCl/KCl}$ is selectivity quantified by assuming both cation and anion contribute, Eq. 4.15, and $S_{X/K}$ by assuming only cations contribute, Eq. 4.16. The selectivity is shown as a range based on the error in σ (the actual range – the range of the data measured in Ref. [3] – is larger than shown here). Only bivalent ions in device 4 and Mg^{2+} in device 3 potentially show selective behavior. However, selectivity of this magnitude was observed in Ref. [87] for large pores, where dehydration can not be playing a role.

conductance. This makes it difficult to determine if there is any selectivity at all. Only the bivalent ions in device 4 and Mg^{2+} in device 3 have the entire range of $S_{\mathrm{XCl/KCl}}$ less than 1. Moreover, the experimental results seem to indicate the presence of negative charges near the pore (see Fig. 3d in Ref. [3]), which would mean that most of the current is carried by the cations. Thus, selectivity should be quantified as

$$S_{\mathrm{X/K}} = \frac{\sigma_{\mathrm{XCl}}/\mu_{\mathrm{X}}}{\sigma_{\mathrm{KCl}}/\mu_{\mathrm{K}}}. \tag{4.16}$$

This shows that (4.15) overestimates the deviation from non-selective behavior. Even if one ignores the large variation in the measured conductance in individual devices (and from device to device), the selectivity reported is consistent with the charge-based selectivity observed in Ref. [87]. Those latter results were in pores much bigger than hydrated ions, indicating that the selective behavior is likely due to differences how bivalent versus monovalent ions screen a charged membrane.

4.4.2 Dehydration and selectivity

Figure 4.9 shows the water density around the ion in the pore and the radial distribution function of oxygen, g_O. In our simulation, the number of oxygen atoms in first hydration layer around K^+ and Cl^- in bulk water are 7.4 and 6.8, respectively, and, when placed in the center of a $r_p = 0.21$ nm pore, 5.8 and 5.2. This is loss of about 1/4 of the water molecules from the innermost layer. Even though the fractional dehydration for K^+ and Cl^- are nearly equal the energy penalty is higher for Cl^- as its inner hydration layer is more strongly bound compare to K^+. As we increase the applied voltage, both ions were able to remain more hydrated while crossing the pore due to polarization-induced chaperoning of the ions. This results in a lower free energy barrier for transport, as seen from Fig. 4.10.

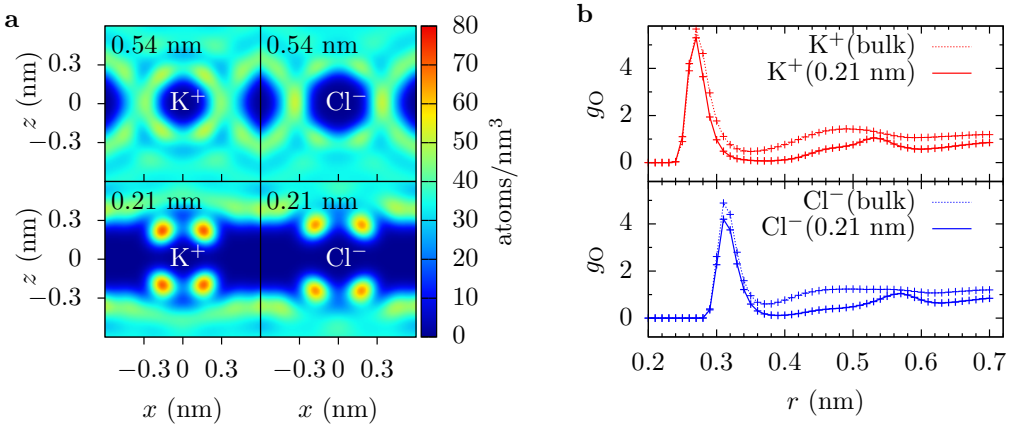

FIGURE 4.9: **Water density quantified by the oxygen density.** (a) The contour plots show either a potassium or a chloride ion fixed at the center of the pore. The pore radius is shown in the upper left corner of each panel. The hydration layers are visible as the high density region around the ion. As the pore size gets smaller, the hydration layers around the ion are distorted by the pore edge. The ions remain fairly well hydrated. (b) The radial distribution function of oxygen atoms around K^+ and Cl^- in bulk and at the center of a $r_p = 0.21$ nm pore for zero bias showing partial dehydration. The number of water molecules in first hydration layer of K^+ and Cl^- are 6.8 and 7.4 in bulk and 5.2 and 5.8 at the center of pore, respectively, i.e., a loss of about 1/4 of the water molecules from first hydration layer. Connecting lines are shown as a guide to the eye.

4.5. The effect of the ion concentration

In order to confirm that the anomalous behavior of current and weak selectivity is not due to a many-body effect but rather to single ion behavior, we repeat the selectivity calculations for lower concentrations of KCl. Both the anomalous behavior of current and weak selectivity are still present in concentrations as low as 0.1 mol/L, at which point there were only a few ions of each type in the smallest simulation box size (hence, box size errors start to become significant).

4.6. Discussion

There are thus two facets of selectivity: the mechanism and the nonlinear features with voltage. The former depends on the dehydration energy and the pore geometry, and

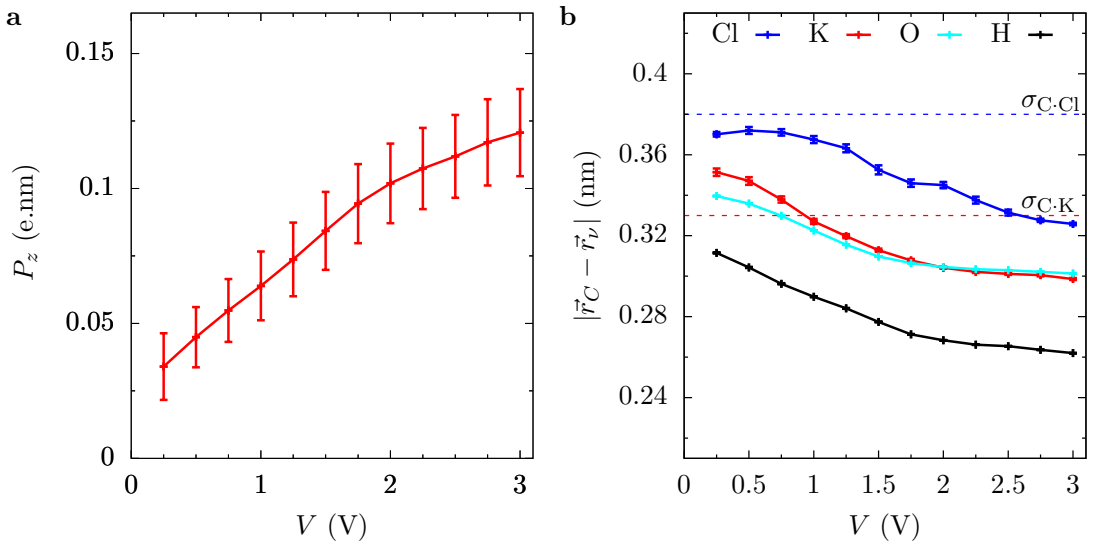

FIGURE 4.10: **Polarization induced chaperoning of ions.** (a) The z-component of polarization of water molecules in the pore region. With increased voltage water molecules are strongly polarized along the applied field. The polarized water molecule enable the ions approaching the pore to stay hydrated and hence assist them to cross the pore. (b) The distance ($|\vec{r}_C - \vec{r}_\nu|$) between an ion ν (or an oxygen/hydrogen from water) crossing the pore and the nearest carbon atom versus voltage. At higher voltage ions are able to enter the repulsive zone ($r < \sigma$) of vdW potential of carbon atom which effectively increases the area of transport. This is partly responsible for the increased current at higher voltages. However, the main cause of the latter is the chaperoning of ions across the pore by polarized water, which happens at lower voltage for K^+ compare to Cl^- due to the charge layer of the former being closer to the graphene membrane, see Fig. 4.4(a).

the latter depends on structural changes of water in the pore as the voltage increases (as well as vdW interactions). Since both are dependent only on geometry and ion characteristics in bulk water, these features will be present for other atomically thin pores and channels. This mechanism for nonlinearities and selectivity gives a simple predictions that can be tested experimentally by examining multilayer graphene, MoS_2 pores, or other pores.

Moreover, selectivity has recently been observed in graphene membranes [1, 87]. In Ref. [1], the selectivity is weak, giving an average ratio of translocation rates of about 1.3 ± 0.1 for potassium to chloride at zero applied bias but in the presence of a concentration gradient across the membrane. That alone may be due to effective mobilities, but, in this case, the pores' structures are known. This experiment has a distribution of pore sizes for

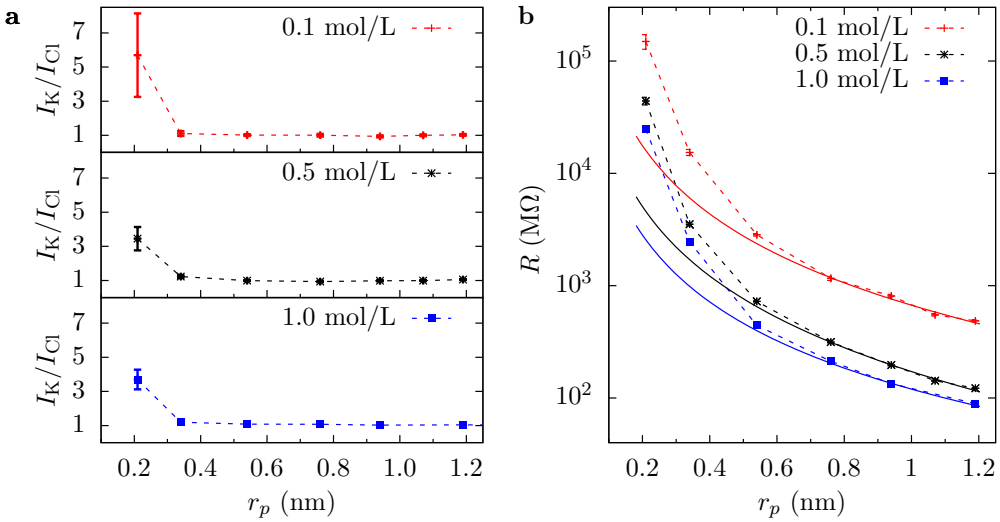

FIGURE 4.11: **Selectivity and pore resistance for three different concentrations.** (a) Selectivity and (b) pore resistance for 0.1 mol/L, 0.5 mol/L, and 1.0 mol/L KCl. The solid line is the fit of resistance of the form, $R = \frac{a}{r_p} + \frac{b}{r_p^2}$ [94, 10]. Here, the $1/r_p$ term is due to access resistance and the $1/r_p^2$ term is due to the pore resistance. Note that this deviation from normal behavior is quite large as the axis is on a logarithmic scale. The persistence of selectivity and the sharp rise in pore resistance at lower concentrations confirms that the behavior is not due to ion-ion interactions or some other many-body effect. Connecting lines are shown as a guide to the eye.

each membrane. Assuming the smallest pores make a negligible contribution to the current – and thus do not affect the average selectivity even though they are themselves selective – and the largest pores have no selectivity, the experimental observations yield a selectivity in the range ≈ 1.8 to 2.5 for a $r_p = 0.21$ nm pore. This is larger than potential variation due to effective mobilities and agrees well with the dehydration-induced selectivity of ≈ 2.3 that we find at low voltages. In Ref. [87] the selectivity is much higher (≈ 100), even for large pores (r_p in the 1 nm to 10 nm range, i.e., well above the size of hydration layers). In both experiments, though, the selectivity was attributed to the presence of charges on the graphene.

Our results indicate, however, that weak selectivity is the consequence of different dehydration energies and fractional removal of water (determined by the hydrated ion size and pore geometry) – i.e., not due to local charges or dipoles, which would result in the much higher selectivities observed in Ref. [87] and in biological pores. While

r_p (nm)	0.21	0.34	0.54	0.76	0.94	1.19	1.39	1.83	2.36
l (nm)	3.7	3.7	3.7	3.7	3.7	7.4	7.4	7.4	7.4
I_{K} (nA)	0.032	0.23	1.13	2.40	3.57	5.7	8.1	13.6	21.8
I_{Cl} (nA)	0.009	0.17	1.13	2.32	3.61	5.5	8.0	13.9	20.8
$I_{\mathrm{K}}/I_{\mathrm{Cl}}$	3.7	1.3	1.0	1.0	1.0	1.0	1.0	1.0	1.0

TABLE 4.5: **Current for various radii.** The table shows the current for 1.0 mol/L KCl solution for the box of height $h = 6.9$ nm for various radii. The edge of the box is $l = b = 7.4$ nm for larger pores ($r_p > 1$ nm) and $l = b = 3.7$ nm for smaller pores. The latter allows for much longer simulations, which are needed to achieve convergence. The error in the current is shown in Fig. 4.5. The Block Standard Error determines the number of significant digits in this and the following tables.

V (V)	0.25	0.5	0.75	1.0	1.25	1.5	1.75	2.0	2.25	2.5	2.75	3.0
I_{K} (pA)	2.3	7.0	15	32	52	87	113	153	167	197	210	234
I_{Cl} (pA)	1.0	2.2	4.5	9	12	15	16	17	21	29	41	55
$I_{\mathrm{K}}/I_{\mathrm{Cl}}$	2.3	3.0	3.2	3.7	4.4	5.6	7.1	9.1	8.0	6.8	5.1	4.2

TABLE 4.6: **Current for various voltages.** The table shows the current for 1.0 mol/L KCl solution through the smallest pore $r_p = 0.21$ nm for various voltages. For these calculations, we use the box height $h = 6.9$ nm and the smaller cross section, $l = b = 3.7$ nm. The error in the current is shown in Fig. 4.10

charges/dipoles can not be ruled out as an explanation for the results of Ref. [1], they would need to be far from the pore, or only present in a minority of pores in order to generate weak selectivity. This would leave unexplained why a small increase in pore radius eliminates selectivity. Screening can play a role here, suggesting that changing the molarity of the solution – thereby changing when selectivity disappears as the pore radius increases – is a simple test to determine the presence of local charges/dipoles. The other effects we predict – nonlinear features in the current-voltage characteristics and enhanced selectivity – should

	pore		bulk	
	$\langle p_r \rangle$ (D)	$\langle n \rangle$	$\langle p_r \rangle$ (D)	$\langle n \rangle$
K^+	2.02	5.2	1.60	6.8
Cl^-	1.81	5.8	1.54	7.4

TABLE 4.7: **Dipole orientation.** The average radial component of individual water dipole $\langle p_r \rangle$ and average number of water dipoles $\langle n \rangle$ in the first hydration layer of K^+ an Cl^- ions in the smallest pore ($r_p = 0.21$ nm) and in the bulk. The dipole moment of water in our model is 2.35 in units of Debye (0.021 e nm). The dipoles are strongly oriented in the pore compare to bulk but have fewer dipoles and hence there is a decrease in total dipole moment.

Atoms (X)	K	Cl	H	O	C
ϵ_X (meV)	3.773	6.505	1.89	6.596	3.036
r_X (nm)	0.176	0.227	0.022	0.177	0.199

TABLE 4.8: **Lennard-Jones parameters for individual elements.** The vdW potential between two atoms at a distance d, is calculated using the Lennard-Jones relation, $V_{\mathrm{LJ}} = \epsilon_m \left[\left(\frac{r_m}{d}\right)^{12} - 2\left(\frac{r_m}{d}\right)^{6} \right]$, where the parameter $r_m = r_1 + r_2$ is the equilibrium distance and $\epsilon_m = \sqrt{\epsilon_1 \epsilon_2}$ is the well depth of the interaction.

be observable experimentally. These results elucidate selectivity and dehydration effects in transport when going from the nanoscale [2, 11, 10, 95, 96] to sub-nanoscale channels and pores. It should help design and understand the behavior of solid-state pores that serve as hosts for other nanoscale probes, i.e., localizing and interrogating molecules or nanoscale structures, such as DNA sequencing with ionic [19, 97, 98, 99, 100, 101, 102, 103, 101] or transverse electronic currents [104, 105, 106, 107, 108, 109, 110].

Moreover, selectivity in biological ion channels is complex and due to many competing interactions and processes. Indeed, dehydration is so important in tiny biological ion channels that it is only the presence of charges, dipoles, and protein structure/dynamics that allows ions to pass by counteracting dehydration. Indeed, selectivity occurs because the pore interacts with ions in an ion-dependent manner, e.g., due to the atomic configuration in the protein's selectivity filter [72]. Our work, however, demonstrates for the first time that graphene pores will allow one to measure selectivity due to dehydration only, therefore delineating its contribution in more complex biological systems. This will allow one to characterize ion transport behavior in confined geometries without the effect of protein structure, surface charges, etc. This will likely lead to the development of experimental model systems to mimic and understand biological channels.

Finally, one of the core challenges with the use of solid state membranes for filtration and other applications is to engineer selectivity. Site-specific chemical functionalization of, e.g., graphene, is currently not possible. Our results suggest that the geometry, which is significantly more controllable, can be designed to give selectivity that is not currently possible in solid state systems via the use of charges or dipoles. Moreover, these results

will shed light on the role of the electrostatic environment and functionalization introduced by the fabrication process, as well as other conditions such as pH. Together with a characterization of pore functionalization, solid-state pores will thus allow – for the first time – to experimentally delineate the contributions to transport in more complex biological pores and for the optimization of porous structures for applications.

5. IONIC SELECTIVITY AND FILTRATION FROM FRAGMENTED DEHYDRATION IN MULTILAYER GRAPHENE NANOPORES

Selective ion transport is a hallmark of biological ion channel behavior but is a major challenge to engineer into artificial membranes. Here, we demonstrate, with all-atom molecular dynamics simulation, that bare graphene nanopores yield measurable ion selectivity that varies over one to two orders of magnitude simply by changing the pore radius and number of graphene layers. Monolayer graphene does not display dehydration-induced selectivity until the pore radius is small enough to exclude the first hydration layer from inside the pore. Bi- and tri-layer graphene, though, display such selectivity already for a pore size that barely encroaches on the first hydration layer, which is due to the more significant water loss from the second hydration layer. Measurement of selectivity and activation barriers from both first and second hydration layer barriers will help elucidate the behavior of biological ion channels. Moreover, the energy barriers responsible for selectivity – while small on the scale of hydration energies – are already relatively large, i.e. several k_BT. For separation of ions from water, therefore, one can exchange longer, larger radius pores for shorter, smaller radius pores, giving a practical method for maintaining exclusion efficiency while enhancing other properties (e.g., water throughput). This work was published in [111].

5.1. Introduction

Ion transport is vital to physiological processes in the cell [112, 6, 75], where membrane ion channels control ion motion through the interplay of protein structural transitions, precisely placed dipoles and charges, and dehydration. Nanotechnologies seek to mimic and exploit the same physical mechanisms for membrane filtration and desalination. However, biological systems are complex and make use of sophisticated assembly methods, ones that we are still not able to utilize in artificial devices. Recent work on

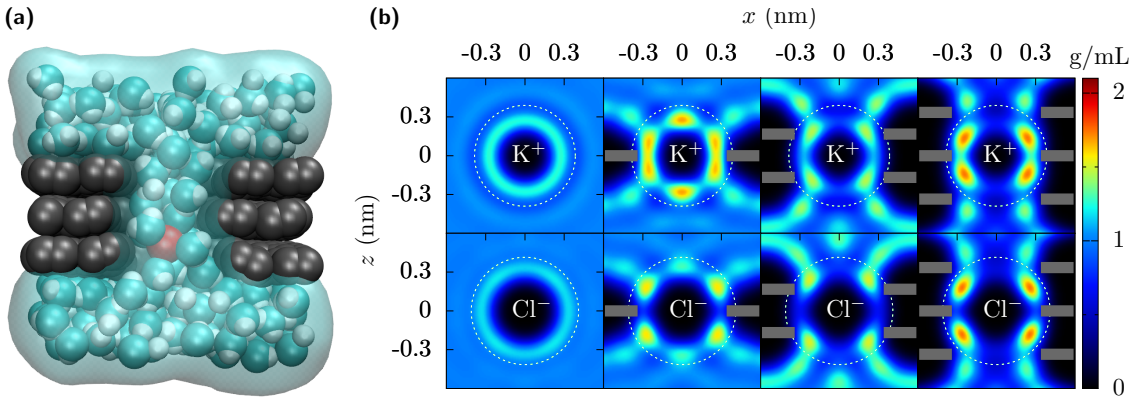

FIGURE 5.1: **Dehydration of ions going through multilayer graphene pores.** **(a)** A nanopore through trilayer graphene. As K^+ (red) translocates through the pore, it retains only part of its hydration. In this case, the pore radius is $r_p = 0.34$ nm and the first hydration layer is essentially complete. The second hydration layer, though, is significantly diminished due to the carbon of the graphene (grey) preventing the water molecules (cyan and white) from fluctuating about 0.5 nm away from the ion, except along the pore axis. **(b)** Water density quantified by its oxygen location around K^+ and Cl^- ions in bulk and mono-, bi-, and tri-layer graphene (shown as grey bars) pores with radius $r_p = 0.34$ nm. The white dotted circles demarcate the first and the second hydration layers. The first hydration layers remain but acquire some additional structure. The second hydration layer is greatly reduced (see Fig. 5.2 and Table 5.2). For this pore size, the free energy barrier due to the second layer dehydration significantly contributes to the ion currents and selectivity.

two-dimensional channels in graphene laminates demonstrates ion selectivity [113] by constraining the channel height. However, one-dimensional channels – pores – give additional control over the confining geometry, where, for instance, recent theoretical results [70] show that experiments on sub-nanoscale, monolayer graphene pores display dehydration-only selectivity [1]. Using all-atom molecular dynamics (MD) and theoretical arguments, we will show that the most fundamental of all processes – dehydration of ions – can be reliably tuned in bare graphene nanopores by controlling only the pore radius and number of graphene layers. This gives rise to selectivity across one to two orders of magnitude before ion currents drop to unmeasurable levels.

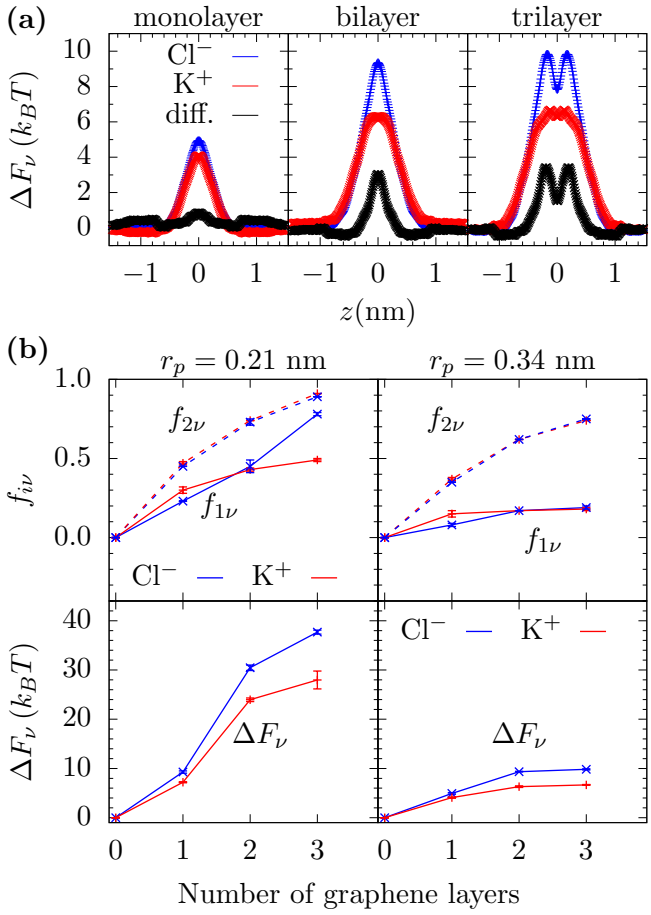

FIGURE 5.2: **Free energy barriers and dehydration. (a)** Free energy barrier versus K^+ and Cl^- location, z, on the pore axis as they cross mono-, bi-, and tri-layer graphene pores with radius 0.34 nm. As the number of layers increases, the energy barrier becomes more substantial and a difference between the two ion types appears. **(b)** Fractional dehydration in the first and second layer ($f_{1\nu}$ and $f_{2\nu}$) for K^+ and Cl^-, where the ion is at the position of its free energy maximum in the pore. When the pore radius is less than the first hydration layer radius (about 0.3 nm), then both the first and second hydration layers lose a substantial amount of their water molecules (upper left panel). However, with just a slightly larger pore radius, $r_p = 0.34$ nm, the first hydration layer retains most of its water but the second layer still loses a significant number of water molecules (upper right panel). The free energy barriers (lower panels) will increase with the number of graphene layers, as a "short pore" interferes less with the hydration than the longer pores. However, while dehydration is the mechanism by which selectivity occurs, water loss is not the sole predictor of selectivity. As Eq. 5.1 shows, one also needs the hydration layer energies. The Cl^- ion has a larger hydration energy and, thus, even for the same $f_{i\nu}$, Cl^- will be selected against. Error bars are ± 1 standard error from five parallel simulations.

5.2. Results

This range of achievable selectivities is possible due to the ability to separately control the pore radius and length at the nanoscale, i.e., in the regime that influences the

hydration layer properties via the confinement. Fig 5.1 shows how the hydration layers change for mono- to tri-layer graphene pores. As an ion goes from bulk into the pore, it can not bring its whole hydration layer with it, but rather some of the water molecules are blocked from entering the pore. The shedding of some of the hydration gives a free energy barrier, a simple estimate of which is

$$\Delta F_\nu = \sum_i f_{i\nu} E_{i\nu}, \tag{5.1}$$

where $f_{i\nu}$ ($E_{i\nu}$) is the fractional dehydration (energy) in the i^{th} hydration layer [79, 80]. The fractional dehydration depends on the confinement via the pore radius and length (number of graphene layers), as this reduces the volume available for water to hydrate the ion. That is,

$$f_{i\nu} = \frac{\Delta n_i}{n_i} \approx \frac{\Delta V_i}{V_i}, \tag{5.2}$$

with the total hydration number n_i, and volume V_i, of a i^{th} hydration layer in the bulk and the reduction of the respective quantities ΔV_i and Δn_i in the pore. The quantity ΔV_i comes from pure geometric arguments – it is the volume excluded by the presence of carbon atoms in the graphene – and the approximation in Eq. 5.2 agrees well with the loss of water molecules computed from MD simulations (shown in Fig. 5.1b).

For the radius $r_p = 0.34$ nm pore in Fig. 5.1a, this simple analytic estimate predicts that there should be a small amount of dehydration in the first layer, increasing when going from mono- to bi-/tri-layer graphene. But for the multilayer graphene, second hydration layer is significantly reduced. However, due to the much larger hydration energy of the first layer [80], both hydration layers influence the magnitude of the ion currents and thus the selectivity. Moreover, the contribution to the dehydration free energy barrier from hydration layer i will "level off" when the length is greater than about twice its radius, i.e., when part of the hydration layer can no longer reside outside of the pore.

This is exactly what is seen from free energy computations using MD simulations. Fig. 5.2a shows the free energy barrier for K^+ and Cl^- moving through the pore. Mono-layer graphene interferes very little with the hydration. To the extent that this membrane

dehydrates the ions, the remaining water molecule can partially compensate for this effect by more strongly orienting their dipole moment with the ion. When the number of layers increases, however, the energy barriers change in size and shape. For both bi- and tri-layer graphene, the dehydration is more substantial and, when accounting for the larger Cl^- hydration energy, it starts to differentiate between the two ions. That is, the relative barriers are predominantly influenced by the hydration energies of the different ions. As the confinement increases – decreasing the pore radius and increasing the pore length – more water will be lost from the hydration layers and ions with larger hydration energies will be more effectively filtered by the pore and selected against. Fig. 5.2b shows this effect, i.e., how the dehydration and free energy barriers increase with increasing number of graphene layers.

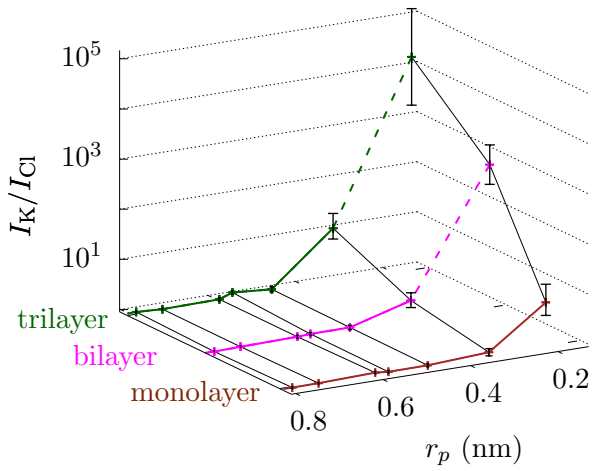

FIGURE 5.3: **Selectivity of graphene pores.** The selectivity, I_K/I_{Cl}, is at an applied bias of 1 V, although the permeation rates should follow similar trends. Selectivity increases as pore radius decreases and when the the number of layers increases. Trilayer graphene with $r_p = 0.34$ nm gives a similar selectivity as monolayer graphene with $r_p = 0.21$ nm. Moreover, if only ion filtration is of interest, then these two pore sizes can be exchanged. For bi- and tri-layer graphene, we use Eq. 5.6 for $r_p = 0.21$ nm, as the currents are too small to reliably determine computationally. Those points have a dashed line connecting them to the remaining plot. The error bars are ± 1 Block Standard Error (BSE).

Free energy barriers and ionic currents

The free energy barriers are the primary factor in determining permeation rates and ion currents. For instance, the current in the pore is related to the free energy barrier and electric field E according to [80]

$$I_\nu = e z_\nu \mu_{\text{eff}} E A_p n_\nu e^{-\Delta F_\nu / k_B T}, \tag{5.3}$$

where e is the electric charge, z the ion valency, μ_{eff} the effective mobility in the pore, A_p is the area of the pore and n_ν the bulk ion density.

The effective pore resistivity is

$$\rho_{\text{eff}} = \frac{E A_p}{I_\nu} = \frac{e^{\Delta F_\nu / k_B T}}{e z_\nu \mu_{\text{eff}} n_\nu} = \rho_\nu \frac{\mu_\nu}{\mu_{\text{eff}}} e^{\Delta F_\nu / k_B T}, \tag{5.4}$$

which gives

$$\ln \frac{\rho_{\text{eff}}/\rho_\nu}{\mu_\nu/\mu_{\text{eff}}} = \Delta F_\nu / k_B T. \tag{5.5}$$

Here, ρ_ν (μ_ν) are the bulk resistivity (mobility). As shown in Fig 5.6(b), the logarithm of the effective resistivity correlates well with the free energy barrier in the pore, suggesting that any consequence of effective mobilities can be neglected to first approximation.

Selectivity

For atomically thin graphene membranes, one expects that the effective mobility is ill-defined. Even still, the results given in the Fig. 5.6 show that the change in effective mobility of ions in the pore can be ignored to first approximation, giving selectivity as

$$\frac{I_{\text{K}}}{I_{\text{Cl}}} \approx e^{(\Delta F_{\text{K}} - \Delta F_{\text{Cl}})/k_B T}. \tag{5.6}$$

This is, however, only an estimate: The energy landscape has some ion-dependent spatial structure (which introduces additional factors into the current) and it changes when a bias is applied. For instance, the applied field orients the water dipoles, which can subsequently

assist ions in crossing the pore [70].

Using nonequilibrium MD, we directly compute $I_{\mathrm{K}}/I_{\mathrm{Cl}}$ where possible and use Eq. 5.6 otherwise. Fig. 5.3 shows the selectivity for pores of radii ranging from 0.21 nm to 1.4 nm in mono-, bi-, and tri-layer graphene. Just as the above theoretical arguments and free energy simulations indicate, the relative current of K^+ increases compared to Cl^- as the pore radius approaches the hydration. The magnitude of this selectivity depends on the pore radius as well as the number of graphene layers. This provides a method to control selectivity beyond just changing the pore radius. We note that the pores are electrically neutral and mobility of both K^+ and Cl^- ions are nearly equal. Hence, the selectivity is due to differences in their hydration energies of the ions. All ion types will thus display mutual selectivity. We also note that chemical functionalization of the pore and of the graphene can modify energy barriers, especially when, e.g., the chemical groups are strongly polar or charged under some ionic conditions. When this occurs, the sign of the charge matters, and anions, for instance, may be excluded from the pore. However, the effect we discuss will never-the-less be present between cations, where Eqs. 5.1 and 5.2 can estimate the selectivity.

The selectivity that is measurable experimentally will be limited by the the minimum resolvable current. The Cl^- current is about 5 pA for the 0.34 nm tri-layer pore (see Table 5.1). However, currents as low as 1 pA are measurable in experiments [114], thus a several fold change in selectivity should be detectable as the pore size and length vary. According to Ref. [115], the water flow rate only decreases by about 20% when going from mono- to bi- layer graphene when the pore size is kept constant and there is no additional inter-layer spacing. Increasing the number of layers to increase selectivity (or ion exclusion overall) will not significantly reduce water flow for applications such as desalination. Moreover, for a given selectivity or ion exclusion, one can use a larger pore with more layers, increasing the overall water throughput (as the area available for transport is larger).

These results indicate that to achieve a given selectivity, one can exchange a $r_p = 0.21$ nm monolayer pore with a tri-layer pore of a larger radius ($r_p = 0.34$ nm). These pore sizes are both clearly small, but this indicates that, *when dealing with nanostructures*, there

is flexibility on how to create the desired ion exclusion. Pore sizes are easily controllable with individual pores fabricated with transmission electron microscopes [2, 10, 11] and techniques are under development to fabricate large scale membranes with precise control [1, 3]. Moreover, we examine only pores with high symmetry. Varying the pore aspect ratio can further tune ion selectivity and conductance.

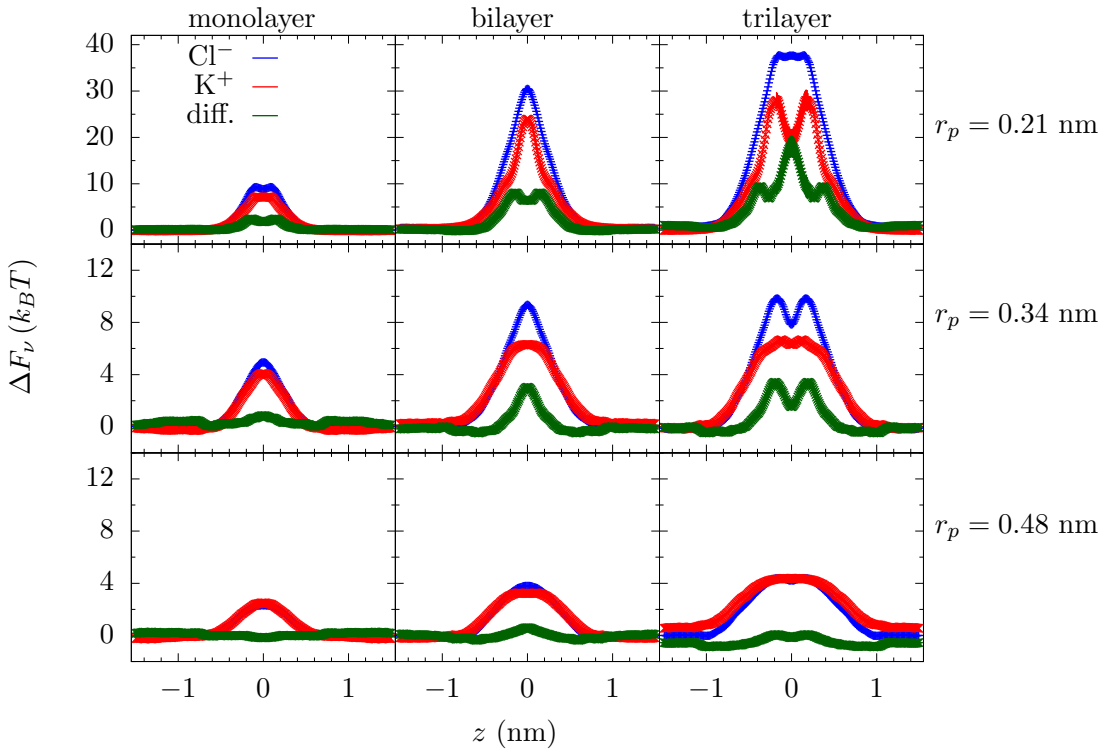

FIGURE 5.4: Free energy barrier for K^+ (red line) ion, Cl^- (blue line) ion, and their difference (green line) to translocate along the z-axis through pores of radius 0.21 nm, 0.34 nm and 0.48 nm in monolayer, bilayer and trilayer graphene. The free energy barriers, as well as their difference, increase with decreasing pore radius and with increasing number of graphene layers, thus making the pore more selective. Error bars are ±1 standard error from five parallel simulations.

"Quantized" ionic current

Since ionic current density is related to free energy barrier as $J_\nu = J_{\nu 0} e^{-\Delta F_\nu}$ and the energy barrier is related to the number of water losts from the solvation shell, the ionic current is expected to have a step-like feature with respect to the pore size as it determines the extent of dehydration. We see such step-like features in current density, as shown in

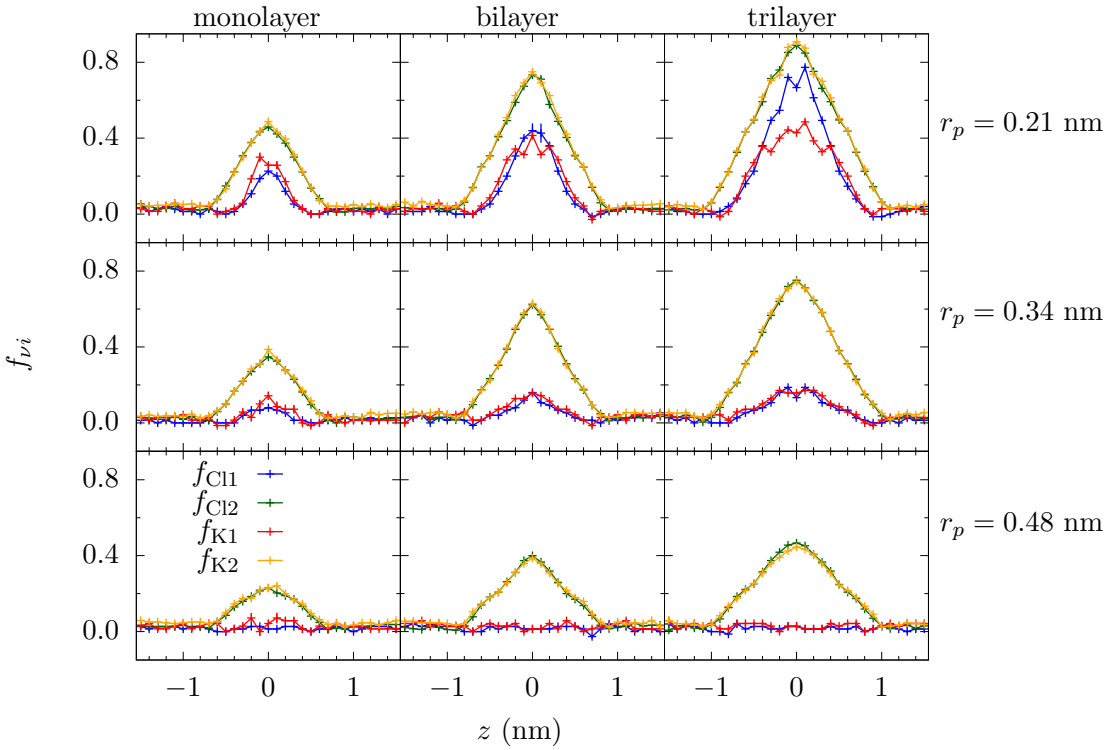

FIGURE 5.5: Fractional dehydration in the first and the second hydration layers for K^+ and Cl^- ions translocating through pores of radius 0.21 nm, 0.34nm and 0.48 nm in monolayer, bilayer and trilayer graphene. Just like the free energy barrier, the dehydration increases with the decrease in the pore radius and with the increase in the number of graphene layers. Fractional dehydration is always smaller in the first hydration layer compare to the second hydration layer. However, due to the larger energy of the first hydration layer, it can have a larger contribution to the free energy barrier. Error bars are ± 1 standard error from five parallel simulations.

Fig. 5.6(b). However, the pore sizes themselves are "discretized" at this length scale (and not perfectly circular), it is hard to determine if these features are sharp. Irregularly shaped nanopores may allow one to examine intermediate pore sizes and determine if these step features are indeed sharp. We leave this to a future study, although it is clear from Fig. 5.6(a) that there is a change in current density when the second (for bi- and tri-layer graphene) and first hydration layers (for all cases) are encroached upon.

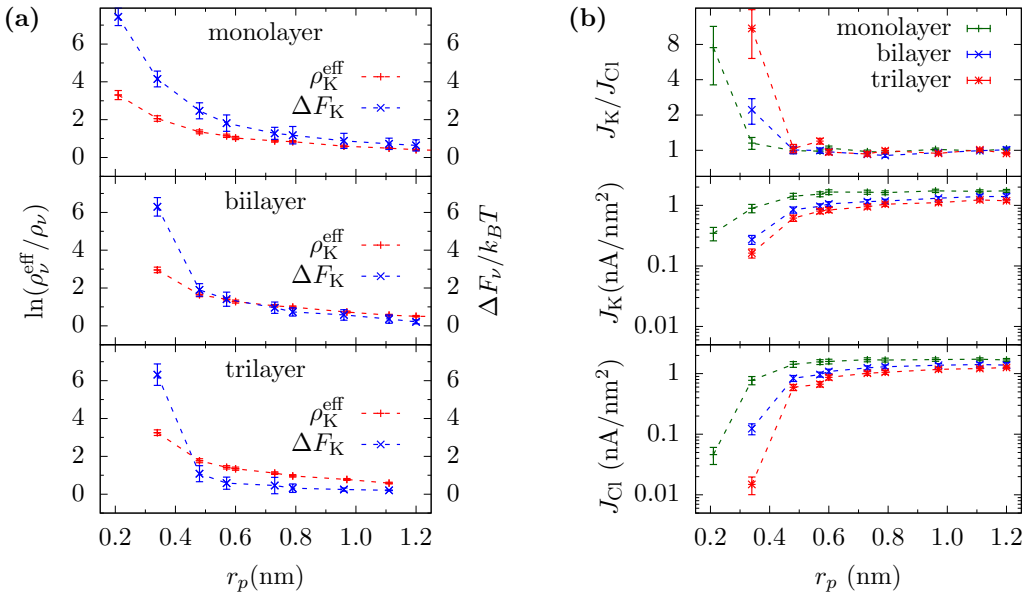

FIGURE 5.6: **(a) ρ_{eff} and ΔF (at its maximum) for K^+ versus r_p in mono-, bi- and tri- layer graphene. In each case, $\ln[\rho_{\text{eff}}]$ correlates with the maximum free energy barrier. (b)** Current densities in the pore, $J_K = I_K/\pi r_p^2$ and $J_{Cl} = I_{Cl}/\pi r_p^2$, and their ratio versus r_p for mono-, bi- and tri- layer graphene membranes. There is no selectivity ($I_K/I_{Cl} \approx 1$) until both the length and radius of the channel significantly encroach on the hydration layers. This occurs for a larger radius for bi- and tri- layer graphene as both the first and second hydration layer are more significantly diminished due to the larger pore length. Moreover, J is fairly constant for r_p greater than the second hydration layer radius (≈ 0.6 nm) and starts to drop as pore size decreases further. The drop is much sharper below the first hydration layer (≈ 0.3 nm) to the extent that it completely vanishes for bi- and tri- layer graphene. The error bars are $\pm$ 1 Block Standard Error (BSE)

5.3. Discussion

Ion transport through sub-nanometer channels, where dehydration is inevitable, is a key process in biology. Ion transport at this scale is also increasingly important in applications, such as nanopore sequencing (both ionic [19, 116, 95] and electronic [104, 105, 107]), desalination [117] and filtration [118]. Graphene membranes and laminates, as well as other atomically thick membranes, are playing a central role, where selective ion transport and ion exclusion is desired [1, 87, 70, 119, 120, 81, 113]. Moreover, fundamental studies demonstrate the possibilities of seeing ionic analogs of electric phenomena, such as quantized ionic conductance [79, 80] and ionic Coulomb blockade [108, 121]. Examining

pores with intermediate pore radii (but "non-circular") may show that there is a notion of *quantized ionic selectivity*, that for, e.g., trilayer graphene, as the pore radius is reduced, the second hydration layer first gives raise to selectivity, and then the first layer.

Our results form the basis for engineering and understanding selectivity and exclusion with multilayer graphene pores, where both the radial and longitudinal lengths can be controlled at the sub-nanoscale level. This is a feat not easily achievable with other approaches, i.e., solid state [79, 80] or carbon nanotubes [83, 84, 85] are not ideal for tuning dehydration-based selectivity, despite some success in making ultra-thin solid state pores[122]. Channel/pore geometry gives a range of possibilities for designing selective pores, on top of which chemical functionalization [82] and other factors can be used to modify their behavior.

5.4. Methods

5.4.1 All-atom MD simulations

We use multilayer graphene with AB stacking with a C-C bond length of ≈ 0.14 nm and inter-layer distance of ≈ 0.335 nm. We open a pore of nominal radius r_n at the center of each membrane by removing carbon atoms whose coordinates satisfy the condition $(x - x_c)^2 + (y - y_c)^2 < r_n^2$, where (x_c, y_c) is the center of mass in each graphene membrane. However, the pore radius, r_p, is measured from the inner edge of carbon atoms (taking the inner edge to be their vdW radius) around the pore. The graphene membrane has a square cross-section of 7.2 nm by 7.2 nm, which we immerse in an aqueous KCl solution of concentration 1 mol/L that extends 5 nm on both sides of the membrane.

We perform all-atom molecular dynamics (MD) simulations using NAMD2 [88] with a time step of 2 fs and employ periodic boundary condition in all directions. The water model in our simulation is rigid TIP3p from the CHARMM force field. Non-bonded interactions (van der Waals and electrostatic) have a cutoff of 1.2 nm but, we perform a full electrostatics calculation every 8 fs using particle-mesh Ewald (PME) method [26]. We

prepare the system using VMD[123] and then equilibrate the system using NAMD2. The equilibration steps are (1) minimizing the energy of the system for 4000 steps, (2) heating it to 295 K in another 8 ps, (3) a 1 ns NPT (constant number of particles, pressure and temperature) equilibration using the Nose-Hoover Langevin piston method[89] to raise the pressure to 101325 Pa (i.e., 1 atm), and (4) a 3 ns of NVT (constant number of particles, volume and temperature) equilibration.

We use real-time, all-atom molecular dynamics simulations to calculate the ionic current through the equilibrated system by applying an electric field perpendicular to the plane of the membrane. We set the Langevin damping rate to 0.2/ps for carbon and water (via its oxygen atoms) during these runs. We freeze the carbon atoms at the outer edge of the graphene membrane, but the rest of the carbon atoms in the graphene membrane are only confined by C-C bonds.

5.4.2 Solvation Shells

To calculate the solvation shells for each ion, we fix the ion in the center of a pore and run equilibrium NVT simulations. Fig. 5.7 shows the solvation shell around K^+ and Cl^- ions fixed at the center of 0.21 nm pore on mono-, bi- and tri- layer graphene. A similar plot for 0.34 nm pore is shown in Fig. 5.1b. In monolayer graphene, the ion at the center of the pore can maintain most of its first hydration shell. However, in bi- and tri-layer graphene there is a greater loss of water from first hydration layer. The dehydration is even stronger in the second hydration layer, loosing about 50%, 80%, and 90% of water molecules in mono-, bi-, and tri- layer graphene, respectively. The water molecules around the ion in the pore are spatially localized, thus giving fragmented solvation shells.

5.4.3 Free Energy Calculations

We calculate the free energy profile of an ion crossing the pore by using the Adaptive Biasing Force (ABF) method [30, 31] as implemented in NAMD2. We compute the free energy barrier within a cylinder of radius r_p and height of 3 nm centered at the origin. fig. 5.4 shows the free-energy profile for both K^+ and Cl^- ions and the difference in the free energies of these two ions along the z-axis. The free energy barrier for each ion

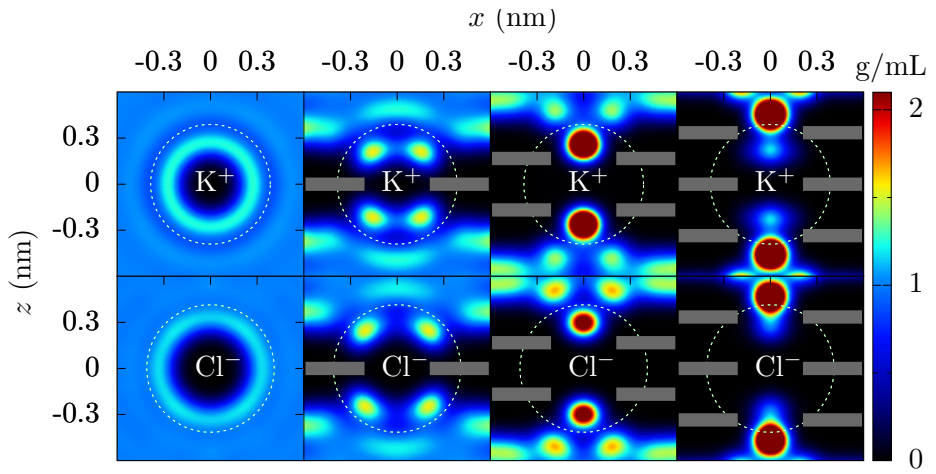

FIGURE 5.7: Water density (within the $y = 0$ plane) quantified by its oxygen location around K^+ and Cl^- ions in bulk and mono-, bi-, and tri-layer graphene (shown as grey bars) pores with radius $r_p = 0.21$ nm. The white dotted circles demarcate the first and the second hydration layers. The bi- and tri- layer graphene significantly excludes both the first and second hydration layers. For monolayer graphene, however, most of the hydration layers are still present due to the atomic thickness of the membrane (See Table 5.2).

increases as we decrease the pore radius or increase the number of graphene layers. Also, the difference in the free energy barriers of K^+ and Cl^- increases for decreasing pore radius and increasing number of graphene layers. The free energy barriers appear due to dehydration of ions in the pore (see Fig. 5.5). As pore radius decreases and the number of graphene layer increases, the fractional dehydration in the solvation shell of ion increases, as shown in Fig. 5.2b.

5.4.4 Tables of Data

	monolayer									
r_p (nm)	0.21	0.34	0.48	0.57	0.6	0.73	0.79	0.96	1.11	1.2
I_{K} (nA)	0.048	0.325	1.027	1.563	1.874	2.770	3.176	5.034	6.614	7.848
I_{Cl} (nA)	0.006	0.282	1.033	1.589	1.794	2.842	3.291	4.944	6.688	7.627
$I_{\mathrm{K}}/I_{\mathrm{Cl}}$	7.50	1.15	0.99	0.98	1.04	0.97	0.96	1.02	0.99	1.03
	bilayer									
r_p (nm)	0.16	0.34	0.48	0.57	0.6	0.73	0.79	0.97	1.11	1.2
I_{K} (nA)	0	0.099	0.610	0.984	1.192	1.934	2.301	3.882	5.430	6.328
I_{Cl} (nA)	0	0.045	0.606	0.987	1.229	2.090	2.547	4.062	5.471	6.264
$I_{\mathrm{K}}/I_{\mathrm{Cl}}$	-	2.21	1.01	1.00	0.97	0.93	0.90	0.96	0.99	1.01
	trilayer									
r_p (nm)	0.14	0.34	0.48	0.57	0.6	0.73	0.79	0.97	1.11	1.2
I_{K} (nA)	0	0.059	0.446	0.819	0.949	1.586	2.050	3.280	4.755	5.380
I_{Cl} (nA)	0	0.005	0.430	0.684	0.981	1.701	2.062	3.479	4.699	5.727
$I_{\mathrm{K}}/I_{\mathrm{Cl}}$	-	10.94	1.04	1.20	0.97	0.93	0.99	0.94	1.01	0.94

TABLE 5.1: K^+ and Cl^- currents and their ratio in pores of various radii in monolayer, bilayer and trilayer graphene. We measure the currents by counting the ions that cross through the pore. There were no ion crossing events for the smallest pore in bilayer and trilayer graphene.

	K^+				Cl^-			
	$r_p = 0.21$ nm		$r_p = 0.34$ nm		$r_p = 0.21$ nm		$r_p = 0.34$ nm	
	n_1	n_2	n_1	n_2	n_1	n_2	n_1	n_2
monolayer	4.7 (3.8)	13.1 (13.2)	7.6 (6.2)	15.9 (15.4)	5.1 (3.8)	15.4 (15.4)	7.7 (6.4)	17.8 (17.6)
bilayer	3.0 (3.1)	5.1 (3.5)	7.3 (6.1)	9.7 (7.9)	2.4 (2.9)	6.5 (3.7)	7.4 (6.1)	11.1 (9.1)
trilayer	4.0 (3.1)	2.1 (3.5)	7.3 (6.1)	8.2 (7.9)	4.0 (2.9)	2.2 (3.8)	7.7 (6.1)	8.8 (8.3)
bulk	6.8	23.0	6.8	23.0	7.4	26.3	7.4	26.3

TABLE 5.2: The average number of water molecules, $\langle n \rangle$, in the first and second hydration layer for K^+ and Cl^- ions fixed at the center of the two smallest pores and in bulk. The estimated water loss considering only the geometric confinement is shown in parentheses. For the geometric estimate, mono-, bi-, and tri- graphene is approximated as a cylindrical hole of thickness 0.3, 0.6 and 0.9 nm, respectively.

	K^+		Cl^-	
	$r_p = 0.21$ nm	$r_p = 0.34$ nm	$r_p = 0.21$ nm	$r_p = 0.34$ nm
monolayer	2.0	1.3	-1.6	-1.5
bilayer	2.2	1.4	-1.9	-1.5
trilayer	2.1	1.3	-1.8	-1.4
bulk	1.4	1.4	-1.4	-1.4

TABLE 5.3: Average dipole orientation along the radial direction in the first hydration layer of K^+ and Cl^- in the two smallest pores and in bulk. When more water is excluded, especially from the first hydration layer, the remaining water more strongly orients its dipole to energetically compensate for the water loss.

6. ACCESS RESISTANCE IN GRAPHENE NANOPORES

The effect of the bulk electrolyte on the measured resistance of a constriction – e.g., a nanopore – has long been of interest, going all the way back to Maxwell in the context of electrical conduction. This *access* or *convergence resistance* is expected to be inversely dependent on pore radius, r_p, and independent of the bulk dimensions. Experiments and simulation both give contradictory results for graphene nanopores, some yielding a clear $1/r_p$ dependence and others seemingly lacking such a contribution (and giving only a $1/r_p^2$ dependence). Continuum simulations predict an unambiguous $1/r_p$ dependence, but can not address the effect of local atomic structure (e.g., the role of charged functional groups, membrane/pore fluctuations, etc.) that can obscure the behavior of the measured resistance. Addressing these issues requires all-atom simulations. We demonstrate that the convergence resistance is accessible with such simulations by using an appropriate finite size scaling, which we confirm with continuum simulations. The scaling form removes a contribution *dependent* on bulk dimensions and extrapolates to the large size limit. We show that clean graphene nanopores have both $1/r_p$ and $1/r_p^2$ contributions all the way down to the dehydration limit. This work will be published in future, however I presented this work in 2017 APS March Meeting [124].

6.1. Introduction

Ion transport through pores and channels plays an important role in physiological functions [112, 6, 75] and in nanotechnology, with applications such as DNA sequencing [19, 116, 95], imaging living cells [22, 23, 125], filtration [118], and desalination [117], among others. These pores localize the flow of ions and molecules across a membrane, where sensors – e.g., nanoscale electrodes for DNA sequencing [107, 104, 105, 106, 108, 109, 110] – can interrogate the flowing species as they pass through and where functional elements can selectivity regulate the movement of different species (e.g., ion types).

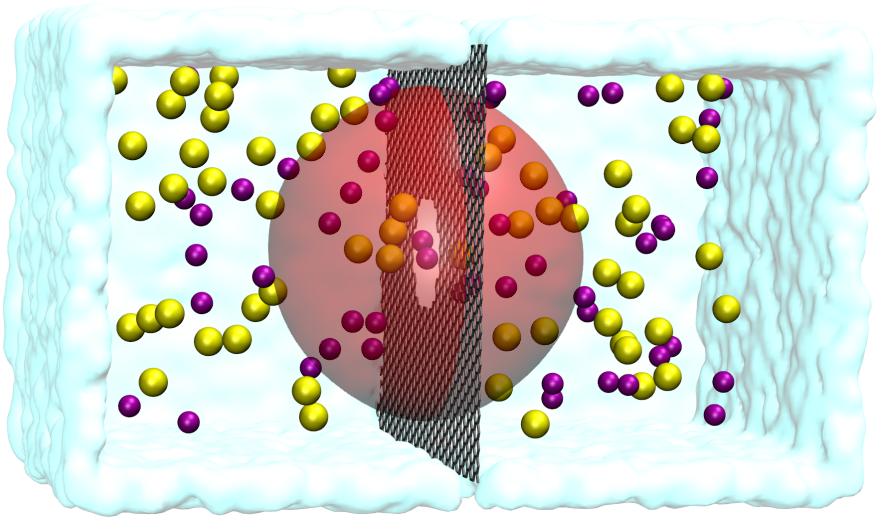

FIGURE 6.1: **Schematic of a graphene nanopore.** The ionic solution is partitioned by a graphene monolayer (shown as a grey, honey-comb membrane). Potassium (purple) and chloride (yellow) ions are shown as vdW spheres but water is not shown even though it is explicitly present in the simulations. The red, shaded region indicates the hemispherical access – or convergence – region.

In particular, from DNA sequencing [2, 11, 10, 126] to filtration [81, 1, 3, 120], graphene nanopores and porous membranes are one of the most promising avenues for applications. Novel fabrication strategies and designs are under development to create large-scale, controllable porous membranes [1, 3, 87] and graphene laminate devices [81, 113]. Moreover, the atomic thickness makes these systems ideal for interrogating ion dehydration [70], which both sheds light on recent experiments [1, 3, 87] and will help dissect the behavior of biological pores [70]. Dehydration has been predicted to give rise to ion selectivity and quantized conductance in long, narrow pores [79, 80, 83, 84, 85] but the energy barriers are typically so large that the currents are minuscule, a fact that is rectified by the use of membranes with atomic thickness [70, 111].

Despite the intense interest in graphene pores, the physical behavior of their resistance is still not understood. Experiments yield contradictory results, some showing a dominant $1/r_p$ access resistance contribution [2, 127] and some seemingly lacking this contribution [10]. To compound this discrepancy, simulations also yield contradictory results, some giving $1/r_p$ [128] and others $1/r_p^2$ [95]. We perform all-atom molecular dynamics

(MD) simulation using NAMD [88] to resolve the latter, showing that graphene pores, see Fig. 6.1, have both an access and pore resistance contribution. To do so, we develop a finite-size scaling analysis that shows that access resistance is accessible in all-atom MD simulations.

Hall's form of access resistance [94] is the classic result for ions to converge from bulk – far away from the pore – to the pore mouth,

$$R_{\text{Hall}} = \frac{\gamma}{4r_p}, \tag{6.1}$$

where γ is the electrolyte resistivity and r_p is the pore radius. This same form of resistance is given by Maxwell [129], Holm [130] and Newmann [131] for *electrical* "contact" resistance of a circular orifice. The above result assumes a hemispherical symmetry and homogeneous concentrations (i.e., no concentration gradients, even near the pore, and no charges/dipoles on the membrane), as well as an infinite distance between the pore and electrode. These assumptions can hold in linear response and for cleanly fabricated pores (e.g., recent low-aspect ratio pores show access only resistance following Eq. (6.1) [132]).

This form is independent of bulk dimension, which will hold for experiment so long as the bulk dimensions are large and balanced [1]. In confined geometries, however, strong boundary effects or unbalanced bulk dimensions modifies this behavior (e.g., in Scanning Ion Conductance Microscopy the imposed boundary close to the pore causes the access resistance to deviate from its standard form [23, 133]). In MD simulations, in particular, the simulation cells are both highly confined and periodic in order to collect sufficient statistical information on ion crossings. The electric potential is thus simulated via the application of a field perpendicular to the membrane surface, changing the potential landscape from that due to electrode surfaces.

To address these issues, we use the form of contact resistance without an infinite bulk. Its derivation is easier in rotational elliptic coordinates [129, 130, 131, 134], ξ and

[1] That is, the height of the, e.g., liquid cell should not be disproportionately large compared to its cross-sectional length.

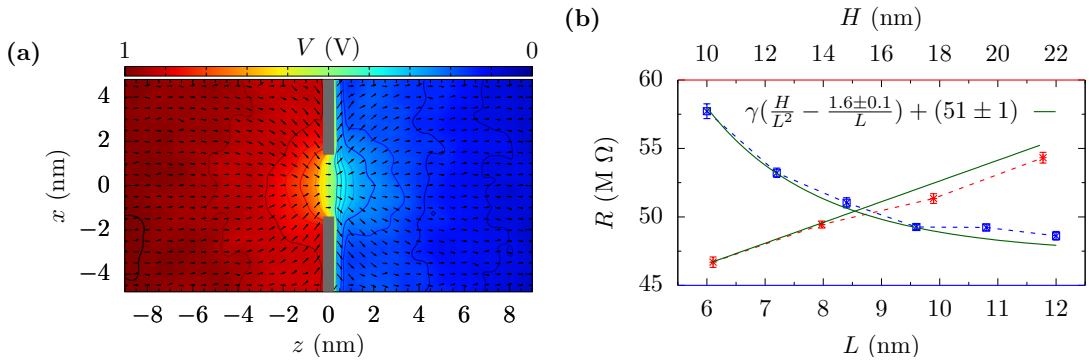

FIGURE 6.2: **Electric potential and access resistance in MD.** (a) The potential (color map), V, and normalized current density (arrows) when 1 V voltage is applied across a graphene membrane with a radius $r_p = 1.43$ nm pore. The resistance is large in the pore region, resulting in the potential drop almost completely across the membrane. (b) Resistance versus the simulation cell height H (red) and cross-sectional length L (blue) for the pore in (a). For R versus H (L), we use $L = 9.6$ nm ($H \approx 14$ nm). Equation (6.10) provides an excellent fit to the MD data. Note that the ansatz predicts R_∞ is higher than where it apparently converges to, which is due to the fact that the bulk dimensions were not changed in tandem as our ansatz indicates should be done. The value of R_∞, though, is consistent with the proper scaling procedure [see Fig. 6.4]. We will discuss this in more detail in a later contribution. We use the electrolyte resistivity as the value from MD simulations of a bulk-only cell (i.e., no graphene membrane), which gives $\gamma \approx 70$ MΩ nm. Error bars are ±1 Block Standard Error (BSE).

η, which are related to cylindrical coordinates, z and ρ, via

$$z = r_p \xi \eta \tag{6.2}$$

$$\rho = r_p \sqrt{(1+\xi^2)(1-\eta^2)}. \tag{6.3}$$

Laplace's equation then becomes

$$\frac{\partial}{\partial \xi}\left[(1+\xi^2)\frac{\partial V}{\partial \xi}\right] + \frac{\partial}{\partial \eta}\left[(1-\eta^2)\frac{\partial V}{\partial \eta}\right] = 0. \tag{6.4}$$

For boundary conditions, we consider a spheroidal electrode, reflecting the equipotential surfaces that form even when a flat electrode is present, and a circular pore. That is, (1) $V = V_0$ on the pore mouth ($\xi = 0$), (2) $V = 0$ on a spheroidal electrode at distance l ($\xi = l/r_p$), and (3) $\partial V/\partial \eta = 0$ on the membrane surface ($\eta = 0$).

We first examine Eq. (6.10) with continuum simulations, i.e., using Laplace's equation, of both rectangular and cylindrical (finite) cells using the COMSOL Multiphysics

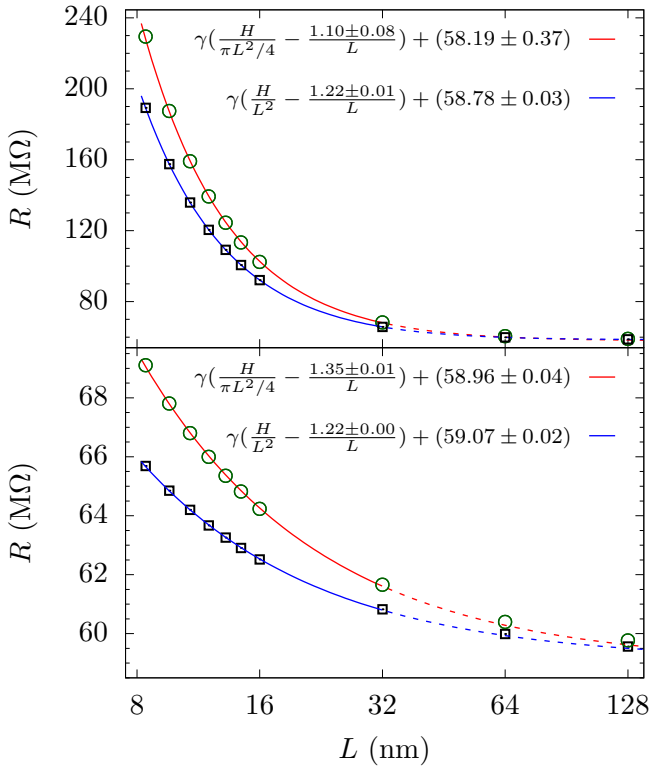

FIGURE 6.3: **Pore and access resistance in continuum simulations.** Resistance versus the bulk dimension L for cylindrical (green circles) and rectangular (black squares) finite boxes. The membrane height is 1 nm (i.e., approximately that for graphene plus the charged double layer) and the pore radius is $r_p = 1$ nm (and γ from MD for consistency). The bulk height is fixed to $H = 140$ nm in the top panel and the aspect ratio is fixed at $H = 2L$ in the bottom panel. We fit Eq. (6.10) for $L \leq 32$ (solid lines) and extrapolate to larger L (dashed lines). The fit for small values of L gives a good estimate of the true resistance, i.e., the small simulation sizes achievable with all-atom MD are sufficient for obtaining R_∞.

finite element solver. Figure 6.3 shows that continuum simulations yield excellent agreement with the ansatz and allow for the extrapolation of R_∞ using quite small simulation cells, which bodes well for the small simulation sizes typical of all-atom MD. Moreover, it suggests that using the constant aspect ratio cells is better, as it yields less deviation over all.

Although clearly idealizations, we already see features that reflect these boundary conditions from all-atom MD. Applying a constant electric field (here, along the z-axis) to the case of a pore in a graphene membrane gives rise to the flow patterns and fields in Fig. 6.2. As expected, due to the large pore resistance, a charged double layer forms [135],

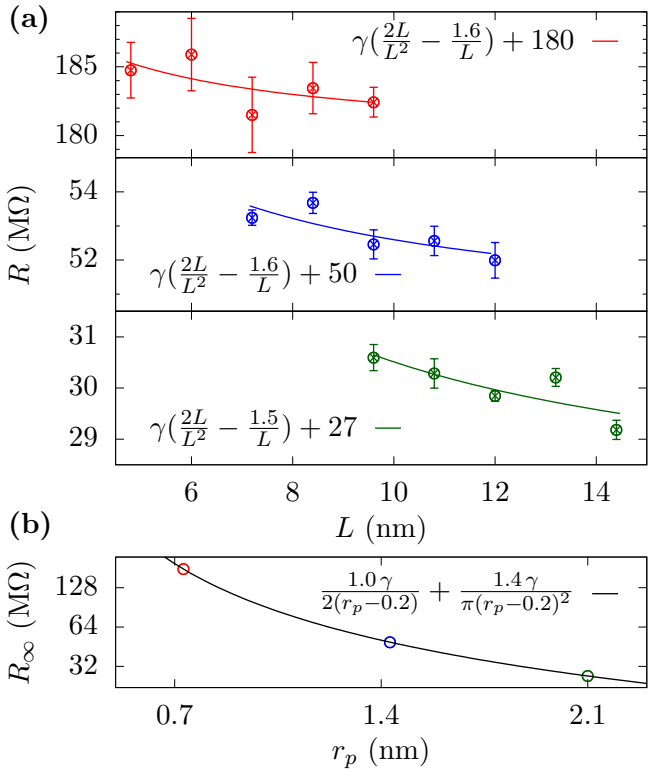

FIGURE 6.4: **Pore and access resistance in MD simulations**. (a) The three panels show the resistance versus cross-sectional length for different pore sizes. Here, we use $H = 2L$ as our ansatz suggests gives "balanced" simulation cell dimensions. Due to this, though, there are only mild changes in the resistance as L increases from small values to infinity. If an unbalanced cell is used, large changes in the resistance occur, see Fig. 6.2(b) and Fig. 6.3 upper panel. Moreover, this can also result in non-monotonic convergence to R_∞. (b) The bulk resistance extracted for the three pores versus the pore radius r_p. This shows agreement with the Maxwell-Hall resistance, so long as the pore radius is corrected by about 0.2 nm, a correction that is inline with accessible area for transport due to dehydration energy barriers at the pore edge. Error bars in R are ± 1 BSE. The errors in the fitted values of f and R_∞ are approximately ± 0.2 and ± 1 MΩ, respectively, for all of the pores. While the error bars are still sizable, the trend is clear: there is a decay following our ansatz (possibly with some finite size effects or nonlinearities) and the resistance R_∞ follows the Maxwell-Hall form.

with enhanced cation (anion) density on the positive (negative) voltage side. Almost all the voltage drop occurs just across the membrane [indeed, over about 1 nm, Fig. 6.2(a)]. The potential at the pore mouth (which is essentially the whole pore due to the atomic thickness) is not constant, but it is roughly so [the asymmetry between cations and anions (in ion sizes, charges, interactions), as well as other effects, distort the potential surface]. The deviation is mainly due to the fact that potassium ions come closer to the

graphene membrane than chloride ions, pushing the potential outward. The equipotential surfaces have roughly a hemispherical form (with deviation due to both simulation error – the accumulated simulation time needs to be very large – and also due to atomic scale features of the graphene, water, and ions). Due to the finite, large voltage, only boundary condition (3) does not appear to be present. However, we expect them to yield the right finite-size deviation from the Hall form (assuming, of course, that there are no charges near the pore, etc.).

Using those boundary conditions, Eq. (6.4) yields

$$\frac{V}{V_0} = 1 - \frac{\tan^{-1}\xi}{\tan^{-1}(l/r_p)}. \tag{6.5}$$

The current through the pore is then

$$I = -\frac{1}{\gamma}\int_0^{r_p} \frac{\partial V}{\partial z}\Big|_{z=0} \rho d\rho = \frac{2\pi r_p V_o}{\gamma \tan^{-1}(l/r_p)}, \tag{6.6}$$

giving the access resistance

$$R_{\text{access}} = \frac{\gamma \tan^{-1}(l/r_p)}{2\pi r_p} \approx R_{\text{Hall}}\left(1 - \frac{2r_p}{\pi l}\right), \tag{6.7}$$

where the approximation is up to $\mathcal{O}\left[\frac{r_p}{l}\right]^3$ [2]. In confined geometries, one needs to account for this correction term, especially in MD where the computational cost limits the bulk dimensions to well below 100 nm.

As one moves away from the membrane, the equipotential surfaces start to become flatter, taking on a bulk-like form. That is, the flow lines, while pointing radially inward near the pore entrance/exit, orient along the z-axis further away, as do the electric field lines. Thus, at some length, $l \sim \mathcal{O}(L/2)$, where $L \times L$ is the simulation cross-sectional

[2]When l is about $2r_p$, the higher order corrections are small, about 2.6%, likely much smaller than corrections due to atomic details at this scale.

area, the resistance transitions from "access like" to "bulk like", giving the total resistance

$$\begin{aligned} R =& R_{\text{bulk}} + 2R_{\text{access}} + R_{\text{pore}} \\ \approx& \frac{\gamma(H-2l)}{L^2} + 2\left(R_{\text{Hall}} - \frac{\gamma}{2\pi l}\right) + R_{\text{pore}}, \end{aligned} \tag{6.8}$$

where the factor of two accounts for both sides of the membrane. The first term – the bulk-like term – uses the total height H minus the two access-like regions of length l (note, of course, that this assumes that we have subtracted out the membrane thickness including charged double layers and that H is reasonably larger than $2l$). Figure 6.2(b) shows that we indeed have this bulk-like region as the resistance increases linearly with H [3].

If all the linear dimensions of the cell (experimental or theoretical) are large, the bulk component of the resistance will vanish and the resistance will be

$$R_\infty = 2R_{\text{Hall}} + R_{\text{pore}} = \frac{\gamma}{2r_p} + \frac{\gamma h_p}{\pi r_p^2}, \tag{6.9}$$

assuming cylindrical pore of height h_p. The computational power to reach this limit with all-atom MD is substantial. Thus, we would like to be able to extract R_∞ without taking the large cell limit.

We introduced Eq. (6.8) by supposing that there is a boundary between access-like and bulk-like at $l \sim \mathcal{O}(L/2)$ because, at the cell's edge (whether periodic or hard boundary), the resistance certainly can not be access-like. Moreover, this assumes H is reasonably bigger than $2l$, as otherwise one would have "feed" ions to the membrane surface but without having a true bulk region. The region around $l \approx L/2$ is some mix of access and bulk properties. We can thus introduce factors f_1 and f_2, both of which

[3] Some previous studies have shown the dependence of the ionic current on the cell height at constant voltage [136, 137]. However, in Ref. [136], the dependence is attributed to the difference in the applied electric field as the height changes – for a fixed voltage, the applied field should decrease as the box height increases – and, in Ref. [137], the difference is considered insignificant. However, in linear response, the resistance contribution from the pore should be independent of the applied field or voltage. While we have 1 V applied bias in order to have properly converged simulations, the main findings hold for smaller voltages, as continuum simulations demonstrate, and we note that there is roughly linear behavior of the I-V curve at this voltage, see Ref. [70].

we expect to be around 1, that quantify the bulk and the access resistance reductions, $\gamma f_1 L/A$ and $2\gamma/(\pi f_2 L)$, respectively. Here, A is the cross-sectional area of the box. Since these both yield $1/L$ corrections (as we anticipate the intermediate region will too), there is really only one factor $f = f_1 + 2/\pi f_2 \approx 1.6$ for rectangular cross-section and $f = 4f_1/\pi + 2/\pi f_2 \approx 1.9$ for cylindrical cross-section. We will use f as fitting parameter to extract R_∞,

$$R = \gamma \left(\frac{H}{A} - \frac{f}{L} \right) + R_\infty, \tag{6.10}$$

with H reasonably bigger than L.

6.2. Results

To test this scaling form, we will need to simultaneously increase L and H to remove the influence of the bulk-like region. If we take a constant aspect ratio, $H = \alpha L$, this reduces Eq. 6.10 to $R = \gamma \left(\frac{\alpha - f}{L} \right) + R_\infty$ (for a rectangular geometry). This suggests that if we knew f exactly, we could take $\alpha = f$ to remove the L-dependence of R, i.e., obtain $R = R_\infty$ for a finite size simulation cell. Since we do not know f exactly, we will take $\alpha = 2$, somewhat larger than the expected value of f, which will simultaneously ensure that R converges to R_∞ from above and reduce the amount that R changes by as L increases.

We now employ our finite-size scaling ansatz to address the access resistance in graphene nanopores. Figure 6.4(a) shows the resistance versus L for $H = 2L$. Using the extracted R_∞, we can determine the behavior versus r_p (due to computational cost, we examine only a small range of r_p). We allow, however, for one additional parameter in fitting R_∞ versus r_p, i.e., we take $r_p - \delta$ since ions do not cross too close to the pore edge (defined here by the van der Waals spheres of carbon). Figure 6.4(b) shows that a best fit gives a reduction of $\delta \approx 0.2$, exactly the value one would expect from steric effect of the hydration (i.e., without incurring an extra energy penalty) and consistent with Fig 6.8.

The other two fitting parameters (a and h_p in $a\gamma/2(r_p-\delta)-h_p\gamma/\pi(r_p-\delta)^2$) come out to be $a=1$ and $h_p=1.4$ nm [4]. That is, we find the Maxwell-Hall form for the access part and that the graphene effective thickness is 1.4 nm, which is in agreement with the extent of the charge double layer.

Thus, when properly defining the pore radius – to that giving the accessible area for ion transport – this shows that the resistance is a combination of both $1/r_p$ and $1/r_p^2$ behavior. Structure at the nanoscale – in this case, hydration layers and charge double layers – can obscure the parameters that appear in R_∞, making it difficult to properly determine the dependence of the resistance on the radius. More generally, there are many sources of ambiguity: Uncertainties in measured values and in the pore depth (e.g., multi-layer versus single layer graphene) and pore size (and aspect ratio / non-circularity), plus unknown charged functional groups or dipoles (that would enhance $1/r_p$ behavior by creating excess density at the membrane surface that "feeds" the current through the pore via its circumference), all affect either the balance of $1/r_p$ and $1/r_p^2$ behavior, or how well one can extract that behavior. This list can also include nonlinearities: MD simulations, for instance, often use high voltages. We demonstrate in Ref. [70] that around 2 V there is the onset of polarization-induced chaperoning of ions through the pore. This will tilt the balance in favor of access resistance as the limiting resistance (and thus the contributions of $1/r_p$ compared to $1/r_p^2$). Different membranes and different conditions can thus display different behavior, but "clean" graphene membranes with pores larger than the hydration radii of the ions have both access and pore contributions to the resistance for nanometer scale pores (as the pore radius gets larger, though, access resistance will then dominate, as seen in Ref. [2]).

[4] Due to the small number of pores examined, there are no error bars in these quantities.

6.3. Discussion

Our results demonstrate that one can indeed capture pore and convergence resistance in reasonably sized simulations, despite what one would expects based on long-range behavior of access resistance [136]. Moreover, our results imply that there is a minimum simulation size required to fully capture the resistance of the pore and convergence region. The deviation of access resistance from the Maxwell-Hall form depends on r_p/l, thus one needs the bulk dimension to be many times larger than r_p in order to capture its true behavior. For the simulation cell size that is too small, the potential and densities will not be fully converged and will be artificially distorted at the periodic boundary (or finite edge). These distortions obscure the dependence of the resistance versus pore radius.

Designing porous membranes requires an understanding of both the pore and the influence of the bulk electrolyte. Since the pores are of nanoscale and sub-nanoscale dimensions (about 1-2 nm in diameter for molecular detection and less than 1 nm for many biological ion channels and filtration applications), atomic scale details are often necessary to make effective predictions and to develop phenomenological models that elucidate the general physical behavior. However, conventional theories on fluid dynamics and ion-transport may not give correct predictions at this scale. For example, the nearby electrolytic medium deviates from continuum behavior [138, 139, 140, 141] once atomic details are taken into consideration. Inevitably, there will be a trade off between the physical dimensions of these simulations and the time scales (and voltages) reachable. Our finite-size scaling ansatz, Eq. (6.10), gives a theoretical approach to guide this trade off and converge the convergence resistance.

6.4. Methods

6.4.1 All-atom MD simulations

Our system consists of a single-layer graphene membrane with a pore in the center and in 1 Mol/L KCl solution, as shown in 6.1. We built the system using VMD 1.9.1

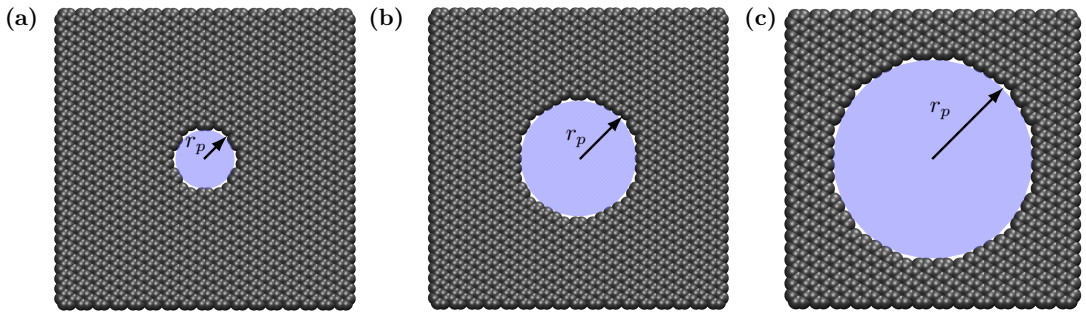

FIGURE 6.5: A 6 nm × 6 nm section of the graphene sheet showing the pores with radii (a) $r_p = 0.73$ nm, (b) $r_p = 1.43$ nm, and (c) $r_p = 2.09$ nm. We construct the pores by removing all carbon atoms within 0.8 nm and 1.5 nm, respectively, of the pore center and also removing any dangling bonds. The radius of the pore is, however, defined as the average distance between the center of the pore and the pore atoms at the edge minus the van der Waals radius of carbon.

[142] and perform all-atom molecular dynamics simulations using NAMD2 [88] with periodic boundary condition in all directions. The force field parameters are rigid TIP3P for water and CHARMM27 for the other atoms. We consider three pore sizes with radius $r_p = 0.73$ nm, $r_p = 1.43$ nm, and $r_p = 2.09$ nm, as shown in Fig. 6.5. We fix the outer edge of the graphene membrane but the bulk of the membrane has no confinement other than the C-C bonds of graphene. The simulations have an integration time step of 2 fs and Langevin damping of 0.2 ps for only carbon and water (via its oxygen atoms). Non-bonded interactions (van der Waals and electrostatics) have a cutoff of 1.2 nm. However, full electrostatic calculations occur every 4 time steps using the Particle Mesh Ewald (PME) method. We first minimize the energy of the system for 4000 steps (8 ps) and then heat it to 295 K in another 8 ps. A 1 ns NPT equilibration using the Nose-Hoover Langevin piston method [89] – to raise the pressure to 101 325 Pa (i.e., 1 atm) – followed by 3 ns of NVT equilibration generates the initial atomic configuration. An electric field perpendicular to the plane of the membrane drives the ionic current through the pore.

6.4.2 Pore radius

The radius of the pore is taken as the average distance between the center of the pore and the pore atoms at the edge minus the van der Waals radius of carbon (0.17

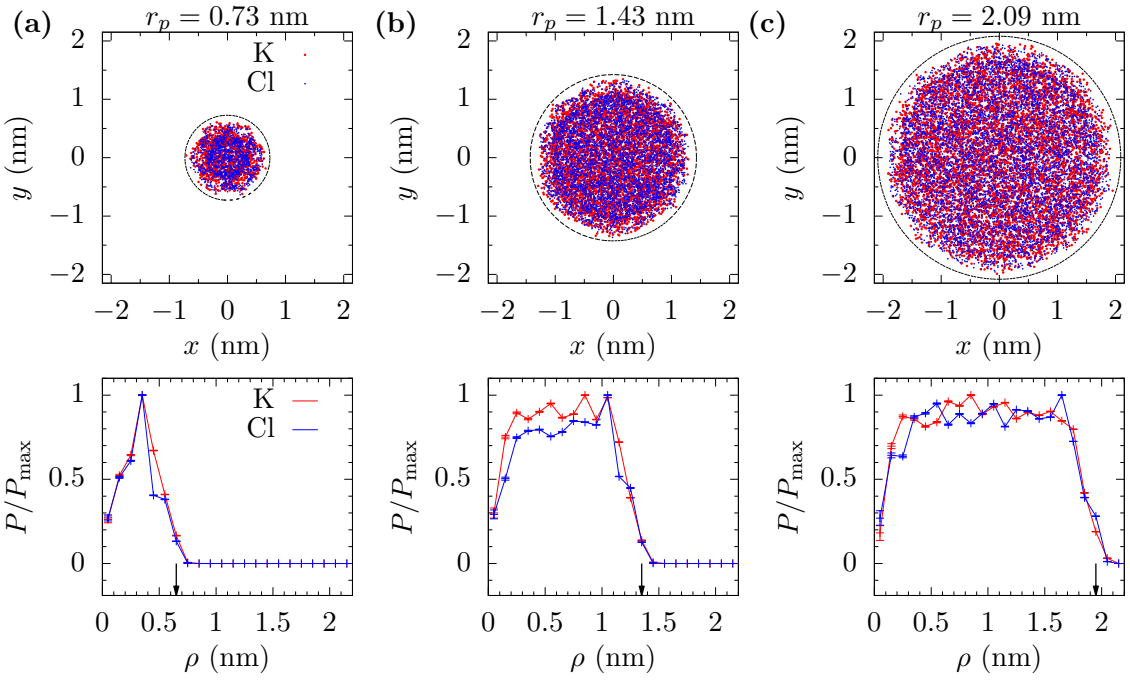

FIGURE 6.6: Probability distribution of K^+ and Cl^- ions crossing the pores with radius (a) $r_p = 0.73$ nm, (b) $r_p = 1.43$ nm, and (c) $r_p = 2.09$ versus the cylindrical coordinate $\rho = \sqrt{x^2 + y^2}$. The black arrow at the bottom shows the value of ρ which captures 99 % of crossing event for K^+ ions. The insets show scatter plots of ion crossings in the xy plane.

nm), i.e., the average distance between the center of pore and edge of the carbon atoms. However, the radius of the accessible area for the transport of ions is at least 0.1 nm to 0.2 nm smaller than r_p, as show in Fig. 6.6. This exclusion near the pore edge is due to vdW repulsion (finite ion size since we already account for carbon's vdW radius) and dehydration. Dehydration effects suggest that r_p should be corrected by around 0.2 nm. An alternative – but more complex – approach would be to weight each area element by a Boltzmann factor that contains the local free energy (e.g., of dehydration or other interactions).

6.4.3 Error analysis for convergence in time

We compute the error in the MD results using the Block Standard Error (BSE) method [90]. We divide a single MD run of duration T into number of contiguous blocks

of equal duration τ. The BSE is given by

$$\text{BSE} = \frac{s_\tau \sqrt{\tau}}{\sqrt{T}}, \tag{6.11}$$

where $s_\tau = \sqrt{\frac{\sum_i (\langle I_\tau \rangle_i - \langle I_T \rangle)^2}{(N_b - 1)}}$ is the standard deviation of the mean current $\langle I_\tau \rangle$, within each of the N_b blocks. The error bars in the plots are ± 1 BSE unless otherwise noted.

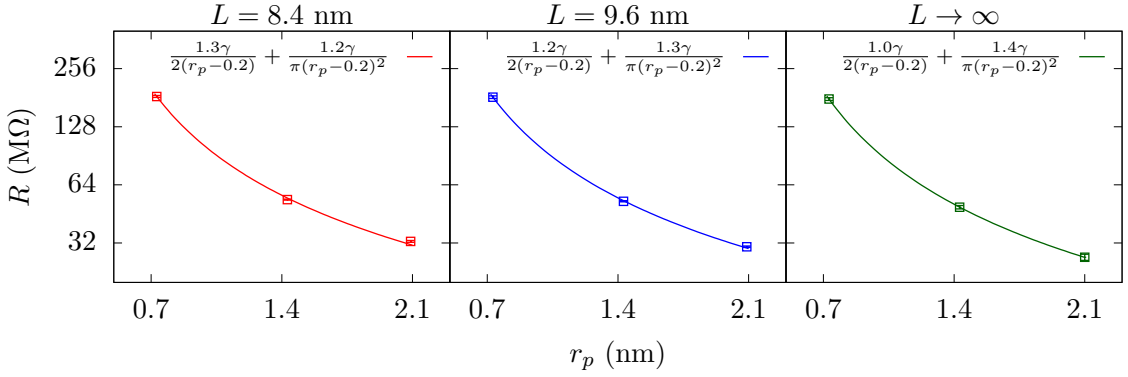

FIGURE 6.7: Maxwell-Hall form of access resistance fitted for $L = 8.4$ nm, $L = 9.6$ nm, and $L \to \infty$. Only when $L \to \infty$ do we get the expected access resistance, i.e., a coefficient of 1 in the Maxwell-Hall form.

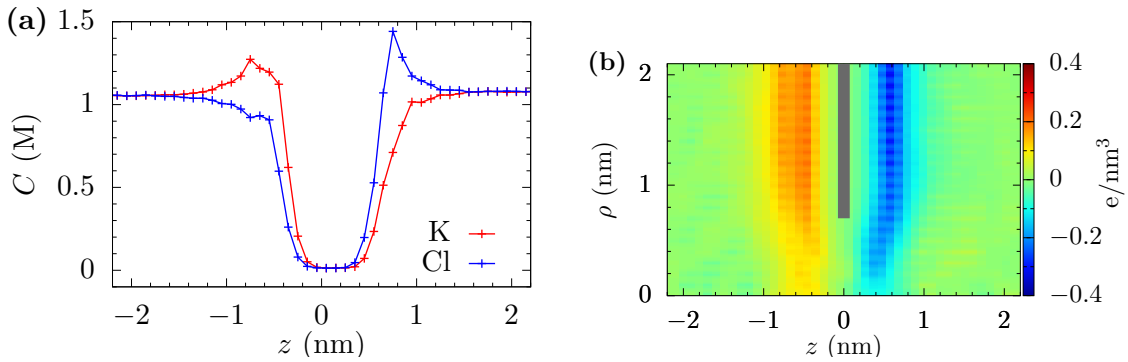

FIGURE 6.8: a) K^+ and Cl^- ion densities, and (b) net charge density when a 1 V voltage is applied across a graphene membrane with a radius $r_p = 0.73$ nm pore. The peak of K^+ ion concentration is closer to the graphene membrane than that of Cl^- due to smaller ionic size of the former. The z distance between the two peaks is about 1.5 nm.

6.4.4 Finite size scaling

In Fig. 6.7, we fit a modified form of Eq. 6.9 for $L = 8.4$ nm, $L = 9.6$ nm, and $L \to \infty$,

$$R_L = \frac{a_L \gamma}{2(r_p - \delta)} + \frac{h_L \gamma}{\pi(r_p^2 - \delta)} \tag{6.12}$$

where a_L and h_L are fitting parameter, and $\delta = 0.2$ nm. For $L = 8.4$ nm and $L = 9.6$ nm the access resistance is larger than Hall's form due to the unbalanced dimensions of the cell and the cell's relative size compared to the differing pore radii. Only when $L \to \infty$ do we get exactly the Maxwell-Hall value. Also the the fitted value of the membrane thickness is ≈ 1.4 nm. This is consistent with the separation of ion density peak on the two sides of the graphene membrane as seen in Fig. 6.8.

6.4.5 Electric Fields and Current density

We calculate the electrostatic potential and the charge density using VolMap plugin of VMD. The current density is the average ion displacement between the snapshots (10 ps) over the length of simulation,

$$\vec{J}(\vec{r}) = \frac{\sum_i q_i \vec{v}_i(\vec{r})}{dV}, \tag{6.13}$$

where the sum is over all the ions within the volume element dV(with $dx = dy = dz = 0.1$ nm) at position $\vec{r}$.

Figure 6.9 shows the flow pattern for three different cross-section cells with a pore radius $r_p = 1.43$ nm. In each of them the current density J quickly orients along z-axis. It is also seen from Fig 6.9 that J decreases with $A = L^2$, which can be understood by looking at the average value of J_z according to our model,

$$\langle J_z \rangle = \frac{V}{RA} = \frac{V}{\gamma(H - fL) + R_\infty A}. \tag{6.14}$$

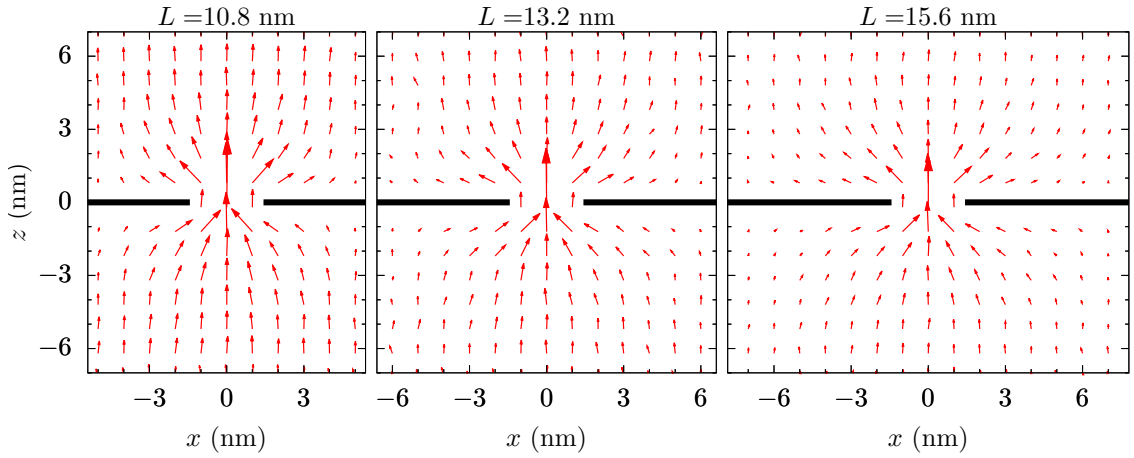

FIGURE 6.9: The current density J, showing the flow pattern for different cell cross-sections from MD simulations of a graphene nanopore with radius $r_p = 1.43$ nm. The flow quickly orient with the z-axis away from the pore regardless of the cross-sectional area of the cell. Note that J is not constant with L due to a changing balance of bulk and pore resistance.

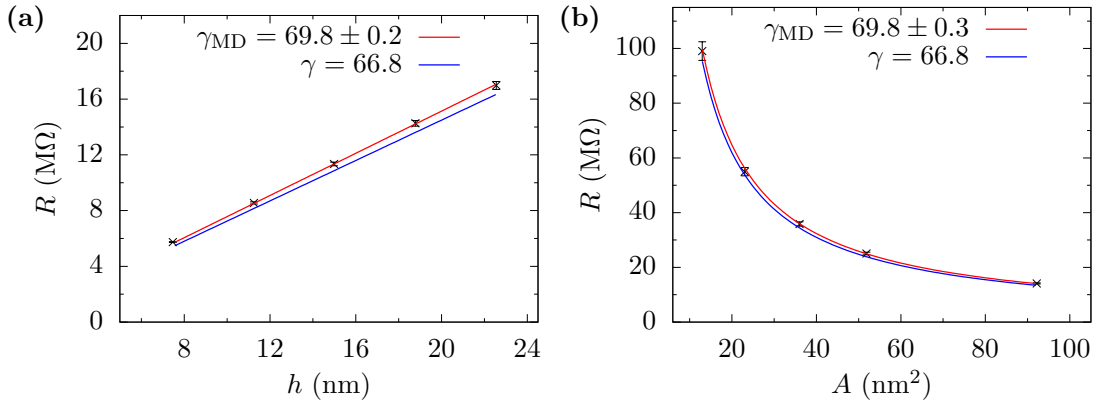

FIGURE 6.10: (a) Resistance versus simulation cell height and (b) resistance versus cross-sectional area for a bulk solution of 1 mol/L KCl. The red line gives γ_{MD} as the best fit to $R = \gamma_{\mathrm{MD}} h/A$, and the blue line shows standard resistivity $\gamma = 1/ne(\mu_{\mathrm{K}} + \mu_{\mathrm{Cl}}) \approx 67$ MΩ·nm.

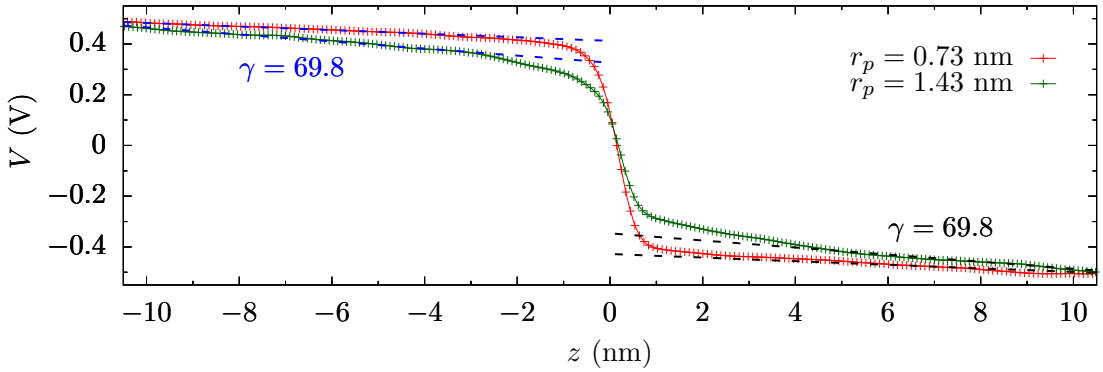

FIGURE 6.11: Potential V versus the z-distance averaged over a cylindrical region of radius $\rho = 1$ nm for $r_p = 0.73$ nm (red line) and radius $\rho = 2$ nm for $r_p = 1.43$ nm (green line). The slope of potential drop is constant and equal to bulk resistiviy beyond $|z| \gtrsim h_0/2$ (with $h_0 \approx 9$ for $r_p = 1.43$ nm and $h_0 \approx 7$ nm for $r_p = 0.73$ nm). But within $|z| \lesssim h_0/2$ the slope increases initially very slowly and then very rapidly near the pore ($z = 0$).

6.4.6 Bulk Resistivity

We calculate the bulk resistivity from our MD simulations using a cell without the graphene membrane/pore. The standard value of the bulk resistivity is $\gamma = 1/ne(\mu_{\rm K} + \mu_{\rm Cl}) \approx 67$ MΩ·nm. The value from MD is $\gamma_{\rm MD} \approx 70$ MΩ·nm, as shown in Fig. 6.10. It is to be noted that the actual value of resistivity of 1 M KCl at room temperature observed in experiments is $\gamma_{\rm exp} \approx 90$ MΩ·nm. At the high concentration of KCl (such as 1 mol/L), the conductance deviates from the linear expression, $\gamma = 1/ne(\mu_{\rm K} + \mu_{\rm Cl})$. However, the MD results give the conductance according to the linear expression.

In Fig. 6.11 we plot the potential drop along the z-direction when 1 V potential is applied across the graphene membrane. At larger distances, Δz from the pore, the potential drop, ΔV, is proportional to the bulk resistivity γ, since

$$\Delta V = I\Delta R = \frac{I\gamma\,\Delta z}{A}, \tag{6.15}$$

where ΔR is the resistance of the region away from the pore.

7. ENABLING PHOTOEMISSION ELECTRON MICROSCOPY IN LIQUIDS VIA GRAPHENE-CAPPED MICROCHANNEL ARRAYS

Photoelectron emission microscopy (PEEM) is a powerful tool to spectroscopically image dynamic surface processes at the nanoscale but is traditionally limited to ultra-high or moderate vacuum conditions. Here, we develop a novel graphene-capped multichannel array sample platform that extends the capabilities of photoelectron spectro-microscopy to routine liquid and atmospheric pressure studies with standard PEEM setups. Using this platform, we show that graphene has only a minor influence on the electronic structure of water in the first few layers and thus will allow for the examination of minimally perturbed aqueous-phase interfacial dynamics. Analogous to microarray screening technology in biomedical research, our platform is highly suitable for applications in tandem with large-scale data mining, pattern recognition, and combinatorial methods for spectro-temporal and spatiotemporal analyses at solid-liquid interfaces. This work was done in a large collaboration with Evgheni Strelcov (CNST, NIST), Hongxuan Guo (CNST, NIST), Alexander Yulaev (Department of Materials Science and Engineering, University of Maryland, College Park), Jian Wang (Canadian Light Source Inc., Canada), Narayana Appathurai (Canadian Light Source Inc., Canada), Stephen Urquhart (University of Saskatchewan, Canada) , John Vinson (Material Measurement Laboratory, NIST), and Andrei Kolmakov (CNST, NIST). The full version can be found in Ref [143].

7.1. Introduction

Electron spectroscopy [144, 145] in liquids aims to boost our understanding of the solid-liquid-gas interface relevant to environmental [146], energy [147, 148], catalysis [149] and biomedical research [150]. The pressure gap between the liquid or gaseous sample and the ultra-high vacuum (UHV) partition of the experimental setup (i.e., the electron energy analyzer) is usually bridged via judiciously designed differentially pumped electron

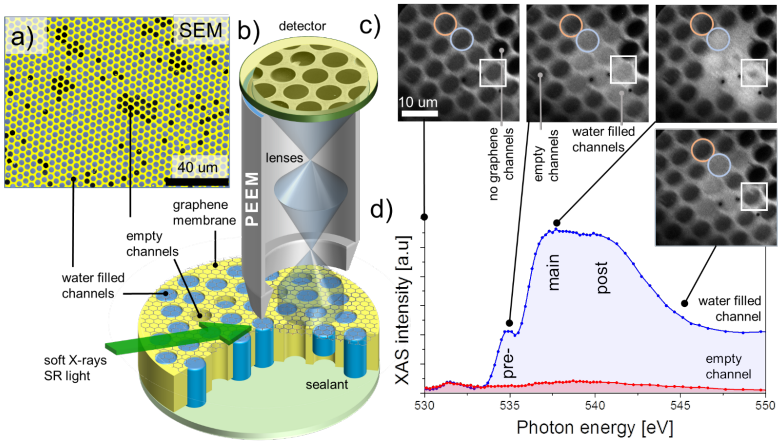

FIGURE 7.1: **Multichannel array sample design and experimental setup.** a) SEM (5 keV, color coded) image of water filled graphene-capped microchannel sample; the darker channels correspond to the graphene-capped but empty channels; b) The schematics of the PEEM and liquid cell setups; c) PEEM images of the water filled MCA collected at different X-ray energies while crossing the O K-edge; d) The resultant XAS spectra collected from different ROIs: water-filled (blue circle and spectrum) and empty (red circle and spectrum) channels. White squares mark the channels that exhibit the dynamic behavior. The spectra were normalized to incident X-ray intensity

optics [151] in combination with an advanced sample delivery systems [152, 153, 154, 155]. Experimental challenges, however, delayed the application of the photon-in electron-out imaging techniques to solid-liquid interfaces.

Novel 2D materials such as graphene have recently enabled an alternative, truly atmospheric pressure, photon-in electron-out X-ray photoelectron spectroscopy (APXPS) [156, 157, 158, 159, 160] via separation of the liquid or gaseous sample from UHV with a molecularly impermeable but yet electron transparent membrane. The subnanometer thickness of these membranes is smaller or comparable to an electron's inelastic mean free path (IMFP). Thus, the photoelectrons can traverse the membrane without significant attenuation while preserving their characteristic energies. The drastic reduction of the complexity of the experimental setup allowed the first scanning photoelectron microscopy (SPEM) measurements to be performed in liquid water through graphene-based membranes [157]. However, focused X-ray beam raster scanning during SPEM chemical

mapping impedes real-time or prolonged imaging of dynamic processes and decreases the lifetime of the membranes [161]. Therefore, an implementation of the full field of view (FOV) PEEM imaging, is advantageous due to reduced photons density at the sample and acquisition at video frame rate (see, e.g., Bauer [162] and references therein). Though FOV photoelectron imaging of the dynamic processes and objects, such as working catalysts or live cells, in their native high pressure gaseous or liquid environments, was a long-standing scientific goal, the differential pumping approach, so successful in APXPS, resulted only in 10-1 Pa of near sample pressures so far when applied to the PEEM setup [163]. The near-sample pressure value was limited mainly by the reduced lifetime of the imaging detector and possible discharge development between the sample and PEEM objective lens. An approach, which surmounts these restrictions, was proposed and tested in Ref [164] based on an environmental cell consisting of two 100 nm to 200 nm thick Si_3N_4 membranes with a liquid layer of micrometer thickness in between [165]. The PEEM images of the liquid interior of the cell can only be obtained within water soft X-ray transparency window (h 285 eV to 532 eV) and in transmission mode. For that Si_3N_4 membrane facing the PEEM objective lens was covered with a thin gold photocathode to convert transmitted X-rays to photoelectrons. These very first feasibility tests were, to the best of our knowledge, the only PEEM measurements of hydrated samples so far. On the other hand, prior PEEM research of buried interfaces revealed that the ultra-violet (UV) excited photoelectrons can be recorded through SiO_2 films from the depths exceeding many IMFPs [166]. Therefore, standard PEEM imaging in liquids and dense gasses can be feasible, in principle, using photoelectrons, provided that UHV and high-pressure environments are separated with a thin enough membrane. The latter possibility has been proven recently in an X-ray (X-)PEEM spectromicroscopy study of thermally induced segregation of nano-bubbles at a graphene-Ir interface filled with high pressure (GPa) noble gases [167] .

Here, we develop a novel, versatile microchannel array (MCA) platform that enables a wide range of photoelectron emission spectromicroscopies in liquids through a graphene membrane using UV or soft X-rays. Unlike the case of the aforementioned PEEM shadow

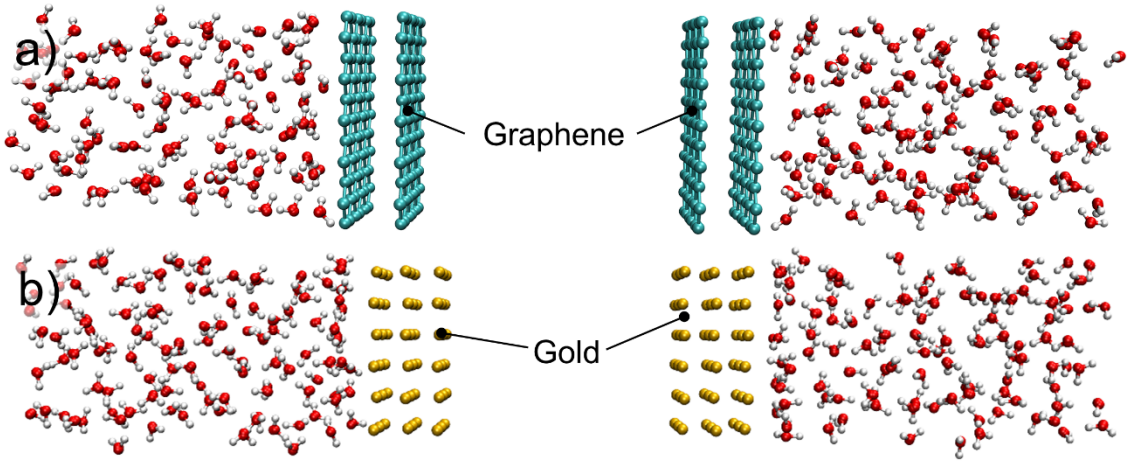

FIGURE 7.2: A snapshot from the MD simulation of water channel capped with a) graphene and b) gold. This is the full unit cell, and the simulation is periodic in all directions. Carbon and gold atoms are frozen during the simulation and, since there is periodicity in all directions, the water molecules can move around the boundary. The cross-section of the cell is kept fixed during an entire simulation, but the height of the box was adjusted during equilibration to obtain the targeted pressure and temperature.

imaging of immersed objects in the transmission mode, we were able to collect XAS spectro-temporal data of dynamic processes at the graphene-liquid interface in operando and submicron spatial resolution using standard laboratory or synchrotron-based PEEM equipment.

7.2. Methods

Multichannel array liquid sample platform for PEEM

PEEM at liquid-solid interfaces became possible as a result of successful development of a UHV compatible liquid sample MCA platform proposed in Ref [161]. Liquid water was impregnated into the gold coated silica matrix made of an ordered array of 300 m deep and 4 m wide parallel channels (Fig. 7.1 a). The top of the MCA was covered and isolated from the vacuum with an electron-transparent membrane made of a bilayer graphene (BLG) stack (Fig. 7.3 b). The bottom of the sample was sealed with a water-immiscible sealant.

The water filling factor (the ratio between water filled and empty channels) is routinely in excess of 85 % at the beginning of the experiment in UHV and slowly decays with time. The lifetime of the liquid inside such a sample usually exceeds a few hours and is limited mainly by the graphene quality and interfacial diffusion of water molecules. The MCA sample containing thousands of water filled micro-channels and capped with BLG was illuminated with monochromatic soft X-rays with an energy between 525 eV and 560 eV, covering the O K-absorption edge (535 eV). Under this excitation, fast photoelectrons and Auger electrons from the liquid which have the IMFP in excess of the thickness of the capping BLG membrane are able to escape into the vacuum with only minor attenuation [168]. These electrons constitute the total electron yield (TEY) which was used for spatially resolved XAS of the liquid or for spectrally resolved PEEM imaging (Fig. 7.1 b, c). Water containing areas have a sharp characteristic onset in the absorption cross-section around h 535 eV and thus can be easily discriminated from the other substrate materials (graphene, Au) which have a flat photoemission background across this energy range.

7.2.1 Liquid cell design, graphene transfer, sealing

MCA is based on a commercial silica-based glass matrix used for the fabrication of the multi-channel electron detectors. Before graphene transfer, the top surface of the MCA was metallized with Au (200 nm) / Cr (10 nm) film via sputtering. Monolayer graphene was CVD grown on the surface of a copper foil and coated with a PMMA sacrificial layer. The Cu foil was etched in 200 mol/m3 ammonium persulfate solution. The PMMA/graphene stack was then cleaned in deionized (DI) water and wet transferred onto a monolayer graphene on copper. After drying and annealing of the PMMA/BLG/Cu stack, the metal foil was etched again and after DI water cleaning the PMMA/BLG was transferred on to the Au surface of the MCA. After annealing the PMMA was stripped off by acetone. The acetone was gradually substituted by Isopropyl alcohol and then by DI water at room temperature. In the last step, the water-filled MCA sample was vacuum sealed from the back by UV curable glue or liquid Ga. The latter approach provides a

cleaner graphene-water interface.

7.2.2 PEEM setup

X-ray PhotoEmission Electron Microscopy (X-PEEM) was conducted at the 10ID-1 SpectroMicroscopy (SM) Beamline of the Canadian Light Source (CLS), a 2.9 GeV synchrotron. The beamline photon energy covers the range from 130 eV to 2700 eV, with a 1012 s-1 photon flux at the O K-edge (540 eV) and the beamline exit slit size set at 50 m x 50 m. The plane grating monochromator (PGM) is able to deliver a spectral resolution of better than 0.1 eV in the measured energy range, and the photon energy scale was calibrated based on samples with known XAS features. The monochromatic X-ray beam was focused by an ellipsoidal mirror down to 20 m spot and irradiated on the sample in PEEM at a grazing incidence angle of 16o. The sample is biased at -20 kV with respect to PEEM objective. FOV image stacks (sequences) were acquired over a range of photon energies at the O K-edge. The incident beam intensity was measured by recording the photocurrent from an Au mesh located in the upstream part of the PEEM beamline, and was used to normalize the PEEM data acquired from the sample ROIs. X-PEEM data were analyzed by aXis2000 (http://unicorn.mcmaster.ca/aXis2000.html), and other routine image processing software packages.

7.2.3 Simulations

We ran all-atom molecular dynamics (MD) simulations using NAMD [88] with a time step of 1 fs and periodic boundary condition in all directions. The simulation cell consists of 200 water molecules interfacing two parallel sheets of bi-layer graphene of cross-section 1.2 nm by 1.2 nm with 2 nm of vacuum between them, as shown in Fig. 7.2a. We use CA type carbon from the CHARMM27 force field and rigid TIP4p water [27]. Van der Waals and electrostatic interactions have a cut-off of 0.8 nm but we perform a full electrostatic calculation every 4 fs via the particle-mesh Ewald (PME) method [26]. To get the production run structures, we minimize the energy of the system in 4 ps and then raise the temperature to 295 K in another 4 ps. Then, we perform a 1 ns NPT (constant number of particles, pressure, and temperature) equilibration using the Nose-Hoover Langevin piston

method [89] to raise the pressure to 101,325 Pa (i.e., 1 atm) followed by 1 ns of NVT (constant number of particles, volume, and temperature) equilibration to generate the initial atomic configuration. The Langevin damping rate is 0.1 ps-1 on all atoms except the carbon atoms (which are fixed during the simulation). The final production run is 0.5 ns of NPT simulation starting with the equilibrated system from which 10 snapshots 50 ps apart were taken for calculating the XAS. Using the structures from MD, we calculate the oxygen K-edge XAS using the Bethe-Salpeter equation approach implemented within the OCEAN code [169, 170]. Spectra were calculated and averaged over two perpendicular X-ray polarizations in the plane of the graphene. The MD simulation cells were too large to carry out X-ray calculations, so each snapshot was cut down to contain only the single graphene layer surface and the first 128 water molecules placed within a 1.2 nm by 1.2 nm by 4.0 nm box, leaving a vacuum layer of 0.8 nm between the carbon atoms and the periodic image of the water. To account for the short electron inelastic mean free path, we average the contributions of the first 48 oxygen atoms, constituting a depth of approximately 1.0 nm from the shallowest to deepest water molecule below the surface. The bulk spectrum is the result of 5 MD snapshots taken from a 226 water molecule cell.

We also perform MD simulations for gold-capped water channels, see Fig. 7.2b. Here, the simulation cell consists of two sheets of gold each of cross-section 1.24 nm by 1.24 nm separated by 1.58 nm of vacuum on one side and 291 water molecules on the other. Each sheet has three layers of gold atoms that are frozen during the simulation. For gold atoms, we use the face-centered cubic (fcc) structure and the parameters for the van der Waals interaction between gold and water are from the Ref.[171]. The remaining simulation details are the same as the graphene-capped water channel. Our model does not take into account polarization of the metal due to interaction with water. Individual water molecules can produce a significant image potential on gold. For large numbers of water molecules, however, this image potential becomes insignificant due to the averaging out of dipole orientations [172]. Other studies show that polarization does not have a significant effect on interfacial water structure [173]. Since the dominant effect in gold is

the screening of the core hole, any small structural change due to polarization or other interactions will not substantially change the XAS spectrum. For determining whether two water molecules are hydrogen bonded, we use the criteria that the oxygen-oxygen distance is less than 0.35 nm and the oxygen-oxygen-hydrogen angle is less than 35° [174]. The molecules are counted as double donor (DD), single donor (SD), and non-donor (ND) when the number of hydrogen atoms contributing to hydrogen bonds is two, one, and zero, respectively.

Oxygen K-edge XAS Calculations

The OCEAN code requires the one-electron wavefunctions of the ground-state system as an input for the Bethe-Salpeter equation (BSE). For this, we use density functional theory (DFT) within the local density approximation as parameterized by Ceperley, Alder, Perdew, and Wang [175]. We make use of the QuantumESPRESSO code [176], and take advantage of an efficient k-point interpolation scheme [177, 178]. The BSE approach retains two electron-hole interaction terms in addition to the non-interacting DFT Hamiltonian; the attractive direct and repulsive exchange. We calculate these explicitly using a combination of a local and a real-space basis. A pseudopotential inversion scheme is necessary to reconstruct the all-electron character of the DFT conduction-band states near the core hole [175]. Within the BSE, the dielectric response of the system screens the direct interaction, for which we take the random phase approximation coupled with a model dielectric function to capture the long-range response [179]. We use an energy cut-off of 952 eV (70 Ryd.) for the DFT calculations and calculate DFT states at the Gamma point. The k-point interpolation scheme expands this to a 2 2 2 k-point mesh for the x-ray calculations. For the graphene surface, we use a 1.2 nm by 1.2 nm by 4.0 nm box containing 128 water molecules and 66 carbon atoms. For the gold, this was changed to a 1.224 nm by 1.224 nm cross section with 36 gold atoms. The screening calculation uses 9000 bands, covering a range of 100 eV above the Fermi level. The BSE states include 5100 bands of which approximately 4456 (4390) were unoccupied for the graphene (gold) surface cells with a metallic surface layer, not all k-points will have the same number of

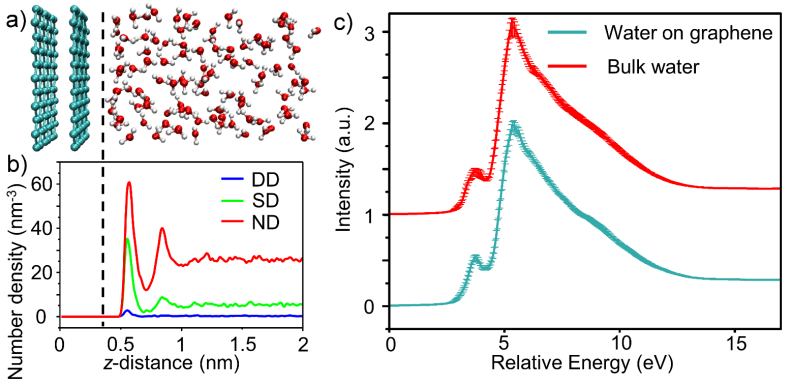

FIGURE 7.3: **Water structure, hydrogen bonding, and theoretical XAS spectrum.** a, A snapshot of the bilayer graphene-capped water channel from the MD simulations. The simulation is periodic in all directions with the full unit cell shown in Fig. 7.2a. b, Density of water molecules with differing numbers of hydrogen bonds they donate (DD=double donor, SD=single donor, and ND=non-donor) versus distance from the graphene sheet. a and b share the same z-axis scale and alignment. The graphene induces a density oscillation in the water, as well as a change in the relative population of different donating species. c, The oxygen K-edge XAS spectrum for water at the graphene interface (green) and the spectrum for bulk water (red) as a function of excitation energy. The bulk water spectrum was y-offset for clarity. The presence of graphene does not significantly affect the spectrum of water. This is due to the weak graphene-water interaction: The graphene surface reduces the number of hydrogen bonds, but does not otherwise align water molecules at the surface. Moreover, the core-hole screening by the BLG is not strong enough to suppress the pre-edge peak (as it does with gold). Thus, this peak, as well as the relative location of the main peak are the same for bulk water and water at the graphene interface. The error bars of the XAS curves denote the variance of the mean across different MD snapshots.

occupied bands. The local basis for calculating the exchange and short-range components of the direct interaction consists of four projectors per angular momentum channel for s-d and three for f. The real-space basis is a regular 24 24 80 grid. The bulk cells contain 226 water molecules within a 1.8 nm by 1.8 nm by 2.1287 nm box and the real-space basis is a 32 32 40 grid. All other parameters are the same as for the cells with surfaces. The long-range part of the dielectric response to the core-hole potential is calculated using a model dielectric function. For all three setups, we used the bulk water dielectric constant of 1.8.

7.3. Results

Figure 7.1c shows a set of four PEEM images of the BLG-capped water filled MCA recorded at different energies while scanning across the O K-edge. The contrast in these images originates from spatial variations of the local TEY from the Au-coated MCA matrix and the graphene-capped MCA channels. The graphene-capped channels can either be filled with liquid water or be empty. A fraction of the channels does not have a graphene cap and these have the lowest signal in Fig. 7.1 c. As can be seen, the contrast between water filled and empty channels is minuscule below O-K absorption threshold at h 535 eV and increases drastically above it. Such sequences of PEEM images constitute a spatial X-ray absorption chemical map and specific regions of interest (ROI) can be designated for site-selective XAS. Figure 7.1d compares two such XAS spectra collected from two ROIs: water filled (blue) and empty (pink) channels. The empty channels show weak spectral feature at 532 eV characteristic of carbonyl group containing hydrocarbons [180]. These contaminations have been previously observed in XAS of ice and water [181] and in our case can also be due to polymethylmethacrylate (PMMA) residue at the BLG membrane left after graphene transfer [182]. The filled channels, on the other hand, demonstrate an XAS spectrum with pronounced features and a shape typical of liquid bulk water probed via TEY or in transmission detection modes (see reviews [183, 184] and references therein). Such a spectrum is a result or transitions from the strongly localized O 1s core level of water molecules to unoccupied valence orbitals derived from the gas-phase 4a1 and 2b2 states[185]. The particular feature of these unoccupied orbitals is their p character (due to the dipole selection rule) that results in their noticeable directionality and spatial extension far beyond hydrogen atoms. Since hydrogen atoms participate in hydrogen bonding (H-bonding) in water, XAS O K-edge spectra are very responsive to variations in electronic and/or structural environment around the probed water molecule. In good accordance with prior XAS works on liquid water [181, 183], our PEEM-derived XAS spectrum in Fig. 7.1 d has a characteristic pre-edge (535 eV), main peak (537.5 eV) features and a post-edge band around 541 eV. The commonly accepted interpretation of water

XAS features assigns these pre-peak and main band to the excitation of water molecules with one broken (or largely distorted H-bond, a so called single-donor (SD) molecules) while the post-edge band corresponds to the molecular environment with strong H-bonds (double donor (DD) molecules) and increased tetrahedrality [185].

It is important to emphasize that the XAS spectrum in Fig. 7.1 originates from the first few layers of water at the graphene-water interface. This interfacial sensitivity of the through-membrane PEEM spectromicroscopy stems from the attenuating role of the BLG layer, which has low transparency for slow few eV secondary electrons emitted from deeper water layers [186]. Therefore, the bulk-like nature of our spectra indicates that interaction of interfacial water molecules with graphene is very weak and neither the electronic nor the geometrical structure are strongly affected by the graphene. A previous XAS study of interfacial water in contact with gold revealed the significant suppression of the pre-edge peak under similar experimental conditions [187]. Thus, graphene represents a model benchmark material to study interfacial water behavior with PEEM.

Modelling of the graphene-water interface

To gain deeper insight into these differences, we simulate graphene-water structures with all-atom molecular dynamics (MD) simulations and perform calculations of the oxygen K-edge XAS, as described in the Methods. As shown in Fig. 7.3 a, b, the structure of the water about 1 nm away from the graphene is already bulk-like. The presence of the graphene does, however, induce water density oscillations (see Fig. 7.4 a) and results in interfacial water losing about 30 % of its hydrogen bonds (Fig. 7.4 b). The latter is reflected in the different proportions of donating species of water near the graphene (Fig. 7.3 b). Despite these changes in interfacial H-bonding and density, the theoretically computed XAS spectrum is similar to one computed for bulk water (Fig. 7.3c). As with the experimental results, the characteristic pre-edge peak is present in both spectra and of approximately the same relative magnitude compared to the main peak. This is in stark contrast to the aforementioned XAS of liquid water near the gold surface [187], where it was found that the large increase in broken hydrogen bonds (expected to strengthen

the pre-edge peak) is overwhelmed by the screening provided by the gold atoms. The highly effective screening of core holes created near the gold surface weakens the core-hole potential, blue-shifting XAS spectrum and reducing the intensity of the lower-energy peaks (see Fig. 7.5b). On the other hand, the BLG layer does not screen the X-ray induced core hole appreciably, and thus does not suppress the pre-edge peak. In total, for water near a BLG layer, both the structural and electronic effects of the surface are significantly weaker than for water-gold interface, resulting in the similarity of the interfacial and bulk water XAS.

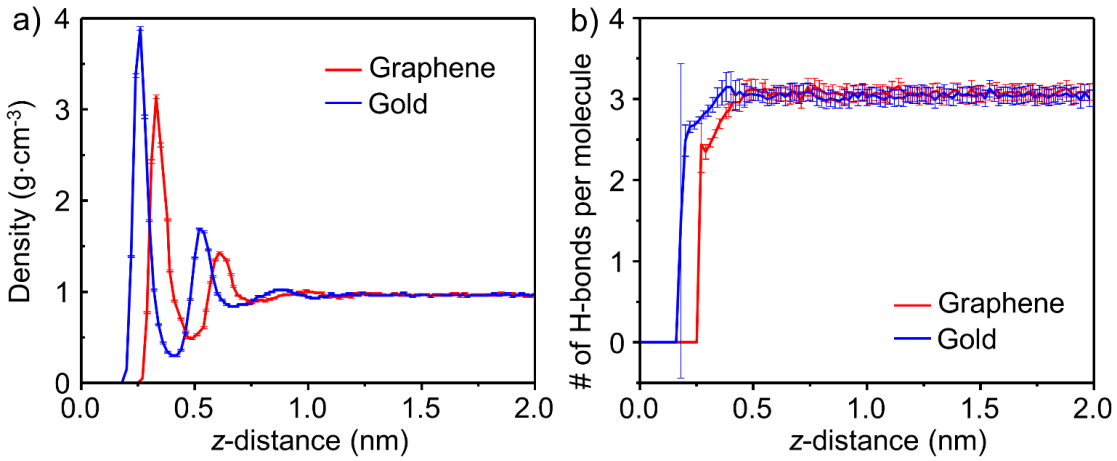

FIGURE 7.4: a) Density profile for water adsorbed on graphene and gold as a function of distance from the interface. In both cases, oscillations are induced by the presence of the surface, with gold giving rise to slightly stronger oscillations than graphene; b) Hydrogen bonds per water molecule vs. distance, z, from the graphene/gold surface. The number of hydrogen bonds rapidly approaches the bulk value away from the surface. Nearby the surface, however, the number of hydrogen bonds are depleted by about 30 %.

7.4. Summary

In summary, we developed a novel multichannel, graphene-capped array platform that is UHV compatible and is able to retain liquid samples for hours. The latter, in conjunction with high electron transparency of the bilayer graphene, allow us to conduct spectro-microscopy studies of the graphene-water interface with high temporal resolution

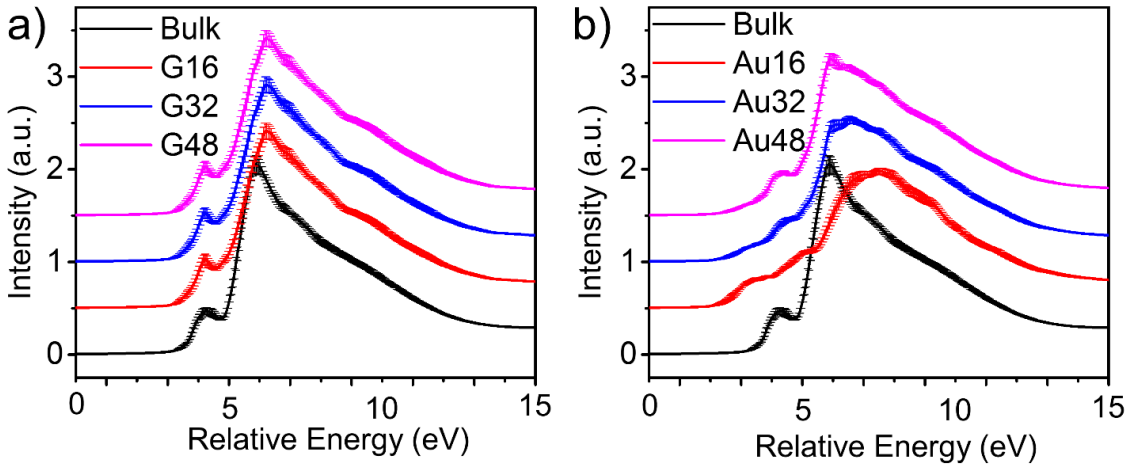

FIGURE 7.5: The changes in the XAS water spectra with averaging over the first 16, 32, or 48 water molecules for both a water interfacing graphene and b water interfacing gold. While both become more bulk-like as further water molecules are included, the changes in the spectrum of the gold-interfacing water are much more dramatic. Spectra are y-offset for clarity of presentation.

using standard PEEM instrumentation. The shape of the oxygen K-edge XAS spectra, measured in TEY mode, were similar to bulk water. This result reveals that bilayer graphene does not significantly distort the electronic structure of water in the first few water layers. Our theoretical calculations indicate that this is due to very weak water core-hole screening by the graphene and weak water-graphene interaction. Since the microarray comprises a lattice of identical water-filled objects, it is suitable to use this platform in tandem with powerful data mining, pattern recognition, and combinatorial approaches for spectro-temporal and spatiotemporal analysis. Using these algorithms, we were able to discriminate between different scenarios of water radiolysis and detect the appearance of the metastable wetting water layer at the later stages of bubble formation. Our work opens up new avenues for investigating electrochemical, catalytic, environmental and other phenomena in liquids using standard (X)PEEM, SPEM, XPS and LEEM setups.

8. CONCLUSIONS

Nonlinear dynamics and transport process at the nanoscale are both scientifically interesting and technologically important. We focused on thermal transport and ion transport at the nanoscale, which can be solved using classical molecular dynamics simulations. Thermal transport at the nanoscale is key to the operation and efficiency of many devices and processes, such as thermoelectrics, thermal management of miniaturized electronics, among others. Ion transport through nanoscale pores, on the other hand, is an integral part of cell physiology and is also the main component of membrane technologies such as desalination, nanopore sequencing, and sensing.

For thermal transport at the nanoscale, we gave a new perspective on thermal transport simulations. In particular, we demonstrate that there is a crossover behavior in the thermal transport, where it first increases then subsequently decrease as the thermal contact with the reservoir is strengthened. This behavior has important implications for both the tunability of transport – it suggests a route to nonlinearly modulate the conductance by controlling, eg., surface-molecule interactions – and for its proper numerical simulation.

We also studied ion transport through porous graphene membranes, which is a promising candidate for ionic sieving and bio-sensing due to their flexibility, mechanical and chemical stability, and atomic thickness. We observed the nonlinear behavior of the ionic current through graphene pores as the radius of a pore is reduced to the sub-nanometer scale. This nonlinear response is characterized by a sharp rise in pore resistance and noise in the current which is due to the encroachment of the pore edge on the hydration layers of the ions. Our results show that hydration layers and the atomic structure of the pore play a defining role in transport properties and give rise to selective behavior. Moreover, we not only developed a mechanistic understanding of selective transport in graphene devices but also presented phenomenological models which will be useful in engineering selectivity.

We also show that one can use layering of graphene (from mono- to bi- to tri- layer) to tune ion selectivity and exclusion. The layering forces ions to dehydrate more than

in monolayer graphene for which the atomic thickness allows substantial hydration just outside the membrane. In essence, layering gives the second knob to the tunability, where the length of the pore is varied at the atomic scale, the scale necessary to impact hydration structure. These findings give an ideal approach to understanding/dissecting biological ion channels by quantifying dehydration and simultaneously yield a method to achieve a target ion exclusion/selectivity while enhancing water flow rate.

Moreover, we give a simple theoretical method to extract the combined pore and convergence resistance. Using this method, we resolved a discrepancy between experiments and simulations of ion transport through graphene nanopores. This makes connections with results in both ionic and electronic transport theory, going all the way back to Maxwell's contact resistance of circular orifice, and both theory/computation and experiment. Additionally, we show that graphene does not significantly distort the electronic structure of water in the first few water layers due to weak water core-hole screening by the graphene and weak water-graphene interaction. In conjunction with the high electron transparency of the graphene, this allows one to conduct spectromicroscopy studies of the graphene-water interface with high temporal resolution using standard PEEM instrumentation.

Thus our work touches the fundamental aspects of nonlinear behavior and transport properties in the nanoscale science, as well as guide the practical application of various emerging nanotechnologies.

BIBLIOGRAPHY

1. O'Hern, S. C. *et al.* Selective ionic transport through tunable subnanometer pores in single-layer graphene membranes. *Nano Lett.* **14**, 1234–1241 (2014).

2. Garaj, S. *et al.* Graphene as a subnanometre trans-electrode membrane. *Nature* **467**, 190–193 (2010).

3. Jain, T. *et al.* Heterogeneous sub-continuum ionic transport in statistically isolated graphene nanopores. *Nat. Nanotechnol.* **10**, 1053–1057 (2015).

4. Wiederrecht, G. *Handbook of nanofabrication* (Academic Press, 2010).

5. Bonetto, F., Lebowitz, J. & Rey-Bellet, L. Fourier's law: a challenge for theorist. In Fokas, A., Grigoryan, A., Kibble, T. & Zegarlinski, B. (eds.) *Mathematical Physics 2000*, 128 (World Scientific, 2000).

6. Bagal, S. K. *et al.* Ion Channels as Therapeutic Targets: A Drug Discovery Perspective. *J Med Chem* **56**, 593–624 (2012).

7. Wallace, P. R. The band theory of graphite. *Physical Review* **71**, 622 (1947).

8. Boehm, H.-P., Clauss, A., Fischer, G. & Hofmann, U. Das adsorptionsverhalten sehr dünner kohlenstoff-folien. *Zeitschrift für anorganische und allgemeine Chemie* **316**, 119–127 (1962).

9. Novoselov, K. S. *et al.* Electric field effect in atomically thin carbon films. *science* **306**, 666–669 (2004).

10. Schneider, G. F. *et al.* DNA translocation through graphene nanopores. *Nano Lett.* **10**, 3163–3167 (2010).

11. Merchant, C. A. *et al.* DNA translocation through graphene nanopores. *Nano Lett.* **10**, 2915–2921 (2010).

12. Chien, C.-C., Velizhanin, K. A., Dubi, Y. & Zwolak, M. Tunable thermal switching via DNA-based nano devices. *Nanoetchnology* **24**, 095704 (2013).

13. Chang, C., Okawa, D., Majumdar, A. & Zettl, A. Solid-state thermal rectifier. *Science* **314**, 1121–1124 (2006).

14. Saira, O.-P. *et al.* Heat transistor: Demonstration of gate-controlled electronic refrigeration. *Physical review letters* **99**, 027203 (2007).

15. Ben-Abdallah, P. & Biehs, S.-A. Near-field thermal transistor. *Physical review letters* **112**, 044301 (2014).

16. Shakouri, A. Nanoscale thermal transport and microrefrigerators on a chip. *Proceedings of the IEEE* **94**, 1613–1638 (2006).

17. Morpurgo, A., Klapwijk, T. & Van Wees, B. Hot electron tunable supercurrent. *Applied physics letters* **72**, 966–968 (1998).

18. Chen, F. & Cai, W. Nanomedicine for targeted photothermal cancer therapy: where are we now? *Nanomedicine* **10**, 1–3 (2015).

19. Kasianowicz, J. J., Brandin, E., Branton, D. & Deamer, D. W. Characterization of individual polynucleotide molecules using a membrane channel. *Proc. Natl. Acad. Sci. U. S. A.* **93**, 13770 (1996).

20. Branton, D. *et al.* The potential and challenges of nanopore sequencing. *Nat Biotechnol* **26**, 1146–1153 (2008).

21. Edel, J. B. & Albrecht, T. *Engineered nanopores for bioanalytical applications* (William Andrew, 2013).

22. Hansma, P. K., Drake, B., Marti, O., Gould, S. A. & Prater, C. B. The scanning ion-conductance microscope. *Science* **243**, 641–643 (1989).

23. Korchev, Y. E., Bashford, C. L., Milovanovic, M., Vodyanoy, I. & Lab, M. J. Scanning ion conductance microscopy of living cells. *Biophys. J.* **73**, 653–658 (1997).

24. Ullersma, P. An exactly solvable model for brownian motion: I. derivation of the langevin equation. *Physica* **32**, 27–55 (1966).

25. Leach, A. R. *Molecular modelling: principles and applications* (Pearson education, 2001).

26. Darden, T., York, D. & Pedersen, L. Particle mesh ewald: An n log (n) method for ewald sums in large systems. *The Journal of chemical physics* **98**, 10089–10092 (1993).

27. Jorgensen, W. L., Chandrasekhar, J., Madura, J. D., Impey, R. W. & Klein, M. L. Comparison of simple potential functions for simulating liquid water. *The Journal of chemical physics* **79**, 926–935 (1983).

28. Ryckaert, J.-P., Ciccotti, G. & Berendsen, H. J. Numerical integration of the cartesian equations of motion of a system with constraints: molecular dynamics of n-alkanes. *Journal of Computational Physics* **23**, 327–341 (1977).

29. Andersen, H. C. Rattle: A velocity version of the shake algorithm for molecular dynamics calculations. *Journal of Computational Physics* **52**, 24–34 (1983).

30. Darve, E., Rodríguez-Gómez, D. & Pohorille, A. Adaptive biasing force method for scalar and vector free energy calculations. *J. Chem. Phys.* **128**, 144120 (2008).

31. Hénin, J. & Chipot, C. Overcoming free energy barriers using unconstrained molecular dynamics simulations. *J. Chem. Phys.* **121**, 2904–2914 (2004).

32. Peyrard, M. & Bishop, A. R. Statistical mechanics of a nonlinear model for DNA denaturation. *Phys. Rev. Lett.* **62**, 2755–2758 (1989).

33. Dauxois, T., Peyrard, M. & Bishop, A. R. Dynamics and thermodynamics of a nonlinear model for DNA denaturation. *Phys. Rev. E* **47**, 684–695 (1993).

34. Dauxois, T., Peyrard, M. & Bishop, A. R. Entropy-driven DNA denaturation. *Phys. Rev. E* **47**, R44–R47 (1993).

35. Joyeux, M. & Buyukdagli, S. Dynamical model based on finite stacking enthalpies for homogeneous and inhomogeneous dna thermal denaturation. *Physical Review E* **72**, 051902 (2005).

36. Velizhanin, K. A., Sahu, S., Chien, C.-C., Dubi, Y. & Zwolak, M. Crossover behavior of the thermal conductance and kramers transition rate theory. *Scientific Reports* **5** (2015).

37. Sahu, S., Velizhanin, K., Chien, C.-C., Dubi, Y. & Zwolak, M. Crossover behavior of the thermal conductance and kramers' transition rate theory. *Bulletin of the American Physical Society* **60** (2015).

38. Li, N. *et al. Colloquium* : Phononics: Manipulating heat flow with electronic analogs and beyond. *Rev. Mod. Phys.* **84**, 1045–1066 (2012).

39. Dubi, Y. & Di Ventra, M. Colloquium: Heat flow and thermoelectricity in atomic and molecular junctions. *Rev. Mod. Phys.* **83**, 131 (2011).

40. Yang, N., Xu, X., Zhang, G. & Li, B. Thermal transport in nanostructures. *AIP Advances* **2**, 041410 (2012).

41. Lepri, S., Livi, R. & Politi, A. Thermal conduction in classical low-dimensional lattices. *Phys. Rep.* **377**, 1–80 (2003).

42. Dubi, Y. & Di Ventra, M. Fourier's law: Insight from a simple derivation. *Phys. Rev. E* **79**, 042101 (2009).

43. Michel, M., Gemmer, J. & Mahler, G. Microscopic quantum mechanical foundation of fourier's law. *Int. J. Mod. Phys. B* **20**, 4855–4883 (2006).

44. Buchanan, M. Heated debate in different dimensions. *Nature Phys.* **1**, 71–71 (2005).

45. Li, Y., Liu, S., Li, N., Hnggi, P. & Li, B. 1D momentum-conserving systems: the conundrum of anomalous versus normal heat transport. *New J. Phys.* **17**, 043064 (2015).

46. Fermi, E., Pasta, J. & Ulam, S. Studies of the nonlinear problems i. *Los Alamos Sci. Lab. Rep. No. LA-1940* (1955).

47. Berman, G. P. & Izrailev, F. M. The Fermi-Pasta-Ulam problem: Fifty years of progress. *Chaos* **15**, 015104 (2005).

48. Gallavotti, G. *The Fermi-Pasta-Ulam problem: a status report*, vol. 728 of *Lecture Notes in Physics, Berlin Springer Verlag* (Springer, 2008).

49. Dhar, A. Heat transport in low-dimensional systems. *Adv. Phys.* **57**, 457–537 (2008).

50. Liu, S., Xu, X., Xie, R., Zhang, G. & Li, B. Anomalous heat conduction and anomalous diffusion in low dimensional nanoscale systems. *Eur. Phys. J. B* **85**, 1–20 (2012).

51. Casher, A. & Lebowitz, J. L. Heat flow in regular and disordered harmonic chains. *J. Math. Phys.* **12**, 1701–1711 (1971).

52. Bernardin, C. & Olla, S. Fouriers law for a microscopic model of heat conduction. *J. Stat. Phys.* **121**, 271–289 (2005).

53. Nakazawa, H. On the lattice thermal conduction. *Prog. Theor. Phys. Supplement* **45**, 231–262 (1970).

54. Dhar, A. Heat conduction in the disordered harmonic chain revisited. *Phys. Rev. Lett.* **86**, 5882 (2001).

55. Velizhanin, K. A., Chien, C.-C., Dubi, Y. & Zwolak, M. Driving denaturation: Nanoscale thermal transport as a probe of DNA melting. *Phys. Rev. E* **83**, 050906 (2011).

56. Segal, D., Nitzan, A. & Hanggi, P. Thermal conductance through molecular wires. *J. Chem. Phys.* **119**, 6840–6855 (2003).

57. Terraneo, M., Peyrard, M. & Casati, G. Controlling the energy flow in nonlinear lattices: A model for a thermal rectifier. *Phys. Rev. Lett.* **88**, 094302 (2002).

58. Kapitza, P. L. The study of heat transfer in helium ii. *J. Phys.(USSR)* **4**, 181–210 (1941).

59. Hänggi, P., Talkner, P. & Borkovec, M. Reaction-rate theory: Fifty years after Kramers. *Rev. Mod. Phys.* **62**, 251 (1990).

60. Melnikov, V. I. The kramers problem: Fifty years of development. *Phys. Rep.* **209**, 1–71 (1991).

61. Banerjee, S. & Dhar, A. Classical limit of master equation for a harmonic oscillator coupled to an oscillator bath with separable initial conditions. *Physical Review E-Statistical, Nonlinear and Soft Matter Physics* **73**, 067104_1–067104_3 (2006).

62. Luo, T. & Lloyd, J. R. Non-equilibrium molecular dynamics study of thermal energy transport in au–sam–au junctions. *Int. J. Heat Mass Transfer* **53**, 1–11 (2010).

63. Wang, Y., Ruan, X. & Roy, A. K. Two-temperature nonequilibrium molecular dynamics simulation of thermal transport across metal-nonmetal interfaces. *Phys. Rev. B* **85**, 205311 (2012).

64. Zhang, Y., Barnes, G. L., Yan, T. & Hase, W. L. Model non-equilibrium molecular dynamics simulations of heat transfer from a hot gold surface to an alkylthiolate self-assembled monolayer. *Phys. Chem. Chem. Phys.* **12**, 4435–4445 (2010).

65. Falat, T., Platek, B. & Felba, J. Non-equilibrium molecular dynamics simulation of heat transfer in carbon nanotubes - verification and model validation. In *Thermal, Mechanical and Multi-Physics Simulation and Experiments in Microelectronics and Microsystems (EuroSimE), 2011 12th International Conference on*, 1/5–5/5 (2011).

66. Wang, S.-C., Liang, X.-g., Xu, X.-H. & Ohara, T. Thermal conductivity of silicon nanowire by nonequilibrium molecular dynamics simulations. *J. Appl. Phys.* **105**, 014316 (2009).

67. Saha, S. K. & Shi, L. Molecular dynamics simulation of thermal transport at a nanometer scale constriction in silicon. *J. Appl. Phys.* **101** (2007).

68. Xu, Z. *et al.* Reversible hydrophobic to hydrophilic transition in graphene via water splitting induced by uv irradiation. *Scientific Reports* **4** (2014).

69. Mortazavi, B., Rajabpour, A., Ahzi, S., Rémond, Y. & Mehdi Vaez Allaei, S. Nitrogen doping and curvature effects on thermal conductivity of graphene: A non-equilibrium molecular dynamics study. *Solid State Commun.* **152**, 261–264 (2012).

70. Sahu, S., Di Ventra, M. & Zwolak, M. Dehydration as a universal mechanism for ion selectivity in graphene and other atomically thin pores. *arXiv preprint arXiv:1605.03134* (2016).

71. Sahu, S., Di Ventra, M. & Zwolak, M. Ion transport and dehydration in sub-nanoscale pores. *Biophysical Journal* **112**, 544a (2017).

72. Doyle, D. A. *et al.* The structure of the potassium channel: Molecular basis of K+ conduction and selectivity. *Science* **280**, 69 (1998).

73. Noskov, S. Y., Berneche, S. & Roux, B. Control of ion selectivity in potassium channels by electrostatic and dynamic properties of carbonyl ligands. *Nature* **431**, 830–834 (2004).

74. Noskov, S. Y. & Roux, B. Importance of hydration and dynamics on the selectivity of the KcsA and NaK channels. *J. Gen. Physiol.* **129**, 135–143 (2007).

75. Rasband, M. N. Ion channels and excitable cells. *Nature Education* **3**, 41 (2010).

76. Varma, S., Sabo, D. & Rempe, S. B. K+/Na+ selectivity in K channels and valinomycin: Over-coordination versus cavity-size constraints. *J. Mol. Biol.* **376**, 13–22 (2008).

77. Eisenberg, R. From structure to function in open ionic channels. *J. Membr. Biol.* **171**, 1–24 (1999).

78. Varma, S., Rogers, D. M., Pratt, L. R. & Rempe, S. B. Design principles for K+ selectivity in membrane transport. *J. Gen. Physiol* **137**, 479–488 (2011).

79. Zwolak, M., Lagerqvist, J. & Di Ventra, M. Quantized ionic conductance in nanopores. *Phys. Rev. Lett.* **103**, 128102 (2009).

80. Zwolak, M., Wilson, J. & Di Ventra, M. Dehydration and ionic conductance quantization in nanopores. *J. Phys.: Condens. Matter* **22**, 454126 (2010).

81. Joshi, R. *et al.* Precise and ultrafast molecular sieving through graphene oxide membranes. *Science* **343**, 752–754 (2014).

82. Sint, K., Wang, B. & Král, P. Selective ion passage through functionalized graphene nanopores. *J. Am. Chem. Soc.* **130**, 16448–16449 (2008).

83. Song, C. & Corry, B. Intrinsic ion selectivity of narrow hydrophobic pores. *J. Phys. Chem. B* **113**, 7642–7649 (2009).

84. Richards, L. A., Schäfer, A. I., Richards, B. S. & Corry, B. The importance of dehydration in determining ion transport in narrow pores. *Small* **8**, 1701–1709 (2012).

85. Richards, L. A., Schäfer, A. I., Richards, B. S. & Corry, B. Quantifying barriers to monovalent anion transport in narrow non-polar pores. *Phys. Chem. Chem. Phys.* **14**, 11633–11638 (2012).

86. Gouaux, E. & MacKinnon, R. Principles of Selective Ion Transport in Channels and Pumps. *Science* **310**, 1461–1465 (2005).

87. Rollings, R. C., Kuan, A. T. & Golovchenko, J. A. Ion selectivity of graphene nanopores. *Nat. Commun.* **7** (2016).

88. Phillips, J. C. *et al.* Scalable molecular dynamics with namd. *Journal of computational chemistry* **26**, 1781–1802 (2005).

89. Martyna, G. J., Tobias, D. J. & Klein, M. L. Constant pressure molecular dynamics algorithms. *J. Chem. Phys.* **101**, 4177 (1994).

90. Grossfield, A. & Zuckerman, D. M. Quantifying uncertainty and sampling quality in biomolecular simulations. *Annu. Rep. Comput. Chem.* **5**, 23–48 (2009).

91. Aksimentiev, A. & Schulten, K. Imaging α-hemolysin with molecular dynamics: ionic conductance, osmotic permeability, and the electrostatic potential map. *Biophys. J.* **88**, 3745–3761 (2005).

92. Ahn, S. & Fessler, J. A. Standard errors of mean, variance, and standard deviation estimators. *University of Michigan: EECS Department* (2003).

93. Bhattacharya, S. *et al.* Rectification of the Current in -Hemolysin Pore Depends on the Cation Type: The Alkali Series Probed by Molecular Dynamics Simulations and Experiments. *The Journal of Physical Chemistry C* **115**, 4255–4264 (2011).

94. Hall, J. E. Access reistance of a small circular pore. *J. Gen. Physiol.* **66**, 531–532 (1975).

95. Sathe, C., Zou, X., Leburton, J.-P. & Schulten, K. Computational investigation of DNA detection using graphene nanopores. *ACS Nano* **5**, 8842–8851 (2011).

96. Wells, D. B., Belkin, M., Comer, J. & Aksimentiev, A. Assessing graphene nanopores for sequencing DNA. *Nano Lett.* **12**, 4117–4123 (2012).

97. Akeson, M., Branton, D., Kasianowicz, J. J., Brandin, E. & Deamer, D. W. Microsecond time-scale discrimination among polycytidylic acid, polyadenylic acid, and polyuridylic acid as homopolymers or as segments within single RNA molecules. *Biophys. J.* **77**, 3227 (1999).

98. Deamer, D. W. & Akeson, M. Nanopores and nucleic acids: prospects for ultrarapid sequencing. *Trends Biotechnol.* **18**, 147 (2000).

99. Vercoutere, W. *et al.* Rapid discrimination among individual DNA hairpin molecules at single-nucleotide resolution using an ion channel. *Nat. Biotechnol.* **19**, 248 (2001).

100. Deamer, D. W. & Branton, D. Characterization of nucleic acids by nanopore analysis. *Acc. Chem. Res.* **35**, 817 (2002).

101. Vercoutere, W. & Akeson, M. Biosensors for DNA sequence detection. *Curr. Opin. Chem. Biol.* **6**, 816 (2002).

102. Vercoutere, W. A. *et al.* Discrimination among individual Watson-Crick base pairs at the termini of single DNA hairpin molecules. *Nucleic Acids Res.* **31**, 1311 (2003).

103. Winters-Hilt, S. *et al.* Highly accurate classification of Watson-Crick basepairs on termini of single DNA molecules. *Biophys. J.* **84**, 967 (2003).

104. Zwolak, M. & Di Ventra, M. Electronic signature of DNA nucleotides via transverse transport. *Nano Lett.* **5**, 421 (2005).

105. Lagerqvist, J., Zwolak, M. & DiVentra, M. Fast DNA sequencing via transverse electronic transport. *Nano Lett.* **6**, 779 (2006).

106. Lagerqvist, J., Zwolak, M. & Di Ventra, M. Comment on "Characterization of the tunneling conductance across DNA bases". *Phys. Rev. E* **76**, 013901 (2007).

107. Zwolak, M. & Di Ventra, M. Colloquium: Physical approaches to DNA sequencing and detection. *Rev. Mod. Phys.* **80**, 141 (2008).

108. Krems, M., Zwolak, M., Pershin, Y. V. & Di Ventra, M. Effect of noise on DNA sequencing via transverse electronic transport. *Biophys. J.* **97**, 1990 (2009).

109. Tsutsui, M., Taniguchi, M., Yokota, K. & Kawai, T. Identifying single nucleotides by tunnelling current. *Nature Nanotech.* **5**, 286 (2010).

110. Chang, S. *et al.* Electronic signatures of all four DNA nucleosides in a tunneling gap. *Nano Lett.* **10**, 1070 (2010).

111. Sahu, S. & Zwolak, M. Ionic selectivity and filtration from fragmented dehydration in multilayer graphene nanopores. *arXiv preprint arXiv:1705.04538* (2017).

112. Hille, B. *Ion channels of excitable membranes*, vol. 507 (Sinauer Sunderland, MA, 2001).

113. Abraham, J. *et al.* Tunable sieving of ions using graphene oxide membranes. *Nat. Nanotechnol.* (2017).

114. Balijepalli, A. *et al.* Quantifying short-lived events in multi-state ionic channel measurements. *ACS Nano* **8**, 1547 (2014).

115. Cohen-Tanugi, D., Lin, L.-C. & Grossman, J. C. Multilayer Nanoporous Graphene Membranes for Water Desalination. *Nano Lett.* **16**, 1027–1033 (2016).

116. Clarke, J. *et al.* Continuous base identification for single-molecule nanopore DNA sequencing. *Nat. Nanotechnol.* **4**, 265–270 (2009).

117. Lee, K. P., Arnot, T. C. & Mattia, D. A review of reverse osmosis membrane materials for desalinationDevelopment to date and future potential. *J. Membr. Sci.* **370**, 1–22 (2011).

118. Karan, S., Jiang, Z. & Livingston, A. G. Sub10 nm polyamide nanofilms with ultrafast solvent transport for molecular separation. *Science* **348**, 1347–1351 (2015).

119. Walker, M. I. *et al.* Extrinsic Cation Selectivity of 2D Membranes. *ACS Nano* **11**, 1340–1346 (2017).

120. Surwade, S. P. *et al.* Water desalination using nanoporous single-layer graphene. *Nat. Nanotechnol.* **10**, 459–464 (2015).

121. Feng, J. *et al.* Observation of ionic Coulomb blockade in nanopores. *Nat. Mater.* **15**, 850–855 (2016).

122. Rodríguez-Manzo, J. A., Puster, M., Nicolaï, A., Meunier, V. & Drndić, M. DNA Translocation in Nanometer Thick Silicon Nanopores. *ACS Nano* **9**, 6555–6564 (2015).

123. Humphrey, W., Dalke, A. & Schulten, K. VMD – Visual Molecular Dynamics. *J. Mol. Graphics* **14**, 33–38 (1996).

124. Sahu, S. & Zwolak, M. Access resistance in ion transport through graphene nanopores. *Bulletin of the American Physical Society* **62** (2017).

125. Panday, N. & He, J. Scanning Ion Conductance Microscopy for Single Cell Imaging and Analysis. *Adv. Sci. Eng. Med.* **7**, 1058–1065 (2015).

126. Heerema, S. J. & Dekker, C. Graphene nanodevices for DNA sequencing. *Nat Nano* **11**, 127–136 (2016).

127. Garaj, S., Liu, S., Golovchenko, J. A. & Branton, D. Molecule-hugging graphene nanopores. *Proc. Natl. Acad. Sci.* **110**, 12192–12196 (2013).

128. Hu, G., Mao, M. & Ghosal, S. Ion transport through a graphene nanopore. *Nanotechnology* **23**, 395501 (2012).

129. Maxwell, J. C. *A treatise on electricity and magnetism*, vol. 1 (Dover Publications, 1954).

130. Holm, R. *The contact resistance. General theory* (Springer, 1958).

131. Newman, J. Resistance for Flow of Current to a Disk. *J Electrochem Soc* **113**, 501–502 (1966).

132. Tsutsui, M. *et al.* Single-Nanoparticle Detection Using a Low-Aspect-Ratio Pore. *ACS Nano* **6**, 3499–3505 (2012).

133. Panday, N. *et al.* Simultaneous Ionic Current and Potential Detection of Nanoparticles by a Multifunctional Nanopipette. *ACS Nano* **10**, 11237–11248 (2016).

134. Braunovic, M., Myshkin, N. K. & Konchits, V. V. *Electrical contacts: fundamentals, applications and technology* (CRC press, 2006).

135. Grahame, D. C. The electrical double layer and the theory of electrocapillarity. *Chem. Rev.* **41**, 441–501 (1947).

136. Gumbart, J., Khalili-Araghi, F., Sotomayor, M. & Roux, B. Constant electric field simulations of the membrane potential illustrated with simple systems. *Biochimica et Biophysica Acta (BBA) - Biomembranes* **1818**, 294 – 302 (2012).

137. Jensen, M. Ø., Jogini, V., Eastwood, M. P. & Shaw, D. E. Atomic-level simulation of currentvoltage relationships in single-file ion channels. *J. Gen. Phsiol.* **141**, 619–632 (2013).

138. Corry, B., Kuyucak, S. & Chung, S. H. Invalidity of continuum theories of electrolytes in nanopores. *Chem. Phys. Lett.* **320**, 35–41 (2000).

139. Corry, B., Kuyucak, S. & Chung, S.-H. Tests of Continuum Theories as Models of Ion Channels. II. PoissonNernstPlanck Theory versus Brownian Dynamics. *Biophys. J.* **78**, 2364–2381 (2000).

140. Fuliski, A., Kosiska, I. D. & Siwy, Z. On the validity of continuous modelling of ion transport through nanochannels. *Europhys. Lett.* **67**, 683–690 (2004).

141. Peter, C. & Hummer, G. Ion Transport through Membrane-Spanning Nanopores Studied by Molecular Dynamics Simulations and Continuum Electrostatics Calculations. *Biophys. J.* **89**, 2222–2234 (2005).

142. Humphrey, W., Dalke, A. & Schulten, K. VMD: Visual molecular dynamics. *J. Mol. Graphics* **14**, 33–38 (1996).

143. Guo, H. *et al.* Enabling photoemission electron microscopy in liquids via graphene-capped microchannel arrays. *Nano Letters* **17**, 1034–1041 (2017).

144. Siegbahn, H. & Siegbahn, K. Esca applied to liquids. *Journal of Electron Spectroscopy and Related Phenomena* **2**, 319–325 (1973).

145. Salmeron, M. & Schlgl, R. Ambient pressure photoelectron spectroscopy: A new tool for surface science and nanotechnology. *Surface Science Reports* **63**, 169–199 (2008).

146. Ghosal, S. *et al.* Electron spectroscopy of aqueous solution interfaces reveals surface enhancement of halides. *Science* **307**, 563–566 (2005).

147. Zhang, C. *et al.* Measuring fundamental properties in operating solid oxide electrochemical cells by using in situ x-ray photoelectron spectroscopy. *Nature materials* **9**, 944–949 (2010).

148. Favaro, M. *et al.* Unravelling the electrochemical double layer by direct probing of the solid/liquid interface. *Nature Communications* **7**, 12695 (2016).

149. Tao, F. *et al.* Break-up of stepped platinum catalyst surfaces by high co coverage. *Science* **327**, 850–853 (2010).

150. Kirz, J., Jacobsen, C. & Howells, M. Soft x-ray microscopes and their biological applications. *Quarterly reviews of biophysics* **28**, 33–130 (1995).

151. Ogletree, D. F. *et al.* A differentially pumped electrostatic lens system for photoemission studies in the millibar range. *Review of Scientific Instruments* **73**, 3872–3877 (2002).

152. Winter, B. & Faubel, M. Photoemission from liquid aqueous solutions. *Chemical reviews* **106**, 1176–1211 (2006).

153. Starr, D. E., Wong, E. K., Worsnop, D. R., Wilson, K. R. & Bluhm, H. A combined droplet train and ambient pressure photoemission spectrometer for the investigation of liquid/vapor interfaces. *Physical Chemistry Chemical Physics* **10**, 3093–3098 (2008).

154. Crumlin, E. J. *et al.* X-ray spectroscopy of energy materials under in situ/operando conditions. *Journal of Electron Spectroscopy and Related Phenomena* **200**, 264–273 (2015).

155. Siegbahn, H. Electron spectroscopy for chemical analysis of liquids and solutions. *The Journal of Physical Chemistry* **89**, 897–909 (1985).

156. Kolmakov, A. *et al.* Graphene oxide windows for in situ environmental cell photoelectron spectroscopy. *Nature nanotechnology* **6**, 651–657 (2011).

157. Kraus, J. *et al.* Photoelectron spectroscopy of wet and gaseous samples through graphene membranes. *Nanoscale* **6**, 14394–14403 (2014).

158. VelascoVelez, J. J. *et al.* Photoelectron spectroscopy at the grapheneliquid interface reveals the electronic structure of an electrodeposited cobalt/graphene electrocatalyst. *Angewandte Chemie International Edition* **54**, 14554–14558 (2015).

159. Weatherup, R. S., Eren, B., Hao, Y., Bluhm, H. & Salmeron, M. B. Graphene membranes for atmospheric pressure photoelectron spectroscopy. *The journal of physical chemistry letters* **7**, 1622–1627 (2016).

160. Velasco-Vlez, J. *et al.* Atmospheric pressure x-ray photoelectron spectroscopy apparatus: Bridging the pressure gap. *Review of Scientific Instruments* **87**, 053121 (2016).

161. Kolmakov, A., Gregoratti, L., Kiskinova, M. & Gnther, S. Recent approaches for bridging the pressure gap in photoelectron microspectroscopy. *Topics in Catalysis* **59**, 448–468 (2016).

162. Bauer, E. A brief history of peem. *Journal of Electron Spectroscopy and Related Phenomena* **185**, 314–322 (2012).

163. Spiel, C. *et al.* Catalytic co oxidation on individual (110) domains of a polycrystalline pt foil: local reaction kinetics by peem. *Catalysis Letters* **141**, 625–632 (2011).

164. De Stasio, G. *et al.* Feasibility tests of transmission x-ray photoelectron emission microscopy of wet samples. *Review of Scientific Instruments* **71**, 11–14 (2000).

165. Frazer, B., Gilbert, B. & De Stasio, G. X-ray absorption microscopy of aqueous samples. *Review of scientific instruments* **73**, 1373–1375 (2002).

166. Ballarotto, V. W., Breban, M., Siegrist, K., Phaneuf, R. J. & Williams, E. D. Photoelectron emission microscopy of ultrathin oxide covered devices. *Journal of Vacuum Science & Technology B* **20**, 2514–2518 (2002).

167. Zamborlini, G. *et al.* Nanobubbles at gpa pressure under graphene. *Nano letters* **15**, 6162–6169 (2015).

168. Frazer, B. H., Gilbert, B., Sonderegger, B. R. & De Stasio, G. The probing depth of total electron yield in the sub-kev range: Tey-xas and x-peem. *Surface science* **537**, 161–167 (2003).

169. Vinson, J., Rehr, J., Kas, J. & Shirley, E. Bethe-salpeter equation calculations of core excitation spectra. *Physical Review B* **83**, 115106 (2011).

170. Gilmore, K. *et al.* Efficient implementation of core-excitation bethesalpeter equation calculations. *Computer Physics Communications* **197**, 109–117 (2015).

171. Schravendijk, P., van der Vegt, N., Delle Site, L. & Kremer, K. Dualscale modeling of benzene adsorption onto ni (111) and au (111) surfaces in explicit water. *ChemPhysChem* **6**, 1866–1871 (2005).

172. Shelley, J., Patey, G., Brard, D. & Torrie, G. Modeling and structure of mercury-water interfaces. *The Journal of chemical physics* **107**, 2122–2141 (1997).

173. Kohlmeyer, A., Witschel, W. & Spohr, E. Molecular dynamics simulations of water/metal and water/vacuum interfaces with a polarizable water model. *Chemical physics* **213**, 211–216 (1996).

174. Luzar, A. Resolving the hydrogen bond dynamics conundrum. *The Journal of Chemical Physics* **113**, 10663–10675 (2000).

175. Perdew, J. P. & Wang, Y. Pair-distribution function and its coupling-constant average for the spin-polarized electron gas. *Physical Review B* **46**, 12947 (1992).

176. Giannozzi, P. *et al.* Quantum espresso: a modular and open-source software project for quantum simulations of materials. *Journal of physics: Condensed matter* **21**, 395502 (2009).

177. Prendergast, D. & Louie, S. G. Bloch-state-based interpolation: An efficient generalization of the shirley approach to interpolating electronic structure. *Physical Review B* **80**, 235126 (2009).

178. Shirley, E. L. Optimal basis sets for detailed brillouin-zone integrations. *Physical Review B* **54**, 16464 (1996).

179. Shirley, E. L. Local screening of a core hole: A real-space approach applied to hafnium oxide. *Ultramicroscopy* **106**, 986–993 (2006).

180. Tinone, M. C. *et al.* Site specific photochemical reaction of pmma and related polymers by inner shell electron excitation. *Journal of electron spectroscopy and related phenomena* **80**, 117–120 (1996).

181. Bluhm, H., Ogletree, D. F., Fadley, C. S., Hussain, Z. & Salmeron, M. The premelting of ice studied with photoelectron spectroscopy. *Journal of Physics: Condensed Matter* **14**, L227 (2002).

182. Lin, Y.-C. *et al.* Graphene annealing: how clean can it be? *Nano letters* **12**, 414–419 (2011).

183. Nilsson, A. *et al.* X-ray absorption spectroscopy and x-ray raman scattering of water and ice; an experimental view. *Journal of Electron Spectroscopy and Related Phenomena* **177**, 99–129 (2010).

184. Fransson, T. *et al.* X-ray and electron spectroscopy of water. *Chemical reviews* (2016).

185. Wernet, P. *et al.* The structure of the first coordination shell in liquid water. *Science* **304**, 995–999 (2004).

186. Frank, L., Mikmekov, E., Mllerov, I. & Lejeune, M. Counting graphene layers with very slow electrons. *Applied Physics Letters* **106**, 013117 (2015).

187. Velasco-Velez, J.-J. *et al.* The structure of interfacial water on gold electrodes studied by x-ray absorption spectroscopy. *Science* **346**, 831–834 (2014).

188. Brünger, A., Brooks, C. L. & Karplus, M. Stochastic boundary conditions for molecular dynamics simulations of st2 water. *Chemical physics letters* **105**, 495–500 (1984).

APPENDICES

A
Thermal Transport

A1 Dimensional analysis of the uniform harmonic model

The complete list of parameters of the uniform harmonic model introduced in main article is: m, D, K, γ, k_BT_L, k_BT_R, N, N_r. We take m, K and $k_B\Delta T = k_B(T_L - T_R)$ as fundamental units to make all the other parameters dimensionless. Then, the independent dimensionless parameters of the model are

$$\frac{D}{K},\ \frac{\gamma}{\sqrt{mK}},\ \frac{T_L + T_R}{\Delta T},\ N \text{ and } N_r. \tag{A.1}$$

Using these dimensionless parameters, the *exact* expression for the heat current through the lattice can be written as

$$\frac{J}{k_B\Delta T}\sqrt{\frac{m}{K}} = C\left(\frac{D}{K}, \frac{\gamma}{\sqrt{mK}}, \frac{T_L + T_R}{\Delta T}, N, N_r\right), \tag{A.2}$$

where C is a dimensionless function of five dimensionless arguments. This very general expression can be simplified by (i) taking $N \to \infty$ (see inset in Fig. 3.2) and by (ii) exploiting the fact that the heat current in such a model is proportional to ΔT [see Eq. (A.17) and the related discussion], then the function C cannot depend on T_L and T_R. These considerations result in

$$\frac{J}{k_B\Delta T}\sqrt{\frac{m}{K}} = C\left(\frac{D}{K}, \frac{\gamma}{\sqrt{mK}}, N_r\right), \tag{A.3}$$

where C is now a dimensionless function of just three dimensionless arguments. The expression for heat conductance of the 1D uniform harmonic model considered in this work can then be written in the limit of $N \to \infty$ as

$$\sigma = k_B\sqrt{\frac{K}{m}}C\left(\frac{D}{K}, \frac{\gamma}{\sqrt{mK}}, N_r\right). \tag{A.4}$$

A2 Numerical solution of Langevin equations of motion

The Langevin equations of motion for a lattice of harmonic oscillators, given by the Hamiltonian

$$H = \frac{1}{2}\mathbf{p}^{\intercal}\mathbf{M}^{-1}\mathbf{p} + \frac{1}{2}\mathbf{x}^{\intercal}\mathbf{K}\mathbf{x}, \tag{A.5}$$

are a system of first-order linear differential equations

$$\begin{aligned} \dot{x}_n &= p_n/m_n, \\ \dot{p}_n + \sum_{m=1}^{N} K_{nm}x_m + \gamma_n p_n/m_n &= \eta_n(t), \end{aligned} \tag{A.6}$$

where the mass can potentially be site-dependent in order to, e.g., examine mass disorder as in Disordered Harmonic Lattice discussed in main article. The matrix $\mathbf{K}$ contains the interaction potentials and $[\mathbf{M}]_{nm} = \delta_{nm}m_n$ is a diagonal matrix of the masses. These equations of motion can be expressed as

$$\frac{d}{dt}|q(t)\rangle + \mathbf{G}|q(t)\rangle = |\eta(t)\rangle, \tag{A.7}$$

where

$$|q\rangle \Rightarrow \begin{pmatrix} \vec{x} \\ \vec{p} \end{pmatrix}. \tag{A.8}$$

The non-symmetric matrix $\mathbf{G}$ is given by

$$\mathbf{G} = \begin{pmatrix} \mathbf{0} & -\mathbf{M}^{-1} \\ \mathbf{K} & \mathbf{\Gamma}\mathbf{M}^{-1} \end{pmatrix}, \tag{A.9}$$

where $\mathbf{\Gamma}$ is a diagonal matrix of the couplings to the Langevin reservoirs (and $\mathrm{tr}|\mathbf{\Gamma}| = 2\Gamma$, where Γ is the cumulative friction coefficient).

The formal solution of Eq. (A.7) is

$$|q(t)\rangle = \int_{t_0}^{t} dt'\, e^{-\mathbf{G}(t-t')}|\eta(t')\rangle. \tag{A.10}$$

An important class of observables can be expressed as an average of a quadratic form of $|q(t)\rangle$ over the statistical ensemble. For example, the heat current flowing from site n to site $n+1$ can be written as a statistical average of

$$J_n = -\frac{K_{n+1,n}}{m_{n+1}} p_{n+1} x_n. \tag{A.11}$$

An observable of this class can be represented by an operator $\mathbf{O}$ so that

$$\begin{aligned} O(t) &= \langle q(t)|\mathbf{O}|q(t)\rangle \\ &= \int_{t_0}^{t} dt' \int_{t_0}^{t} dt'' \, \langle \eta(t')|e^{-\mathbf{G}^\dagger(t-t')}\mathbf{O}e^{-\mathbf{G}(t-t'')}|\eta(t'')\rangle. \end{aligned} \tag{A.12}$$

Averaging over the statistical ensemble and using Eq. 3.3 from Methods section of main article for the auto-correlation function of the random forces, one obtains

$$O(t) = \int_{t_0}^{t} dt' \, \mathrm{Tr}\left[e^{-\mathbf{G}^\dagger(t-t')}\mathbf{O}e^{-\mathbf{G}(t-t')}\mathbf{F}\right], \tag{A.13}$$

where $\mathbf{F}$ is a diagonal matrix with its only non-zero elements given by

$$F_{N+n,N+n} = 2\gamma_n k_B T_n, \;\; n = 1, 2, ..., N. \tag{A.14}$$

The spectral decomposition of the particular class of non-symmetric operators $\mathbf{G}$ above necessarily includes left and right eigenvectors, i.e., $\mathbf{G} = \sum_k \lambda_k |k_R\rangle\langle k_L|$, where the components of right (column) and left (row) eigenvectors are denoted by $[|k_R\rangle]_n = v^R_{n,k}$ and $[\langle k_L|]_n = \left(v^L_{n,k}\right)^*$, respectively. The orthonormality condition is $\langle k_L|l_R\rangle = \sum_{n=1}^{2N}\left(v^L_{n,k}\right)^* v^R_{n,l} = \delta_{kl}$. The spectral decomposition of $\mathbf{G}^\dagger$ is given by $\mathbf{G}^\dagger = \sum_k \lambda_k^* |k_L\rangle\langle k_R|$, where $|k_L\rangle = \langle k_L|^\dagger$ and $\langle k_R| = |k_R\rangle^\dagger$.

Substituting these spectral decompositions into Eq. (A.13), setting $t_0 \to -\infty$ to find the steady-state value of the observable, and integrating, we obtain

$$O = \sum_{k,l=1}^{2N} \frac{\langle l_R|\mathbf{O}|k_R\rangle\langle k_L|\mathbf{F}|l_L\rangle}{\lambda_k + \lambda_l^*}. \tag{A.15}$$

This equation allows one to draw very general conclusions regarding the dependence of the observable O on temperature without the need to explicitly specify **G** and **O**. Since operators **O** (e.g., heat current) and **G** do not typically depend on temperature, and the operator **F** in Eq. (A.14) is strictly linear with respect to temperature, O is then a linear form of $T_1, T_2, ..., T_N$. Specifically, since in the harmonic lattice case we examine there is only two independent temperatures, T_L and T_R, O is necessary a linear form of T_L and T_R, i.e.,

$$O(T_L, T_R) = \alpha_L T_L + \alpha_R T_R, \tag{A.16}$$

where α_L and α_R are coefficients that depend only on specific parameters of the system and nature of operator **O**, but not temperature. For example, since the heat current has to vanish at thermodynamic equilibrium, we must have $\alpha_L = -\alpha_R$ and, therefore,

$$J \propto T_L - T_R. \tag{A.17}$$

That is, the heat conductance does not depend on temperatures T_L or T_R at all. These considerations do not lead to the same conclusion in the case of anharmonic lattices, as illustrated in Fig. 5(b).

A3 Heat current in 1D harmonic lattices

To use Eq. (A.15) to evaluate the heat current in the lattice of harmonic oscillators, one needs to construct operators **G** and **O**. Below we explicitly construct these matrices and derive an expression for the heat current.

The system under consideration is a lattice of harmonic oscillators with only nearest neighbor coupling, which yields a matrix **K** in Eq. (A.5) that is sparse. For an oscillator with index n somewhere inside the lattice (i.e., $1 < n < N$), the corresponding n^{th} row of the matrix has only three non-zero components $(K_{n,n-1}, K_{n,n}, K_{n,n+1}) = (-K, D + 2K, -K)$, where K and D are parameters in the Hamiltonian. The end sites, $n = 1$ and $n = N$, are assumed to be coupled to "hard walls", i.e., to implicit oscillators with indices $n = 0$ and $n = N + 1$, respectively, whose coordinates are kept zero. This results in

only two non-zero matrix elements in the very first and the very last rows of matrix $\mathbf{K}$: $(K_{1,1}K_{1,2}) = (D + 2K, -K)$ and $(K_{N,N-1}K_{N,N}) = (-K, D + 2K)$.

According to Eq. (A.11), the operator $\mathbf{J}_n$ corresponding to the heat current from site n to site $n + 1$ has only a single non-zero element

$$[\mathbf{J}_n]_{N+n+1,n} = \frac{K}{m_{n+1}}. \tag{A.18}$$

Substituting this expression, together with Eq. (A.14) and the eigenvectors of $\mathbf{G}$ and $\mathbf{G}^\dagger$, into Eq. (A.15) gives

$$J_n = \frac{2k_B K}{m_{n+1}} \sum_{k,l=1}^{2N} \left[\frac{\left(v^R_{N+n+1,l}\right)^* v^R_{n,k}}{\lambda_k + \lambda_l^*} \times \sum_{m=1}^{N} \gamma_m T_m \left(v^L_{N+m,k}\right)^* v^L_{N+m,l} \right]. \tag{A.19}$$

A4 Heat current in the small γ regime

The most convenient way to analyze the small γ dynamics of the 1D lattice is to perform a perturbation expansion of eigenvalues and eigenvectors of operator $\mathbf{G}$ with respect to γ. $\mathbf{G}$ is at most linear with respect to γ and can be represented as $\mathbf{G} = \mathbf{G}_0 + \gamma\mathbf{G}_1$, where $\mathbf{G}_{0,1}$ are independent of γ. The zeroth-order eigenvalues and eigenvectors of $\mathbf{G}$ are then the eigenvalues and eigenvectors of $\mathbf{G}_0$,

$$\mathbf{G}_0 = \begin{pmatrix} \mathbf{0} & -\mathbf{M}^{-1} \\ \mathbf{K} & \mathbf{0} \end{pmatrix}. \tag{A.20}$$

The solutions – normal modes of lattice vibrations with no friction – can be found in the standard way, first by scaling ("mass-weighting") by $\mathbf{S} = \mathrm{diag}(\mathbf{M}^{1/2}, \mathbf{M}^{-1/2})$,

$$\mathbf{S}\mathbf{G}_0\mathbf{S}^{-1} = \begin{pmatrix} \mathbf{0} & -\mathbf{I} \\ \mathbf{M}^{-\frac{1}{2}}\mathbf{K}\mathbf{M}^{-1/2} & \mathbf{0} \end{pmatrix} \tag{A.21}$$

and then diagonalizing the mass-weighted coupling $\mathbf{M}^{-1/2}\mathbf{K}\mathbf{M}^{-1/2}$ via an orthogonal transformation $\mathbf{T}$. The normal modes of the lattice are

$$x_n^k(t) = u_n^k e^{\pm i\omega_k t}, \tag{A.22}$$

where $u_n^k = \left[\mathbf{M}^{-1/2}\mathbf{T}\right]_{nk}$ are the real-valued polarization vectors of the normal modes and $n, k = 1, \ldots, N$ enumerate the lattice sites and modes, respectively.

The eigenvalues and *right* eigenvectors (hence denoted with R below) of $\mathbf{G}_0$ can be readily constructed from these and they come in pairs. The unnormalized "positive frequency" solutions are

$$\begin{aligned} \lambda_k^0 &= i\omega_k, \\ v_{n,k}^{0,R} &\propto u_n^k, \\ v_{N+n,k}^{0,R} &\propto -i\omega_k m_n u_n^k, \end{aligned} \tag{A.23}$$

for $k = 1, \ldots, N$ and $n = 1, \ldots, N$. The unnormalized "negative frequency" solutions are

$$\begin{aligned} \lambda_k^0 &= -i\omega_k, \\ v_{n,k}^{0,R} &\propto u_n^k, \\ v_{N+n,k}^{0,R} &\propto i\omega_k m_n u_n^k, \end{aligned} \tag{A.24}$$

for $k = N+1, \ldots, 2N$, $n = 1, \ldots, N$, and "extending" $\omega_k = \omega_{k-N}$ and $u_n^k = u_n^{k-N}$ for $k > N$. We have ordered the solution so that when the positive frequency solution takes on the label k, the negative frequency solution takes on the label $k + N$. The last two lines of each of these solutions reflect the simple relationship between momenta and the time derivative of coordinates, the first line in Eq. (A.6).

The left eigenvectors can be found in a similar way, essentially the position and momenta change roles including how they are scaled by mass. With the convention that

$[\langle k_L|]_n = \left(v^L_{n,k}\right)^*$, the unnormalized "positive frequency" solutions are

$$\begin{aligned} \lambda^0_k &= i\omega_k, \\ v^{0,L}_{n,k} &\propto i\omega_k m_n u^k_n, \\ v^{0,L}_{N+n,k} &\propto u^k_n, \end{aligned} \tag{A.25}$$

for $k = 1, \ldots, N$ and $n = 1, \ldots, N$. The unnormalized "negative frequency" solutions are

$$\begin{aligned} \lambda^0_k &= -i\omega_k, \\ v^{0,L}_{n,k} &\propto -i\omega_k m_n u^k_n, \\ v^{0,L}_{N+n,k} &\propto u^k_n, \end{aligned} \tag{A.26}$$

for $k = N+1, \ldots, 2N$, $n = 1, \ldots, N$, and the same "extension" for $k > N$. The left and right eigenvectors clearly obey the right orthogonality relationship, but for each k have norm $\mp 2i\omega_k$ for "positive" and "negative" frequencies, respectively.

The first-order perturbative correction to the eigenvalues of $\mathbf{G}_0$ can be found in the usual manner, i.e.,

$$\lambda^1_k = \gamma \langle k^0_L | \mathbf{G}_1 | k^0_R \rangle. \tag{A.27}$$

Using this expression, we can now expand the current. To do so, we will make use of Eq. (A.15). The matrix element $\langle k_L|\mathbf{F}|l_L\rangle$ is linear with respect to γ at small γ, i.e., putting in the normalized zeroth order states $\langle k^0_L|\mathbf{F}|l^0_L\rangle = \sum_n 2\gamma_n k_B T_n u^k_n u^l_n / \sqrt{4\omega_k \omega_l}$. Thus, we can focus on the quantity

$$\frac{\langle l_R|\mathbf{J}_n|k_R\rangle}{\lambda_k + \lambda^*_l} \tag{A.28}$$

and show that it is zeroth order with respect to γ. We separate the summation in Eq. (A.15) into the off-diagonal ($k \neq l$) and diagonal ($k = l$) contributions. Assuming no degeneracy, the former is nonzero and well-behaved when zeroth-order eigenvalues

and eigenvectors are used since the denominator in Eq. (A.15) does not vanish at $k \neq l$. The off-diagonal contribution is thus proportional to γ at small γ.

The diagonal contribution has a vanishing denominator as γ approaches zero, i.e., λ_k^0 is pure imaginary which gives $\lambda_k + \lambda_k^* = 0 + \sum_n \gamma_n (u_n^k)^2 + \mathcal{O}(\gamma^2)$. Performing the whole sum, however, we can pair the "positive" and "negative" frequencies:

$$\sum_{k=1}^{N} \left(\langle k_R | \mathbf{J}_n | k_R \rangle + \langle (k+N)_R | \mathbf{J}_n | (k+N)_R \rangle \right) \frac{\langle k_L^0 | \mathbf{F} | k_L^0 \rangle}{\lambda_k + \lambda_k^*} \tag{A.29}$$

where the last factor is the same for both "positive" and "negative" frequencies. The term in parenthesis gives

$$\left(\frac{i m_{n+1} u_{n+1}^k u_n^k}{2} + \frac{-i m_{n+1} u_{n+1}^k u_n^k}{2} + \mathcal{O}(\gamma) \right) = 0 + \mathcal{O}(\gamma) \tag{A.30}$$

Thus, the sum over "positive" and "negative" frequencies gives a contribution that is of order γ. Therefore, the current for small γ is $J \propto \gamma$.

A5 Heat current in the large γ regime

The current in the large γ regime can also be calculated perturbatively in powers of $1/\gamma$. We consider only single sites at each end connected to Langevin reservoirs, as any additional sites in the extended reservoir are decoupled from the lattice by higher orders in $1/\gamma$. Now consider the matrix $\gamma \mathbf{G}_1 + \mathbf{G}_0$, where $\mathbf{G}_0$ is the perturbation. The expansion is complicated by the fact that the "bare" matrix

$$\gamma \mathbf{G}_1 = \begin{pmatrix} \mathbf{0} & \mathbf{0} \\ \mathbf{0} & \mathbf{\Gamma M}^{-1} \end{pmatrix} \tag{A.31}$$

is highly degenerate, with $2N-2$ zero eigenvalues and 2 non-zero eigenvalues. The latter two are γ/m_1 and γ/m_N, which may have an (unimportant) degeneracy, and we can take two of the zeroth order right (left) eigenvectors to be $|N+1\rangle$ and $|2N\rangle$ ($\langle N+1|$ and $\langle 2N|$).

The degenerate space is spanned by the states $|n\rangle$ with $n = 1, \ldots, N$ and $|N+m\rangle$

$\downarrow k \neq l \rightarrow$	$l \in \mathcal{B}_{-1}$	$l \in \mathcal{B}_0$	$l \in \mathcal{B}_1$
$l \in \mathcal{B}_{-1}$	$\frac{1}{\gamma};\frac{1}{\gamma};\frac{1}{\gamma}$	$1;\frac{1}{\gamma};1$	$\frac{1}{\gamma};1;\gamma$
$l \in \mathcal{B}_0$	$1;\frac{1}{\gamma};1$	$1;\frac{1}{\gamma};1$	$1;1;\gamma$
$l \in \mathcal{B}_1$	$\frac{1}{\gamma};1;\gamma$	$1;1;\gamma$	$\frac{1}{\gamma};0;\gamma$

TABLE 0.1: Order of the different factors in the current contribution, Eq. A.15, when $k \neq l$. Note that cross terms between $\mathcal{B}_1$ and $\mathcal{B}_1$ are identically zero given our choice of zeroth order eigenvectors.

with $m = 2, \ldots, (N-1)$. The degeneracy is lifted in the normal way: Let $\mathbf{P}_0$ project onto this subspace and diagonalize $\mathbf{P}_0\mathbf{G}_0\mathbf{P}_0$. This matrix has $2N-4$ eigenvectors with non-zero eigenvalues. The right eigenvectors with non-zero eigenvalues have the same form as Eqs. (A.23) and (A.24) except found from the lattice sites $2, \ldots, (N-1)$ only. The other two eigenvectors have a zero eigenvalue. Their degeneracy is not broken until the next order $(1/\gamma)$, and requires diagonalizing

$$\mathcal{G} = \mathbf{P}_0\mathbf{G}_0\mathbf{P}_0 - \frac{1}{\gamma}\mathbf{P}_0\mathbf{G}_0\tilde{\mathbf{P}}_0\frac{1}{\mathbf{G}_1}\tilde{\mathbf{P}}_0\mathbf{G}_0\mathbf{P}_0, \tag{A.32}$$

with $\tilde{\mathbf{P}}_0 = (\mathbf{I} - \mathbf{P}_0)$. This matrix has a simple form

$$\begin{aligned}\mathcal{G} &= -\sum_{n\neq 1,N}\frac{1}{m_n}|n\rangle\langle N+n| + \sum_{n\neq 1,N;m} K_{nm}|N+n\rangle\langle m| \\ &\quad +\frac{1}{\gamma}\sum_{n=1,N;m} K_{nm}|n\rangle\langle m|.\end{aligned} \tag{A.33}$$

Using this, we can search for the remaining two linearly independent and stable right eigenvectors with an eigenvalue of order $1/\gamma$. This results in a generalized eigenvalue problem for the zeroth order right eigenvectors, $\mathbf{K}|\lambda^0\rangle = \lambda\mathbf{B}|\lambda^0\rangle$ where $[\mathbf{B}]_{nm} = \delta_{nm}\,(\delta_{n1} + \delta_{nN})$. When this eigenvector is extended to the full degenerate space (padding it with zeros for all the momentum components), one has $\mathcal{G}|\lambda^0\rangle \approx \lambda/\gamma|\lambda^0\rangle$.

Starting with these zeroth order eigenvectors, then we can apply perturbation theory

as usual. This results in three sets of eigenvectors, ($\mathcal{B}_1$) ones with eigenvalues that are $\mathcal{O}(\gamma)$ ($|N+1\rangle$ and $|2N\rangle$), ($\mathcal{B}_0$) ones that are $\mathcal{O}(1)$ (Eqs. (A.23) and (A.24) but in the internal lattice), and ($\mathcal{B}_{-1}$) ones that are $\mathcal{O}(1/\gamma)$ ($\mathbf{K}|\lambda^0\rangle = \lambda\mathbf{B}|\lambda^0\rangle$). We can also delineate these sets by the subspace on which the zeroth order eigenvectors live ($\mathcal{B}_1$ on ($|N+1\rangle$ and $|2N\rangle$; $\mathcal{B}_0$ on $|n\rangle$ with $n = 2, \ldots, (N-1)$ and $|N+m\rangle$ with $m = 2, \ldots, (N-1)$; $\mathcal{B}_{-1}$ on $|n\rangle$ with $n = 1, \ldots, N$). Contributions to the eigenvectors outside this subspace will be order $1/\gamma$. As with the small γ regime, we need to group the different contributions into diagonal and off-diagonal (and then further distinguish between off-diagonal contributions between these three groups). We will break down the contributions to Eq. (A.15) in terms of each of the factors $\langle l_R|\mathbf{J}|k_R\rangle$, $\langle k_L|\mathbf{F}|l_L\rangle$, and $\lambda_k + \lambda_l^*$.

We start with the diagonal contributions. For eigenvectors in $\mathcal{B}_1$, we get contributions to $\langle l_R|\mathbf{J}|k_R\rangle$; $\langle k_L|\mathbf{F}|l_L\rangle$; $\lambda_k + \lambda_l^*$ of: at most $\mathcal{O}(1/\gamma)$ due to the zeroth order states living on $\{|N+1\rangle, |2N\rangle\}$; $\mathcal{O}(\gamma)$ as, e.g., $\langle N+1|\mathbf{F}|N+1\rangle = \mathcal{O}(\gamma)$; $\mathcal{O}(\gamma)$ because $\lambda_k \approx \gamma$. This gives an overall contribution at most of order $1/\gamma$.

For eigenvectors in $\mathcal{B}_0$, we get: $\mathcal{O}(1)$ (this is the same calculation as Eq. (A.30) as the states are eigenstates of $\mathbf{G}_0$ on the internal lattice); $\mathcal{O}(1/\gamma)$ because although $\mathbf{F}$ is order γ, the contribution of $|N+1\rangle$ and $|2N\rangle$ to the eigenvector are order $1/\gamma$; $\mathcal{O}(1/\gamma)$ because the eigenvalue has a real part that is order $1/\gamma$ (the imaginary part is order 1 but this cancels in $\lambda_k + \lambda_l^*$). Thus, the total contribution from a eigenvector in $\mathcal{B}_0$ is order 1. However, just like in Eq. (A.30) for the small γ regime, this contribution always has a paired contribution from the negative (positive) frequency mode, which cancels this order 1 contribution. This gives an overall contribution at most of order $1/\gamma$.

For eigenvectors in $\mathcal{B}_{-1}$, we get: $\mathcal{O}(1/\gamma)$ due to the zeroth order eigenvector living only on the position component of the vector; $\mathcal{O}(1/\gamma)$ because although $\mathbf{F}$ is order γ, the contribution of $|N+1\rangle$ and $|2N\rangle$ to the eigenvector are order $1/\gamma$; $\mathcal{O}(1/\gamma)$ because the eigenvalue has a real part of order $1/\gamma$. This gives an overall contribution at most of order $1/\gamma$.

For the off-diagonal terms, we give the contributions to each of the three factors for all the different possibilities in Table 0.1. The highest order contributions from the

off diagonal are order $1/\gamma$. Thus, the sum over all contributions gives zero for the zeroth order term and the leading term is order $1/\gamma$.

We note that for both the small γ and large γ regimes, these well-defined perturbation expansions demonstrate that the the zeroth order terms are zero, a fact which is obvious for the small γ regime (i.e., there would be no driving force for the thermal current) but not the large γ regime. Moreover, due to the presence of the different temperature reservoirs at each end, the first order expressions are non-zero always unless the lattice has a broken link. Coupled with the results of the anharmonic lattice, the perturbative expressions give evidence that the presence of these regimes are universal except in pathological cases.

B Ion Transport

Consider a pore in membrane of thickness L. We can use the Nernst-Plank equation to get the ionic current due to electric field, $\nabla\phi$, and concentration gradient, ∇n_i for ion species i with mobility μ_i and charge q_i.

$$\mathbf{J_i} = \mu_i k_B T \nabla n_i + n_i q_i \mu_i \nabla\phi, \tag{B.1}$$

where k_B is the Boltzmann constant. Now, assuming no variation in radial direction we can reduce this equation to one dimensional form

$$J_i = \mu_i k_B T \frac{dn_i}{dz} + n_i q_i \mu_i \frac{d\phi}{dz} \tag{B.2}$$

Multiplying by $e^{q_i\phi(z)/k_BT}$ we get

$$J_i e^{q_i\phi(z)/k_BT} = -\mu_i k_B T \frac{d}{dz}[n_i e^{q_i\phi(z)/k_BT}] \tag{B.3}$$

And, Integrating from $z = -L/2$ to $z = L/2$ we get

$$J_i = \mu_i k_B T \frac{n_i(-L/2)e^{q_i\phi(-L/2)/k_BT} - n_i(L/2)e^{q_i\phi(L/2)/k_BT}}{\int_{-L/2}^{L/2} e^{q_i\phi(Z)/k_BT} dZ}$$

We assume,

$$n_i(-L/2) = n_{\mathrm{i0}} e^{q_i\phi(z=-L/2,V=0)/k_BT} = n_{\mathrm{i0}}$$

$$n_i(L/2) = n_{\mathrm{i0}} e^{q_i\phi(z=L/2,V=0)/k_BT} = n_{\mathrm{i0}}$$

$$\phi(Z) = \begin{cases} VZ/L + \Delta F, & -\Delta L/2 \le z \le \Delta L \\ VZ/L, & \text{otherwise} \end{cases}$$

Thus the numerator becomes,

$$\begin{aligned} n_i(-L/2)e^{q_i\phi(L/2)/k_BT} - n_i(L/2)e^{q_i\phi(-L/2)/k_BT} &= n_{\mathrm{i0}}(e^{q_iV/2k_BT} - e^{-q_iV/2k_BT}) \\ &= 2n_{\mathrm{i0}}\sinh\left(\frac{q_iV}{2k_BT}\right) \end{aligned}$$

And the denominator can be simplified as,

$$\begin{aligned} &\int_{-L/2}^{L/2} e^{q_i\phi(Z)/k_BT}dZ \\ =&\int_{-L/2}^{-\Delta L/2} e^{q_i\phi(Z)/k_BT}dZ + \int_{-\Delta L/2}^{\Delta L/2} e^{q_i\phi(Z)/k_BT}dZ + \int_{\Delta L/2}^{L/2} e^{q_i\phi(Z)/k_BT}dZ \\ =&\int_{-L/2}^{-\Delta L/2} e^{q_iVZ/Lk_BT}dZ + \int_{-\Delta L/2}^{\Delta L/2} e^{\Delta F/k_BT}e^{q_iVZ/Lk_BT}dZ + \int_{\Delta L/2}^{L/2} e^{q_iVZ/Lk_BT}dZ \\ =&\frac{e^{-q_iV\Delta L/2Lk_BT} - e^{-q_iV/2k_BT}}{q_iV/Lk_BT} + e^{\Delta F/k_BT}\frac{e^{q_iV\Delta L/2Lk_BT} - e^{-q_iV\Delta L/2Lk_BT}}{q_iV/Lk_BT} \\ &+ \frac{e^{q_iV/2k_BT} - e^{q_iV\Delta L/2Lk_BT}}{q_iV/Lk_BT} \\ =&\frac{1}{q_iV/Lk_BT}\Big[e^{-q_iV\Delta L/2Lk_BT} - e^{q_iV\Delta L/2Lk_BT} + e^{q_iV/2k_BT} - e^{-q_iV/2k_BT} \\ &\qquad + \sinh\left(\frac{q_iV\Delta L}{2Lk_BT}\right)e^{\Delta F/k_BT}\Big] \\ =&\frac{2Lk_BT}{q_iV}\left[-\sinh(\frac{q_iV\Delta L}{2Lk_BT}) + \sinh\left(\frac{q_iV}{2k_BT}\right) + \sinh\left(\frac{q_iV\Delta L}{2Lk_BT}\right)e^{\Delta F/k_BT}\right] \end{aligned}$$

$$
\begin{aligned}
J_i =& \mu_i k_B T \frac{2 n_{\mathrm{i}0} \sinh\left(\frac{q_i V}{2k_B T}\right)}{2\frac{Lk_B T}{q_i V}\left[-\sinh\left(\frac{q_i V \Delta L}{2Lk_B T}\right)+\sinh\left(\frac{q_i V}{2k_B T}\right)+\sinh\left(\frac{q_i V \Delta L}{2Lk_B T}\right)e^{\Delta F/k_B T}\right]} \\
=& \mu_i n_{\mathrm{i}0}\frac{q_i V}{L}\frac{\sinh\left(\frac{q_i V}{2k_B T}\right)}{\left[\sinh\left(\frac{q_i V}{2k_B T}\right)-\sinh\left(\frac{q_i V \Delta L}{2Lk_B T}\right)+\sinh\left(\frac{q_i V \Delta L}{2Lk_B T}\right)e^{\Delta F/k_B T}\right]} \\
=& q_i n_{\mathrm{i}0}\frac{\mu_i V}{L}\left[1-\frac{\sinh\left(\frac{q_i V \Delta L}{2Lk_B T}\right)}{\sinh\left(\frac{q_i V}{2k_B T}\right)}(1-e^{\Delta F/k_B T})\right]^{-1}
\end{aligned}
$$

C Brunger, Brooks, Karplus (BBK) method

Langevin equation of motion of a particle under the influence of noise and friction is given as

$$F(\vec{x}_n) + \vec{f}_n(t) = m\ddot{x}_n, \tag{C.1}$$

where, $F(\vec{x}_n)$ is the sum of external forces and $f_n(t) = \eta_n(t) - \gamma_n \dot{x}_n(t)$ is the random force. The noise $\eta_n(t)$ and friction coefficient γ_n are related by the fluctuation-dissipation relation

$$\langle \eta_n(t)\eta_m(t')\rangle = 2\gamma_n k_B T_n \delta_{nm}\delta(t-t'). \tag{C.2}$$

Several numerical algorithms exits for the solution of Langevin Dynamics. One of the most commonly used algorithm is given by Brunger, Brooks and Karplus [188]
From the Eq. C.1, acceleration of a particle is given by

$$\ddot{x}_n(t) = \frac{1}{m}[F(\vec{x}_n) + \eta_n(t) - \gamma_n \dot{x}_n(t)] \tag{C.3}$$

Thus we get,

$$x_n(t+\Delta t) = x_n(t) + \dot{x}_n(t)\Delta t + \ddot{x}_n(t)\frac{\Delta t^2}{2} + \dddot{x}_n\frac{\Delta t^3}{6} + O(\Delta t^4) \tag{C.4}$$

$$x_n(t-\Delta t) = x_n(t) - \dot{x}_n(t)\Delta t + \ddot{x}_n(t)\frac{\Delta t^2}{2} - \dddot{x}_n\frac{\Delta t^3}{6} + O(\Delta t^4) \tag{C.5}$$

Adding

$$x(t+\Delta t) + x_n(t-\Delta t) = 2x_n(t) + \ddot{x}_n(t)\Delta t^2 + O(\Delta t^4) \tag{C.6}$$

Which gives:

$$x(t+\Delta t) = 2x_n(t) - x_n(t-\Delta t) + \frac{\Delta t^2}{m}[F(\vec{x}_n) + \eta_n(t) - \gamma_n\dot{x}_n(t)] + O(\Delta t^4) \tag{C.7}$$

This propagation equation needs the particle velocity $\dot{x}_n(t)$ which can be obtained as

$$\dot{x}_n(t) \approx \frac{x_n(t+\Delta t) - x_n(t-\Delta t)}{2\Delta t}$$

Using in Eq. (10) we get,

$$\begin{aligned} x(t+\Delta t) = {} & 2x_n(t) - x_n(t-\Delta t) \\ & + \frac{\Delta t^2}{m}[F(\vec{x}_n) + \eta_n(t)] \\ & - \frac{\Delta t}{2m}\gamma_n[x_n(t+\Delta t) - x_n(t-\Delta t)] + O(\Delta t^4) \end{aligned}$$

Rearranging, we get,

$$x(t+\Delta t) = \frac{2x_n(t) - x_n(t-\Delta t) + \gamma\frac{\Delta t}{2m}x_n(t-\Delta t) + \frac{\Delta t^2}{m}\left[F(\vec{x}_n) + \eta_n(t)\right]}{1 + \gamma\frac{\Delta t}{2m}} \tag{C.8}$$